Title
Dopamine D3 receptor modulation of prefrontal cells and circuits

Author
Clarkson, Rebecca Lauren

Publication Date
2017

Peer reviewed|Thesis/dissertation

Dopamine D3 receptor modulation of prefrontal cells and circuits

by

Rebecca Lauren Clarkson

DISSERTATION

Submitted in partial satisfaction of the requirements for the degree of

DOCTOR OF PHILOSOPHY

in

Neuroscience

in the

GRADUATE DIVISION

of the

UNIVERSITY OF CALIFORNIA, SAN FRANCISCO

Acknowledgements

First and foremost, I would like to thank Kevin Bender and the entire Bender lab, past and present. With Kevin's guidance and support, this lab has grown tremendously in the five years that I have been a member; from the valiant few in Emeryville at the Gallo Center, to the vibrant, supportive, and exceedingly talkative cohort at Mission Bay. I strongly admire Kevin's unwavering intellectual curiosity that underlies his passion for scientific research, in addition to his commitment to teaching. The warm and collegial environment within the lab is a testament to his compassion, patience, and enthusiasm as a mentor. In addition, I owe many thanks to all members of the Bender lab with whom I have worked and collaborated. I have had the pleasure to know these individuals both as colleagues and as friends. In particular, I would like to thank Ken Burke, Alayna Liptak, and Gina Rinetti, all of whom provided critical support and camaraderie during my early years in lab.

I would also like to thank the UCSF faculty members who taught and mentored me throughout my years here. My thesis committee members, Roger Nicoll, Anatol Kreitzer, and Vikaas Sohal, have been outstanding in providing scientific guidance and insight throughout this process. I would also like to thank Dr. Stephan Lammel for graciously serving as the external member of my thesis committee. Furthermore, thanks to Patricia Veitch and Lucita Nacionales, program administrators who work hard to make the UCSF Neuroscience Graduate Program run smoothly.

In addition, I am incredibly grateful to my entire graduate cohort. We began this program together 6 years ago, and I have been privileged to be part of such a warm, supportive, and inclusive group of people who truly enjoy each other's company.

Special thanks to Joe Boivin, for years of East Bay hiking adventures, to Joanne Cheung, for lovely conversations with wine, and to Sarah Robinson for coffee excursions and always stopping by lab to say “Hello.”

I have also found many supportive networks outside the laboratory. In particular, I am incredibly grateful for the vibrant group exercise community here at UCSF. In addition, thanks to Catherine Paltin Hicks and Mark Llorente for many delightful Wednesday nights, thanks to Ian and Sarah Oldenburg for joining me on the West coast, and thanks to Remi Frazier for the many therapeutic playdates with his baby, Miles. And of course, thanks to Ana Nelson for helping me cross the finish line.

Finally, I would like to thank the support of my family, both during my graduate studies and all the years before. To my parents, Ken Clarkson and Ronnie Cooperstein, for their support of all my intellectual and educational endeavors, and to Grandma and Papa for bringing our family to Woods Hole, MA, where I developed my love of science. Throughout my life, my scientific curiosity has been supported by teachers and community members, from my childhood attending the Children’s School of Science in Woods Hole, to the UCSF Neuroscience graduate program, and I would like to thank everyone who has been a part of that process.

Author Contributions

The text of Chapter 2 of this thesis is a reprint of the material as it originally appeared in The Journal of Neuroscience (Clarkson et al., 2017). Rebecca Clarkson and Kevin Bender contributed equally to the electrophysiology experiments in this chapter. Rebecca Clarkson performed the supervised machine learning analysis and retrograde tracing experiments. Kevin Bender performed the calcium imaging experiments. Alayna Liptak and Steven Gee, third and fourth authors on this paper, performed viral injections for the orthograde tracing experiments. Alayna Liptak also contributed morphological reconstructions and widefield imaging. Kevin Bender and Vikaas Sohal directed and supervised the research. Rebecca Clarkson and Kevin Bender co-wrote the paper.

The experiments discussed in Chapters 3 and 4 were performed as described for Chapter 2. Rebecca Clarkson wrote these chapters and performed all additional image and electrophysiological analyses. Kevin Bender and Vikaas Sohal directed and supervised the research.

Abstract

Prefrontal circuits process input from the internal and external world and use these inputs to guide decision-making and subsequent goal-directed behavior. The ability of the prefrontal cortex (PFC) to flexibly guide appropriate behaviors, including updating expectations of reward and punishment, is highly sensitive to neuromodulators such as dopamine. Therefore, elucidating the cellular expression of dopamine receptors on prefrontal projection neurons is critical for understanding how dopamine can act on the prefrontal network, and thereby regulate cognitive and behavioral processes. Dopamine acts in part to regulate the activity of prefrontal layer 5 (L5) principal cells via D1-family (D1/D5) or D2-family (D2/D3/D4) receptors. Recent work indicates that D1- and D2-receptors (D1R/D2R) are expressed in largely separate subclasses of L5 pyramidal cell and that these subclasses have unique electrophysiological features and projection patterns, and are modulated by dopamine via distinct mechanisms. How other dopamine receptor classes are distributed in mPFC is unknown.

D3R signaling is critically important for prefrontal executive function, as manipulations perturbing prefrontal D3Rs affect high level cognitive processes such as anxiety and reversal learning. However, the mechanisms by which D3Rs regulate prefrontal cells and circuits remains unknown. By applying a supervised machine learning approach to electrophysiological recordings from dopamine receptor reporter lines, I determine that D3R-expressing (D3+) pyramidal neurons are electrophysiologically distinct from D1R- and D2R-expressing neurons, and therefore likely represent a separate cell subclass. With anatomical tracing techniques, I demonstrate that L5 D3+ neurons are an intratelencephalic cell type. Further

experiments reveal that D3R activation within this cell class can regulate calcium channels in the axon initial segment, thereby suppressing action potential burst generation. This provides a mechanism by which modulation via D2-family receptors could directly affect PFC output to other cortical areas.

Table of Contents

List of Figures

List of Tables

Chapter 1

General Introduction

Appropriate decision-making and subsequent goal-directed behavior requires the integration of previously-learned action-outcome relationships with processing of internal and external states. The prefrontal cortex (PFC) facilitates numerous high-order executive functions required for this flexible responding to novel circumstances, including attention, working memory, response inhibition, and temporal sequencing of behavior (Dalley et al., 2004). Normal function of prefrontal circuits relies strongly on neuromodulatory regulation, with a critical contribution from dopaminergic mesocortical input. Indeed, perturbations in prefrontal dopamine are implicated in neuropsychiatric disorders such as schizophrenia, addiction, and depression (Kalivas et al., 2005; Durstewitz and Seamans, 2008; Leggio et al., 2013), as well as in stress-induced cognitive impairments (Butts et al., 2011).

To understand the function of prefrontal dopamine in both health and disease, it is critical to understand its cellular substrates. mRNA encoding all five dopamine receptor subtypes is found in non-human primate PFC, with the majority in cortical layer 5 (L5) (Lidow et al., 1998), which receives dense dopaminergic innervation (Descarries et al., 1987; Miner et al., 2003). This establishes a framework through which dopamine is poised to regulate PFC output to downstream structures, by acting directly on L5 PFC output neurons that project to numerous cortical and subcortical regions (Gabbott et al., 2005). In this dissertation, I focus on the role of dopamine D3 receptors (D3Rs) in prefrontal cells and circuits, with an emphasis on understanding their role in regulating

L5 pyramidal neuron output; I find that D3Rs modulate neuronal excitability in a novel population of callosally-projecting PFC pyramidal neurons.

PFC control of high-level cognitive and emotional function

As a critical node in a distributed neural network, the PFC provides top-down flexible control of complex cognitive and behavioral processes (Dalley et al., 2004). To perform these functions, the PFC receives input from and sends output to diverse cortical and subcortical regions, with extensive reciprocal connectivity (Carr and Sesack, 2000; Vertes, 2004; Gabbott et al., 2005; Hoover and Vertes, 2007). Though the entire PFC is involved in high-level executive function, it contains multiple subregions, each playing distinct roles in prefrontal-dependent cognitive processing. My dissertation focuses on the rodent medial PFC (mPFC), a prefrontal subregion critical for both processing of and responding to emotionally salient stimuli.

The mPFC conveys highly-processed information to diverse long-range targets, including other cortical regions, numerous limbic structures (such as the basolateral amygdala [BLA] and nucleus accumbens [nAC]), and midline thalamus (Vertes, 2004). The mPFC also projects to virtually all neuromodulatory centers, including the ventral tegmental area (VTA), basal forebrain, locus coeruleus, and raphe nuclei (Dembrow and Johnston, 2014). Prefrontal output to these downstream structures can actively drive behavioral changes, as shown via optogenetic manipulations of specific mPFC projections. For example, mPFC terminal photostimulation in the dorsal raphe nucleus increases avoidance during social interaction (Challis et al., 2014), whereas terminal photostimulation in the BLA is anxiolytic, increasing time spent in the open arms of an

elevated plus maze (Vialou et al., 2014). While glutamatergic prefrontal outputs contribute to driving goal-directed behavior, ascending neuromodulatory systems provide critical signals of internal state, including mood, attention, motivation, and expectations of reward or punishment (Clark and Noudoost, 2014). Indeed, the mPFC is reciprocally connected with all the neuromodulatory centers mentioned above, thereby receiving dopaminergic, cholinergic, noradrenergic, and serotonergic modulatory input (Dembrow and Johnston, 2014).

Prefrontal dopamine in health and disease

The mPFC receives its dopaminergic inputs from dopamine neurons within the VTA (Björklund and Dunnett, 2007). Classic work postulates that VTA dopamine neurons encode reward prediction error (RPE), signaling discrepancies between expectations and outcome, thereby driving learning. In support of this model, unexpected reward (or reward-related sensory cues) increases phasic burst firing in midbrain dopamine neurons, while the absence of expected reward (or cues thereof) suppresses tonic dopamine neuron activity (Schultz et al., 1997). Recent studies have probed the causal relationship between reward-related electrophysiological responses and reinforcement learning. As predicted, temporally-specific phasic stimulation or transient suppression of VTA dopamine neurons mimic positive or negative RPE (Steinberg et al., 2013; Chang et al., 2015).

However, the different roles of VTA's dopaminergic projections to numerous corticolimbic targets (e.g. mPFC, dorsal and ventral striatum, amygdala) are still being clarified. The VTA contains anatomically and functionally distinct dopamine neuron

populations, with distinct axonal projections and input sources (Lammel et al., 2014). Furthermore, in addition to encoding RPE, dopamine neurons can also signal nonrewarding events, including those that are salient, uncertain, novel, or even aversive (Bromberg-Martin et al., 2010). Interestingly, Lammel et al. recently demonstrated a role for the mPFC in processing aversive inputs. In one study, an aversive stimulus (hind paw formalin), but not a rewarding one (cocaine administration), modified synapses on mPFC-projecting VTA dopamine neurons (Lammel et al., 2011). In addition, VTA inputs from the lateral habenula (LHb) synapsed onto mPFC-projecting VTA neurons. They further show that mPFC dopamine is required for the conditioned place avoidance elicited by stimulation of LHb terminals in the VTA (Lammel et al., 2012). However, VTA terminal stimulation in the mPFC is neither positively nor negatively reinforcing, but instead can alter whether an animal is in a more flexible or perseverative behavioral mode (Ellwood et al., 2017).

Prefrontal dopamine plays a critical role in regulating high-level cognitive processes (Seamans and Yang, 2004). In a pioneering early study, selective depletion of prefrontal dopamine in non-human primates was shown to impair working memory performance (Brozoski et al., 1979). Dysfunctional dopamine signaling in the mPFC is implicated in numerous neuropsychiatric disorders, including schizophrenia, depression, and addiction, that involve maladaptive emotional learning and inappropriate processing of motivationally significant information (Yang et al., 1999; Laviolette and Grace, 2006; Leggio et al., 2013).

Differing roles of prefrontal D1-family and D2-family receptors

At a cellular level, dopamine regulates mPFC-mediated cognitive function through D1- and D2-family receptors (D1/D5 and D2/D3/D4, respectively). These receptor families are thought to have opposing effects on PFC-dependent cognitive function, as proposed by the "Dual-State Theory" of prefrontal function (Durstewitz and Seamans, 2008). In this model, D1-family receptors stabilize active neural representations, facilitating robust working memory despite environmental distractions, thereby supporting maintenance of previously learned behavioral strategies. In contrast, D2-family activation destabilizes the prefrontal network, promoting flexible behavioral responding (Durstewitz and Seamans, 2008). A balance between these "exploit" and "explore" behavioral modes is important for successful behavioral adaptation in the face of uncertainty (Daw et al., 2006), determining when to implement known strategies and when to search for new ones.

Extensive work supports a critical role for D1-family receptors in both the behavioral and neural correlates of working memory. For example, in nonhuman primates, prefrontal infusion of D1-family (but not D2-family) receptor antagonists disrupted performance in an oculomotor delayed response task; monkeys became less accurate in making memory-guided saccades, after a delay following a location cue (Sawaguchi and Goldman-Rakic, 1991, 1994). In addition, D1-, but not D2-family receptors modulated delay-period persistent neuronal activity, a presumed neural basis for working memory (Williams and Goldman-Rakic, 1995; Wang et al., 2004; Arnsten et al., 2012).

While D2-family receptors are not strongly implicated in PFC-dependent working memory processes, they are proposed to support behavioral flexibility (Durstewitz and Seamans, 2008; Floresco, 2013; Puig and Miller, 2015). For example, blockade of mPFC D2-family receptors impaired rodents' performance in a maze-based set-shifting paradigm. This task required a shift between a response-based strategy (i.e. "always turn left") and a visual-cue discrimination strategy (i.e. "turn toward the stripes"). D2-family receptor antagonism increased perseverative responding, in which the no-longer valid strategy continued to be used (Floresco et al., 2006). In another study, monkeys learned novel associations between visual cues and saccades to the left or right; both D1- and D2-family receptor antagonism in the PFC impaired learning of novel associations but D2-family receptor antagonism resulted in the largest increase in perseverative errors (consecutive repetition of the same error) (Puig and Miller, 2015).

The mRNA for all five dopamine receptor subtypes are expressed in the PFC (Lidow et al., 1998). Unfortunately, historically, pharmacological manipulations only readily distinguished between dopamine receptor families, not individual subtypes. Therefore, many studies of dopamine receptors' roles in PFC function have been restricted to a dissociation between D1-family and D2-family receptors. However, to fully understand dopamine's role in PFC function, it will be critical to determine the cellular substrates of all five prefrontal dopamine receptor subtypes as well as resultant effects on neuronal computation and behavior. In this dissertation, I focus on the D3R, a member of the D2-family of dopamine receptors, leveraging the ability to identify and manipulate D3R-expressing neurons with a D3-Cre transgenic mouse line.

D3R signaling and distribution

As a member of the D2-receptor family, the D3R is a G-protein-coupled receptor that signals via canonical G protein, $G\alpha_{i/o}$-dependent mechanisms, as well as through non-canonical β-arrestin-dependent mechanisms (Beaulieu et al., 2009; Beaulieu and Gainetdinov, 2011; Yang et al., 2016). In contrast to the D1R and D2R, which are distributed widely throughout the brain, the D3R has a more restricted anatomical distribution (Missale et al., 1998; Nakajima et al., 2013), with mRNA expression highest in limbic structures, such as the nucleus accumbens, Islands of Calleja, and hippocampal formation. D3R mRNA is also found throughout neocortical regions, including the PFC, though at lower levels (Bouthenet et al., 1991; Suzuki et al., 1998).

Despite their relatively low abundance in the PFC, dysfunction in prefrontal D3R signaling is thought to be a major contributor to neuropsychiatric disorders, including schizophrenia and drug addiction (Schwartz et al., 2000; Newman et al., 2012); indeed, while the role of D2R dysfunction in schizophrenia has historically been the focus, currently prescribed antipsychotics have equal affinity for D3R and D2R (Joyce and Millan, 2005; Gross et al., 2013). In addition, convergent evidence from D3R knockout mice and prefrontal micro-infusions of preferential D3R antagonists suggests a pro-cognitive effect of decreased prefrontal D3R activation (Glickstein et al., 2005; Loiseau and Millan, 2009; Watson et al., 2012). However, the cellular mechanisms by which D3Rs modulate prefrontal function remain unclear. In this dissertation, I focus on dopaminergic modulation of D3R-expressing (D3+) mPFC projection neurons, establishing a framework for understanding the impact of D3R-dependent dopaminergic regulation on prefrontal control of downstream brain structures.

Cortical pyramidal neuron heterogeneity

The downstream impact of D3R-dependent regulation of prefrontal output neurons will depend upon the postsynaptic targets of these neurons. With respect to downstream targets, cortical pyramidal neurons comprise two major types: intratelencephalic (IT) and pyramidal tract (PT). IT neurons project only within the telencephalon, including the neocortex, striatum, and amygdala. In contrast, PT neurons project subcortically, such as to the thalamus, brainstem, and spinal cord (Harris and Shepherd, 2015).

Previous studies have examined the electrophysiological and morphological properties of L5 pyramidal neurons from the somatosensory, visual, and frontal cortices based on their axonal projections. Convergent results across the neocortex indicate that IT and PT pyramidal neurons are both electrophysiologically and morphologically distinct. Specifically, L5 pyramidal neurons projecting to the striatum or contralateral cortex show spike frequency adaptation and minimal voltage sag ("h-current") in response to hyperpolarizing current injection. In addition, they have "thin-tufted" dendritic morphology, with narrow dendritic arborization. In contrast, L5 pyramidal neurons projecting to the thalamus, pons, or spinal cord have an initial action potential doublet in response to depolarizing current, followed by regular firing. In addition, these PT neurons have high h-current and are "thick-tufted" (Kasper et al., 1994; Morishima and Kawaguchi, 2006; Hattox and Nelson, 2007; Dembrow et al., 2010; Gee et al., 2012).

Recent work reveals that D1R- and D2R-expressing L5 mPFC pyramidal neurons are IT and PT, respectively, with corresponding electrophysiological and morphological properties (Gee et al., 2012; Seong and Carter, 2012). However, the projection targets of D3R-expressing mPFC pyramidal neurons remain unexamined. Are D3+ neurons an IT or PT subtype, and, if so, are they a distinct population from the previously described D1+ and D2+ neurons? How does prefrontal dopaminergic modulation affect D3+ neuron output to downstream brain structures? These questions will be addressed in depth.

*****

Chapter 2 examines the role of prefrontal D3Rs in regulating neuronal function, revealing a novel population of callosally-projecting pyramidal neurons that express the D3R and largely lack D1R and D2R expression. By implementing a supervised machine learning approach, we find that D3+ neurons are electrophysiologically separable from D1+ and D2+ neurons. Furthermore, we find that dopamine regulates neuronal excitability selectively in this cell population via D3R-dependent action, decreasing the propensity for high frequency action potential bursts.

Chapter 3 extends the characterization of the transgenic mouse lines used in Chapter 2, with a focus on the D3-Cre line. I find that mPFC D3+ neurons project to the majority of known mPFC targets, but that they have a relatively low cell density and comprise a fairly small percentage of total mPFC output. In addition, I examine the distribution of D3Rs within this mouse line, finding strong agreement with prior studies of D3R mRNA expression in the rodent brain.

In Chapter 4, I expand on the supervised machine learning approach used in Chapter 2 for the electrophysiological classification of D1+ and D3+ neurons, clarifying both the exploratory data analysis techniques as well as the important experimental concerns that will help other researchers apply this approach to electrophysiological classification in other cell types and brain regions.

Finally, in Chapter 5, I synthesize and discuss the collective findings of this dissertation, providing concluding remarks concerning core findings and possible future directions for this research.

References

Arnsten AFT, Wang MJ, Paspalas CD (2012) Neuromodulation of Thought: Flexibilities and Vulnerabilities in Prefrontal Cortical Network Synapses. Neuron 76:223–239.

Beaulieu J-M, Gainetdinov RR (2011) The physiology, signaling, and pharmacology of dopamine receptors. Pharmacol Rev 63:182–217.

Beaulieu J-M, Gainetdinov RR, Caron MG (2009) Akt/GSK3 signaling in the action of psychotropic drugs. Annu Rev Pharmacol Toxicol 49:327–347.

Björklund A, Dunnett SB (2007) Dopamine neuron systems in the brain: an update. Trends Neurosci 30:194–202.

Bouthenet M-L, Souil E, Martres M-P, Sokoloff P, Giros B, Schwartz J-C (1991) Localization of dopamine D3 receptor mRNA in the rat brain using in situ hybridization histochemistry: comparison with dopamine D2 receptor mRNA. Brain Res 564:203–219.

Bromberg-Martin ES, Matsumoto M, Hikosaka O (2010) Dopamine in Motivational Control: Rewarding, Aversive, and Alerting. Neuron 68:815–834.

Brozoski TJ, Brown RM, Rosvold HE, Goldman PS (1979) Cognitive deficit caused by regional depletion of dopamine in prefrontal cortex of rhesus monkey. Science 205:929–932.

Butts KA, Weinberg J, Young AH, Phillips AG (2011) Glucocorticoid receptors in the prefrontal cortex regulate stress-evoked dopamine efflux and aspects of executive function. Proc Natl Acad Sci U S A 108:18459–18464.

Carr DB, Sesack SR (2000) Projections from the rat prefrontal cortex to the ventral tegmental area: target specificity in the synaptic associations with mesoaccumbens and mesocortical neurons. J Neurosci 20:3864–3873.

Challis C, Beck SG, Berton O (2014) Optogenetic modulation of descending prefrontocortical inputs to the dorsal raphe bidirectionally bias socioaffective choices after social defeat. Front Behav Neurosci 8:43.

Chang CY, Esber GR, Marrero-Garcia Y, Yau H-J, Bonci A, Schoenbaum G (2015) Brief optogenetic inhibition of dopamine neurons mimics endogenous negative reward prediction errors. Nat Neurosci 19:1–8.

Clark KL, Noudoost B (2014) The role of prefrontal catecholamines in attention and working memory. Front Neural Circuits 8:33.

Dalley JW, Cardinal RN, Robbins TW (2004) Prefrontal executive and cognitive functions in rodents: Neural and neurochemical substrates. Neurosci Biobehav Rev 28:771–784.

Daw ND, O'Doherty JP, Dayan P, Dolan RJ, Seymour B (2006) Cortical substrates for exploratory decisions in humans. Nature 441:876–879.

Dembrow N, Johnston D (2014) Subcircuit-specific neuromodulation in the prefrontal cortex. Front Neural Circuits 8:1–9.

Dembrow NC, Chitwood RA, Johnston D (2010) Projection-specific neuromodulation of medial prefrontal cortex neurons. J Neurosci 30:16922–16937.

Descarries L, Lemay B, Doucet G, Berger B (1987) Regional and laminar density of the dopamine innervation in adult rat cerebral cortex. Neuroscience 21:807–824.

Durstewitz D, Seamans JK (2008) The Dual-State Theory of Prefrontal Cortex Dopamine Function with Relevance to Catechol-O-Methyltransferase Genotypes and Schizophrenia. Biol Psychiatry 64:739–749.

Ellwood IT, Patel T, Wadia V, Lee AT, Liptak AT, Bender KJ, Sohal VS (2017) Tonic or phasic stimulation of dopaminergic projections to prefrontal cortex causes mice to maintain or deviate from previously learned behavioral strategies. J Neurosci:1221–17.

Floresco SB (2013) Prefrontal dopamine and behavioral flexibility: shifting from an "inverted-U" toward a family of functions. Front Neurosci 7.

Floresco SB, Magyar O, Ghods-Sharifi S, Vexelman C, Tse MTL (2006) Multiple Dopamine Receptor Subtypes in the Medial Prefrontal Cortex of the Rat Regulate Set-Shifting. Neuropsychopharmacology 31:297–309.

Gabbott PL a, Warner T a., Jays PRL, Salway P, Busby SJ (2005) Prefrontal cortex in the rat: Projections to subcortical autonomic, motor, and limbic centers. J Comp Neurol 492:145–177.

Gee S, Ellwood I, Patel T, Luongo F, Deisseroth K, Sohal VS (2012) Synaptic activity unmasks dopamine D2 receptor modulation of a specific class of layer V pyramidal neurons in prefrontal cortex. J Neurosci 32:4959–4971.

Glickstein SB, Desteno DA, Hof PR, Schmauss C (2005) Mice lacking dopamine D2 and D3 receptors exhibit differential activation of prefrontal cortical neurons during tasks requiring attention. Cereb Cortex 15:1016–1024.

Gross G, Wicke K, Drescher KU (2013) Dopamine D_3 receptor antagonism--still a therapeutic option for the treatment of schizophrenia. Naunyn Schmiedebergs Arch Pharmacol 386:155–166.

Harris KD, Shepherd GMG (2015) The neocortical circuit: themes and variations. Nat Neurosci 18:170–181.

Hattox AM, Nelson SB (2007) Layer V neurons in mouse cortex projecting to different targets have distinct physiological properties. J Neurophysiol 98:3330–3340.

Hoover WB, Vertes RP (2007) Anatomical analysis of afferent projections to the medial prefrontal cortex in the rat. Brain Struct Funct 212:149–179.

Joyce JN, Millan MJ (2005) Dopamine D3 receptor antagonists as therapeutic agents. Drug Discov Today 10:917–925.

Kalivas PW, Volkow N, Seamans J (2005) Unmanageable motivation in addiction: A pathology in prefrontal-accumbens glutamate transmission. Neuron 45:647–650.

Kasper EM, Larkman AU, Lübke J, Blakemore C (1994) Pyramidal neurons in layer 5 of the rat visual cortex. I. Correlation among cell morphology, intrinsic electrophysiological properties, and axon targets. J Comp Neurol 339:459–474.

Lammel S, Ion DI, Roeper J, Malenka RC (2011) Projection-Specific Modulation of Dopamine Neuron Synapses by Aversive and Rewarding Stimuli. Neuron 70:855–862.

Lammel S, Lim BK, Malenka RC (2014) Reward and aversion in a heterogeneous midbrain dopamine system. Neuropharmacology 76:351–359.

Lammel S, Lim BK, Ran C, Huang KW, Betley MJ, Tye KM, Deisseroth K, Malenka RC (2012) Input-specific control of reward and aversion in the ventral tegmental area. Nature 491:212–217.

Laviolette SR, Grace AA (2006) The roles of cannabinoid and dopamine receptor systems in neural emotional learning circuits: implications for schizophrenia and addiction. Cell Mol Life Sci 63:1597–1613.

Leggio GM, Salomone S, Bucolo C, Platania C, Micale V, Caraci F, Drago F (2013) Dopamine D3 receptor as a new pharmacological target for the treatment of depression. Eur J Pharmacol 719:25–33.

Lidow MS, Wang F, Cao Y, Goldman-Rakic PS (1998) Layer V neurons bear the majority of mRNAs encoding the five distinct dopamine receptor subtypes in the primate prefrontal cortex. Synapse 28:10–20.

Loiseau F, Millan MJ (2009) Blockade of dopamine D3 receptors in frontal cortex, but not in sub-cortical structures, enhances social recognition in rats: Similar actions of D1 receptor agonists, but not of D2 antagonists. Eur Neuropsychopharmacol 19:23–33.

Miner LH, Schroeter S, Blakely RD, Sesack SR (2003) Ultrastructural Localization of the Norepinephrine Transporter in Superficial and Deep Layers of the Rat Prelimbic Prefrontal Cortex and Its Spatial Relationship to Probable Dopamine Terminals. J Comp Neurol 466:478–494.

Missale C, Nash RS, Robinson SW, Jaber M, Caron MG (1998) Dopamine Receptors: From Structure to Function. Physiol Rev 78:189–225.

Morishima M, Kawaguchi Y (2006) Recurrent connection patterns of corticostriatal pyramidal cells in frontal cortex. J Neurosci 26:4394–4405.

Nakajima S, Gerretsen P, Takeuchi H, Caravaggio F, Chow T, Le Foll B, Mulsant B, Pollock B, Graff-Guerrero A (2013) The potential role of dopamine D3 receptor neurotransmission in cognition. Eur Neuropsychopharmacol 23:799–813.

Newman AH, Blaylock BL, Nader MA, Bergman J, Sibley DR, Skolnick P (2012) Medication discovery for addiction: translating the dopamine D3 receptor hypothesis. Biochem Pharmacol 84:882–890.

Puig MV, Miller EK (2015) Neural substrates of dopamine d2 receptor modulated executive functions in the monkey prefrontal Cortex. Cereb Cortex 25:2980–2987.

Sawaguchi T, Goldman-Rakic PS (1991) D1 dopamine receptors in prefrontal cortex: involvement in working memory. Science 251:947–950.

Sawaguchi T, Goldman-Rakic PS (1994) The role of D1-dopamine receptor in working memory: local injections of dopamine antagonists into the prefrontal cortex of rhesus monkeys performing an oculomotor delayed-response task. J Neurophysiol 71:515–528.

Schultz W, Dayan P, Montague PR (1997) A neural substrate of prediction and reward. Science 275:1593–1599.

Schwartz JC, Diaz J, Pilon C, Sokoloff P (2000) Possible implications of the dopamine D3 receptor in schizophrenia and in antipsychotic drug actions. Brain Res Rev 31:277–287.

Seamans JK, Yang CR (2004) The principal features and mechanisms of dopamine modulation in the prefrontal cortex. Prog Neurobiol 74:1–57.

Seong HJ, Carter AG (2012) D1 receptor modulation of action potential firing in a subpopulation of layer 5 pyramidal neurons in the prefrontal cortex. J Neurosci 32:10516–10521.

Steinberg EE, Keiflin R, Boivin JR, Witten IB, Deisseroth K, Janak PH (2013) A causal link between prediction errors, dopamine neurons and learning. Nat Neurosci 16:966–973.

Suzuki M, Hurd YL, Sokoloff P, Schwartz J-C, Sedvall G (1998) D3 dopamine receptor mRNA is widely expressed in the human brain. Brain Res 779:58–74.

Vertes RP (2004) Differential projections of the infralimbic and prelimbic cortex in the rat. Synapse 51:32–58.

Vialou V, Bagot RC, Cahill ME, Ferguson D, Robison AJ, Dietz DM, Fallon B, Mazei-Robison M, Ku SM, Harrigan E, Winstanley CA, Joshi T, Feng J, Berton O, Nestler EJ

(2014) Prefrontal cortical circuit for depression- and anxiety-related behaviors mediated by cholecystokinin: Role of FosB. J Neurosci 34:3878–3887.

Wang M, Vijarayaghavan S, Goldman-Rakic PS (2004) Selective D2 Receptor Actions on Working Memory. Science 303:853–856.

Watson DJG, Loiseau F, Ingallinesi M, Millan MJ, Marsden C a, Fone KCF (2012) Selective blockade of dopamine D3 receptors enhances while D2 receptor antagonism impairs social novelty discrimination and novel object recognition in rats: a key role for the prefrontal cortex. Neuropsychopharmacology 37:770–786.

Williams G V, Goldman-Rakic PS (1995) Modulation of memory fields by dopamine D1 receptors in prefrontal cortex. Nature 376:572–575.

Yang CR, Seamans JK, Gorelova N (1999) Developing a neuronal model for the pathophysiology of schizophrenia based on the nature of electrophysiological actions of dopamine in the prefrontal cortex. Neuropsychopharmacology 21:161–194.

Yang S, Ben-Shalom R, Ahn M, Liptak AT, van Rijn RM, Whistler JL, Bender KJ (2016) β-Arrestin-Dependent Dopaminergic Regulation of Calcium Channel Activity in the Axon Initial Segment. Cell Rep 16:1518–1526.

Chapter 2

D3 receptors regulate excitability in a unique class of prefrontal pyramidal cells

Abstract

The D3 dopamine receptor, a member of the G_i-coupled D2 family of dopamine receptors, is expressed throughout limbic circuits affected in neuropsychiatric disorders, including prefrontal cortex (PFC). These receptors are important for prefrontal executive function because pharmacological and genetic manipulations that affect prefrontal D3 receptors alter anxiety, social interaction, and reversal learning. However, the mechanisms by which D3 receptors regulate prefrontal circuits and whether D3 receptors regulate specific prefrontal subnetworks remains unknown. Here, we combine dopamine receptor reporter lines, anatomical tracing techniques, and electrophysiology to show that D3 receptor expression defines a novel subclass of layer 5 glutamatergic pyramidal cell in mouse PFC (either sex). D3-receptor-expressing pyramidal neurons are electrophysiologically and anatomically separable from neighboring neurons expressing D1 or D2 receptors based on their dendritic morphology and subthreshold and suprathreshold intrinsic excitability. D3-receptor-expressing neurons send axonal projections to intratelencephalic (IT) targets, including contralateral cortex, nucleus accumbens, and basolateral amygdala. Within these neurons, D3 receptor activation was found to regulate low-voltage-activated $Ca_v3.2$ calcium channels localized to the axon initial segment, which suppressed action potential (AP) excitability, particularly when APs occurred at high frequency. Therefore, these data indicate that D3 receptors

regulate the excitability of a unique, IT prefrontal cell population, thereby defining novel circuitry and cellular actions for D3 receptors in PFC.

Significance Statement

The D3 dopamine receptor, a member of the G_i-coupled D2 family of dopamine receptors, are expressed throughout limbic circuits, including prefrontal cortex (PFC). They are of broad interest as a site for therapeutic intervention in serious mental illness, yet we know very little about their distribution or function within PFC. Here, we show that D3 receptors define a unique population of glutamatergic principal cells in mouse PFC that largely lack expression of D1 or D2 receptors. Within these cells, we find that D3 receptors regulate the ability to generate high-frequency action potential bursts through mechanisms not supported by other dopamine receptors. These results define unique circuitry and cellular actions for D3 receptors in regulating PFC networks.

Introduction

The $G_{i/o}$-coupled D2 family of dopamine receptors is important for normal prefrontal function and dysfunction of these receptors underlies multiple forms of serious mental illness (Minzer et al., 2004; Laruelle, 2014). Although considerable attention has been paid to the function of D2 receptors (D2Rs) themselves, the cellular mechanisms by which other D2-family receptors, including D3 receptors (D3Rs), regulate prefrontal cortex (PFC) neurons remain unclear. D3Rs appear to play an important role in normal PFC function and potentially in mental illness treatment because currently prescribed antipsychotics have equal affinity for D3R and D2R (Joyce

and Millan, 2005; Gross et al., 2013). Moreover, alterations in medial PFC (mPFC)-dependent learning tasks are evident in both D3R knock-out animals and with pharmacological manipulation of prefrontal D3Rs (Glickstein et al., 2002, 2005; Millan et al., 2010; Nakajima et al., 2013). Therefore, determining the cellular substrates of prefrontal D3R modulation and the resulting effects on neuronal computation is essential for our understanding of mPFC function in health and disease.

Major advances in understanding striatal circuitry were made after the discovery that D1 receptors (D1Rs) and D2Rs map onto medium spiny neurons that comprise the direct and indirect pathway (Gerfen and Surmeier, 2011). In prefrontal circuits, parallel observations are beginning to emerge, as recent work indicates that D1R and D2R regulate thin- and thick-tufted layer 5 (L5) pyramidal cells, respectively (Gee et al., 2012; Seong and Carter, 2012). These pyramidal cell subclasses are part of distinct circuits: thin-tufted pyramidal cells are intratelencephalic (IT), with projections to contralateral cortex; thick-tufted pyramidal cells are pyramidal tract (PT), with projections to thalamus and pons, but not contralateral cortex (Dembrow et al., 2010; Gee et al., 2012). Given that D1Rs and D2Rs are expressed in largely separate L5 pyramidal cell subclasses that have unique electrophysiological and morphological features (Gee et al., 2012; Seong and Carter, 2012), we hypothesized that D3R expression may be restricted to one of these subclasses or to an additional subclass with its own electrophysiological signature. However, how D3Rs are incorporated in and regulate the activity of prefrontal neurons is not clear.

Here, we used dopamine receptor reporter lines, anatomical tracing techniques, and electrophysiology to understand D3-dependent regulation in PFC. In contrast to

striatum, which contains only two principle classes of medium spiny neuron, we found that D3R expression defines an additional class of L5 pyramidal cells that largely lack D1R or D2R coexpression. Despite D3R and D1R belonging to different dopamine receptor families (D2-like, D1-like), L5 D3R-expressing neurons were more comparable to D1R-expressing cells in their synaptic connectivity, with projections to IT areas, including contralateral cortex. D3R-expressing neurons could be distinguished from D1R- or D2R-expressing neurons by dendritic morphology and intrinsic electrophysiological properties, and by the manner in which dopamine regulated neuronal function. In these neurons, D3Rs selectively regulated the dynamics of voltage-gated calcium channels localized to the site of action potential (AP) initiation in the axon initial segment (AIS), which in turn led to a marked suppression in the generation of high-frequency AP bursts. Similar signaling mechanisms were not observed in neighboring D1R- or D2R-expressing cells, indicating that D3Rs have a unique role in the regulation of pyramidal cell excitability. Therefore, these results reveal a specific role for D3R signaling in prefrontal networks and highlight new signaling pathways and circuitries that may contribute to antipsychotic efficacy in PFC.

Materials and Methods

Electrophysiological recordings.

All procedures were in accordance with University of California, San Francisco Institutional Animal Care and Use Committee guidelines. After anesthesia, para-coronal slices in plane with mPFC L5 apical dendrites (225–300 μm) were made from postnatal day (P)25–P60 C57 or transgenic mice of either sex. Transgenic animals (TH-Cre::Ai32;

D1-tdTomato/D3-cre; D2-Cre; D3-Cre; D3-Cre::Ai14; D1-tdTomato/D2-eGFP; and $D3^{-/-}$, all on C57 background) were genotyped by PCR. Transgenic mice lines had the following research resource identifiers: TH-cre, IMSR_JAX:008601; D1-tdTomato, IMSR_JAX:016204; D2-Cre, MMRRC_032108-UCD; D2-eGFP, MMRRC_000230-UNC; D3-Cre (KJ302), MMRRC_034696-UCD; $D3^{-/-}$, MGI:4839942. No differences were observed across mouse lines and results were pooled. Cutting solution contained the following (in mM): 87 NaCl, 25 $NaHCO_3$, 25 glucose, 75 sucrose, 2.5 KCl, 1.25 NaH_2PO_4, 0.5 $CaCl_2$ and 7 $MgCl_2$ bubbled with 5%CO_2/95%O_2; 4°C. After cutting, slices were either incubated in the same solution or in the recording solution (see below) for 30 min at 33°C and then at room temperature until recording. Recording solution contained the following (in mM): 125 NaCl, 2.5 KCl, 2 $CaCl_2$, 1 $MgCl_2$, 25 $NaHCO_3$, 1.25 NaH_2PO_4, 25 glucose bubbled with 5%CO_2/95%O_2 at 32–34°C.

Pyramidal cells were visualized with Dodt or differential interference contrast optics; L5 was targeted as the less dense region below L2/3, visualized as the thin band of densely packed somata. For current-clamp recordings, patch electrodes (Schott 8250 glass, 3–4 MΩ tip resistance, <15 MΩ series resistance) were filled with a solution containing the following (in mM): 113 K-gluconate, 9 HEPES, 4.5 $MgCl_2$, 0.1 EGTA, 14 $Tris_2$-phosphocreatine, 4 Na_2-ATP, 0.3 tris-GTP at ~290 mOsm, pH 7.2–7.25. For Ca imaging, EGTA was replaced with 250 μM Fluo-5F and 20 μM Alexa Fluor 594. Electrophysiological data were recorded at 20–50 kHz and filtered at 10 kHz using a Multiclamp 700A or 700B amplifier (Molecular Devices) and acquired with custom routines in Igor Pro (Wavemetrics). For assessing AIS Ca modulation, V_m was held at

−80 mV (corrected for a 12 mV measured junction potential) and cells were excluded if Rin changed by >±15%.

Targeted Ni iontophoresis was done as described previously (Bender et al., 2012) using a Dagan ION-100 (50–100 nA ejection current, −20 nA retention current). Phosphates were omitted from recording solutions to avoid $Ni_3(PO_4)_2$ formation at the electrode tip. Ni application temporally overlapped somatic current or conductance injection. Excitatory postsynaptic conductances were injected in dynamic clamp using an ITC-18 interface as pure AMPA-mediated conductances (0 mV reversal potential, Poisson distributed, τ_{rise} = 0.4 ms, τ_{decay} = 4 ms, amplitude scaled within each experiment to evoke spikes).

For endogenous dopaminergic fiber stimulation, channelrhodopsin-2 (ChR2) was activated by full-field 470 nm light (2 mW at the focal point) using a purpose-built light-emitting diode assembly. Stimuli were delivered in a burst of 10 light pulses at 40 Hz (5 ms per stimulus). These bursts were repeated 10× every 60 s. Because ChR2 is expressed in both dopaminergic and noradrenergic cells in TH-Cre::Ai32 animals, noradrenergic receptors were blocked with 10 μM yohimbine hydrochloride, 1 μM alfuzosis hydrochloride, and 10 μM ICI 118,551 hydrochloride.

For voltage clamp of Ca currents, experiments were performed in D1-tdTomato/D2-eGFP or D3-Cre::Ai14 mice, allowing fluorescent targeting of pyramidal cell subclasses. Internal solution contained the following (in mM): 110 $CsMeSO_3$, 40 HEPES, 1 KCl, 4 NaCl, 4 Mg-ATP, 10 Na-phosphocreatine, 0.4 Na_2-GTP, 0.5 Fluo-5F, and 0.02 Alexa Fluor594 at ~290 mOsm, pH 7.22, voltages adjusted for 11 mV junction potential. Experiments were performed in the presence of 500 nm tetrodotoxin (TTX), 1

mM CsCl, 10 μM SR95531, and 10 μM NBQX. T-type Ca^{2+} currents were activated with 100 ms voltage steps from −100 to −50 mV. For T-type current measurements, leak currents were subtracted using a P/4 protocol with −12.5 mV steps from −80 mV.

Electrophysiological analysis for classification.

Electrophysiological characteristics (sag/rebound, AP spike train/waveform) were determined from voltage responses to hyperpolarizing (−400 pA, 120 ms) and depolarizing (300 ms, 20–300 pA) square current pulses from a holding potential of −80 mV.

Latency to peak sag was calculated as the time from current pulse onset to the negative peak of the voltage. Sag amplitude was defined as the amplitude of a one-term exponential model fit to the voltage between peak sag onset and the end of the current pulse. Latency to peak rebound was defined as the time from the end of the current pulse to the maximum voltage within 100 ms of pulse offset. Rebound time constant was defined as the duration after current offset for a voltage increase from 20–80% of the difference between the peak rebound voltage and the voltage at current offset.

AP threshold was defined as the voltage at which the first derivative of the membrane potential exceeded 15 V/s (McCormick et al., 2007). AP amplitude was calculated as the difference between the maximum AP membrane potential and AP threshold. The rate of the AP rising, rate of AP falling, and spike width were all calculated at 20% of AP amplitude for the given amplitude, with rates calculated as the first derivative of membrane potential with respect to time. Afterhyperpolarization (AHP)

potential of APs in a spike train was defined as the minimum voltage between APs. A doublet index was calculated as the ratio of the second to first interspike interval.

Linear discriminant analysis (LDA): model development and application.

Five features were chosen for LDA: sag amplitude, rebound time constant, the log of the doublet index, rate of AP rising phase for the last AP in the spike train, and difference in AP threshold between first and last AP. None of these variables was tightly correlated (defined as $r^2 > 0.5$ and $p < 0.05$) or strongly non-normal (Lilliefors test, $p < 0.001$). Variables were standardized by rescaling to have a mean of zero and an SD of one.

Twelve classifiers were created using the machine learning toolbox (MATLAB), depending on Ca buffer in the recording pipette (EGTA or Fluo-5F) and number of APs evoked in 300 ms (3–8 APs). Repeated holdout cross-validation (2000×) validated the discriminant functions. For each iteration, data were randomly partitioned into a training set (90%) and a testing set (10%), with the linear discriminant determined by the training set then applied to the testing set. Prediction accuracy was averaged across rounds, defined as the percentage of cells correctly identified in the testing set. Prediction accuracy was increased by defining an “exclusion zone,” determined by the Gaussian fit of the D1+ and D3+ cell class' Euclidean distances from the discriminant hyperplane (i.e., decision boundary). The exclusion zone was defined such that only nonlabeled cells with distances from the boundary outside of the 95th percentile of the other cell class' distribution were classified as “Type 1” or “Type 3” (see Fig. 2D). The final set of classifiers was applied to all nongenetically identified cells to predict D1R or

D3R expression. Each cell was tested on all relevant classifiers, depending on Ca buffer and AP spike number. Cells were included in subsequent analysis if they were classified outside the exclusion zone and did not have their designation switch from Type 1 to Type 3 (or vice versa) between classifiers.

Laminar distribution and orthograde/retrograde tracing.

Before all viral injections, mice were anesthetized and positioned in a stereotaxic frame. For laminar expression experiments, P28–P35 D1-tdTomato/D3-cre or D2-cre mice were injected bilaterally with large volumes (750–1000 nl) of either AAV-EF1α-DIO-EYFP or AAV-EF1α-DIO-mCherry in the mPFC (stereotaxic coordinates [mm]: anteriorposterior [AP], +1.7, mediolateral [ML] +/− 0.3; dorsoventral [DV]: −2.75). Four to 5 weeks after injection, animals were fixed with 4% paraformaldehyde in PBS via transcardial perfusion. After full brain fixation (4 h), 50 μm coronal sections of the mPFC were made in PBS using a vibratome.

In preparation for anti-RFP immunohistochemistry, free-floating coronal sections were rinsed with PBS (3×) and blocked 1 h at room temperature (BlockAid blocking solution). Sections were incubated overnight at 4°C in primary antibody (mouse anti-RFP, 1:500) in PBS-T (PBS with 0.1% Triton X-100) with 1% normal goat serum. Sections were then rinsed with PBS-T and incubated in secondary antibody (Alexa Fluor 594 goat anti-mouse, 1:500) with PBS-T for 4 h at room temperature. After PBS rinse, sections were coverslipped with Prolong Gold Antifade reagent with DAPI. To visualize laminar distributions of D1R, D2R, or D3R expression, fluorescence of mPFC sections was acquired with a spinning disk confocal microscope (10× objective, 0.3

numerical aperture, NA). Somatic fluorescence expression was assessed with a z-series from a 500 × 800 μm area of mPFC (long axis perpendicular to midline pia).

For analysis of cellular laminar distributions, laminar depths were used as defined previously by the L3 and L5b markers Cux1 and Ctip2. Given variability in L1 depth, laminar boundaries were defined with respect to the L1/2 border, visualized with DAPI. The bottom of L2/3, L5a, and L5b were defined as 119, 241, and 534 μm from the L1/2 border, respectively (DeNardo et al., 2015).

For orthograde tracing experiments, P28 D3-Cre::Ai14 mice were injected with 300 nl of AAV- EF1α-DIO-ChR2-EYFP in the mPFC (coordinates as above). Three weeks after injection, animals were perfused and the full brain fixed overnight. Then, 50-μm-thick coronal sections of the entire brain were obtained. To assess axonal projection patterns, fluorescent images were taken with a high-speed wide-field microscope (Nikon Ti with Andor Zyla 5.2 camera, 10× objective, 0.45 NA) and then digitally stitched with ImageJ to reconstruct each full coronal section.

For retrograde tracing experiments, P52+ D3-Cre::Ai14 mice were injected with 200–300 nl of Alexa Fluor 488 conjugated to cholera toxin subunit B (Ctb-488) in the mPFC (coordinates as above), nucleus accumbens core (NAcc) (AP, +1.5; ML, −1.3; DV, −4.38), basolateral amygdala (BLA) (AP, −1.55; ML, −2.95; DV, −5), or mediodorsal (MD) thalamus (AP, −1.7; ML, −0.3; DV, −3.45). Then, 3–4 d after injection, animals were perfused, the full brain fixed overnight, and 50-μm-thick coronal mPFC sections were obtained. In a subset of animals, paracoronal slices were prepared containing mPFC and slices were fixed, cryoprotected in a sucrose–PBS solution, and then sectioned on a freezing stage microtome at 50 μm after a recording session. In both

cases, the injection site was verified in 75 μm coronal sections. To examine colabeling of Ai14 marker and retrograde tracer, fluorescence of mPFC sections was acquired with a confocal microscope (10× objective, 0.45 NA). Ai14/Ctb-488 coexpression was assessed with a z-series taken of a 400–500 μm swath of mPFC up to 800 μm from the pia. Analysis of laminar distribution was done as described above.

Two-photon imaging.

A two-photon imaging system (Prairie Technologies) was used as described previously (Bender et al., 2010). A Chameleon Ultra II laser (Coherent Technologies) was tuned to 810 nm. Epifluorescence and transfluorescence signals were captured through a 60×, 1.0 NA objective and a 1.4 NA oil-immersion condenser (Olympus). Fluorescence was split into red and green channels using dichroic mirrors and band-pass filters (T560LPXR, ET525/50, ET620/60; Chroma). Green fluorescence (Fluo-5F) was captured with H10770PA-40 photomultiplier tubes (PMTs; Hamamatsu). Red fluorescence (Alexa Fluor 594) was captured with R9110 PMTs. Data are presented as averages of 10–20 events per site and are expressed as $\Delta(G/R)/(G/R)_{sat} * 100$ (simply, $\Delta(G/G_{sat})$, where $(G/R)_{sat}$ was the maximal fluorescence in saturating Ca^{2+} (2 mM). Ca^{2+} transient peaks were calculated from exponential fits to the fluorescence decay after stimulus offset. Two-photon imaging was performed in P30–P45 mice.

Chemicals.

Fluo-5F pentapotassium salt, Alexa Fluor 594 hydrazide Na+ salt, cholera toxin conjugated to Alexa Fluor 488, and Alexa Fluor 594 goat anti-mouse secondary

antibody were from Invitrogen. BlockAid blocking solution was from Thermo Fisher Scientific. Anti-RFP (mouse) monoclonal antibody was obtained from Rockland Immunochemicals (200–301-379). Prolong Gold Antifade reagent with DAPI was from Invitrogen. All AAV vectors were obtained from the University of North Carolina vector core. SR95531, R-CPP, NBQX (−)-quinpirole hydrochloride, TTX, and GR103691 were from Tocris Bioscience. All others were from Sigma-Aldrich.

Statistics.

All data are shown as mean ± SEM. Depending on data distributions, an ANOVA followed by multiple two-sample t tests or Kruskal–Wallis followed by Wilcoxon's rank-sum test (Holm–Sidak corrections for multiple comparisons) was used unless otherwise noted (significance: $p < 0.05$). For the Wilcoxon's rank-sum test, z-statistics are given for large sample sizes ($n > 20$); otherwise, the rank-sum test statistic (W) is reported.

Results

D3Rs are expressed in a distinct subset of mPFC pyramidal cells

To determine how D3Rs are distributed relative to known pyramidal cell classes in mPFC, we visualized the distribution of fluorescently labeled pyramidal cells across mPFC layers using previously described border demarcations (Hooks et al., 2011; DeNardo et al., 2015) and dopamine-receptor-specific reporter mice (D1-tdTomato/D2-GFP or D1-tdTomato/D3-cre mice, as well as D2-Cre or D3-Cre mice either crossed to Ai14 or injected with a DIO-EYFP or DIO-mCherry virus). D1R- and D2R-expressing (D1+, D2+) pyramidal cells have been identified previously in L5, with

morphological features consistent with thin- and thick-tufted pyramidal classes, respectively (Gee et al., 2012; Seong and Carter, 2012). Consistent with this, D1+ and D2+ neurons were identified in L5. In addition, D1+ and D2+ neurons were observed in L2/3. D2+ neurons were most heavily concentrated in L5b, with lower relative abundance in L5a. In contrast, D3R-expressing (D3+) neurons were concentrated within the upper cortical layers to the L5a/L5b border, with relatively low expression below (Fig. 1A).

That D1+, D2+, and D3+ neurons are distributed in distinct lamina suggests that they are restricted to separate mPFC pyramidal cell classes. To determine whether dopamine receptor expression correlates with electrophysiological or morphological characteristics, whole-cell current-clamp recordings were made from each of these cell classes and a series of hyperpolarizing and depolarizing pulses were delivered to examine subthreshold and suprathreshold voltage responses. Cells were simultaneously filled via patch pipettes with the red volume marker Alexa Fluor 594 and two-photon-based z-stacks were acquired over the entire dendritic span, allowing for post hoc morphological reconstruction.

Previous studies have shown that different prefrontal pyramidal cell classes express varying degrees of hyperpolarization-activated cyclic nucleotide-gated (HCN) channels, which can influence resting membrane properties (Dembrow et al., 2010; Gee et al., 2012; Seong and Carter, 2012). We found that D1+, D2+, and D3+ neurons had different input resistances when subjected to a −50 pA current pulse (D1+: 183 ± 5 MΩ, n = 95; D2+: 146 ± 11 MΩ, n = 35; D3+: 212 ± 5 MΩ, n = 188; Kruskal–Wallis, $H_{(2)} = 32.91$, $p = 7 \times 10^{-8}$; Wilcoxon's rank-sum test, Holm–Sidak correction, D1+

vs D2+: $z = 3.75$, D1+ vs D3+: $z = -3.32$, D2+ vs D3+: $z = -5.01$; $p < 0.05$) and that D2+ cell resting V_m was modestly depolarized relative to D3+ cells (D1+: −80.0 ± 0.6 mV; D2+: −77.9 ± 0.7 mV; D3+: −80.2 ± 0.4 mV; Kruskal–Wallis, $H_{(2)} = 7.26$, $p = 0.027$; Wilcoxon's rank-sum test, Holm–Sidak correction, D2+ vs D3+: $z = 2.76$; $p < 0.05$; Fig. 1D). Intrinsic membrane properties were stable within each class across the age range studied, consistent with other reports in rodent neocortex (McCormick and Prince, 1987; Zhang, 2004; linear regression of V_m or R_{in} vs age for D1+/D2+/D3+: $r^2 < 0.01$, $p > 0.4$).

Larger current pulses (−400 pA) more effectively recruit HCN current and reveal different response properties across dopamine-receptor-expressing classes. Consistent with other reports from D2+ neurons (Gee et al., 2012), 74% of D2+ neurons exhibited a prominent voltage sag during hyperpolarizing pulses and had a voltage rebound that depolarized past rest after current offset. A far lower proportion of D1+ and D3+ neurons had similar response properties (4% and 6%, respectively, defined by a peak rebound voltage occurring within 90 ms of current offset; Fig. 2A: rebound: n = 85/35/185, D1+/D2+/D3+; Kruskal–Wallis, $H_{(2)} = 67.01$, $p = 3 \times 10^{-15}$; Wilcoxon's rank-sum test, Holm–Sidak correction, D1+ vs D2+: $z = 5.89$, D1+ vs D3+: $z = -4.55$, D2+ vs D3+: $z = -7.08$; sag: n = 95/35/188, D1+/D2+/D3+; Kruskal–Wallis, $H_{(2)} = 90.23$, $p = 3 \times 10^{-20}$; Wilcoxon's rank-sum test, Holm–Sidak correction, D1+ vs D2+: $z = 6.06$, D1+ vs D3+: $z = -5.51$, D2+ vs D3+: $z = -8.34$). Therefore, we used these response properties to classify cells that likely express D2Rs, but lack D1Rs and D3Rs (termed Type 2).

To determine whether non-Type 2 neurons had electrophysiological phenotypes that correlated with D1R and D3R expression, we examined additional aspects of their

intrinsic excitability. We found that multiple features differed across D1+ and D3+ groups; however, no single electrophysiological property was sufficient to discriminate these groups well. Therefore, we applied LDA to determine whether a combination of features would better distinguish D1+ and D3+ neurons. We chose five electrophysiological properties that allowed for maximal separation of D1+ and D3+ populations (Fig. 2C). These included sag amplitude in response to −400 pA current steps, rebound time constant during recovery from these current steps, and three spiking properties (AP rate of rise, threshold, and changes in interspike interval during an AP train). Compared with D1+ neurons, D3+ neurons had lower sag and slower rebound recovery after −400 pA current pulses (sag, D1+: −2.7 ± 0.1 mV, n = 92; D3+: −1.9 ± 0.1 mV, n = 176; two-sample t test, $t_{(266)} = -4.62$, $p = 6 \times 10^{-6}$; rebound τ, D1+: 30.1 ± 0.6 ms; D3+: 35.7 ± 0.4 ms; two-sample t test, $t_{(266)} = -7.56$, $p = 7 \times 10^{-13}$). In addition, D3+ neurons had a lower instantaneous spike frequency at train onset, slower AP rise times, and a larger increase in AP threshold of successive spikes in trains (Fig. 2B,C: statistics for classifier shown; two-sample t tests, n = 47/72, D1+/D3+; rebound: $t_{(118)} = -7.24$, $p = 5 \times 10^{-11}$; sag: $t_{(118)} = -3.77$, $p = 3 \times 10^{-4}$; doublet index: $t_{(118)} = 7.49$, $p = 1 \times 10^{-11}$; AP rate of rise: $t_{(118)} = 6.98$, $p = 2 \times 10^{-10}$; ΔThreshold: $t_{(118)} = -7.65$, $p = 6 \times 10^{-12}$). Additional features also differed across these populations, but they tended to covary with parameters already included in the analysis and therefore did not improve discriminability (Fig. 3).

Using these features, we created multiple LDA classifiers to assess the electrophysiological discriminability of these populations and to allow for classification of nonfluorescent neurons (see Materials and Methods, Fig. 2, Tables 1 and 2). To

evaluate our electrophysiological model's performance, we implemented holdout cross-validation and found that the classifiers' mean accuracies in predicting D1R or D3R expression always exceeded 70% (D1+ range: 80–93%, median: 87%; D3+ range: 72–87%, median: 80%, Fig. 2E). These data indicate that pyramidal cells expressing different dopamine receptors tend to have distinct intrinsic electrophysiological phenotypes and that D1+ and D3+ neurons comprise generally nonoverlapping populations. We confirmed this separation by injecting D1-tdTomato/D3-cre mice with an AAV vector containing Cre-dependent EYFP, enabling simultaneous visualization of D1R and D3R expression via tdTomato and EYFP fluorescent markers, respectively (Fig. 4A). Consistent with electrophysiological analysis, D1+ and D3+ cells were largely separate populations, with >90% of labeled cells within L5 uniquely expressing the D1R or D3R (Fig. 4C).

The ability to identify accurately neurons likely to express a given dopamine receptor based solely on electrophysiological characteristics would be useful for assessing dopaminergic function in cases in which fluorescent reporters are not available. To enhance the prediction accuracy that a neuron's electrophysiological signature indeed corresponds to expression of D1R or D3R, we defined an “exclusion zone,” an area surrounding the decision boundary defined by the discriminant, in which D1+ and D3+ cell classes' electrophysiology overlapped (see Materials and Methods; Fig. 2D). Across all classifiers, this yielded a median accuracy of >90% for both D1+ and D3+ cells when tested on the final classifier that included all genetically identified cells (Fig. 2E). Therefore, by rejecting a subset of cells with overlapping electrophysiological characteristics, D1+ and D3+ cells can be categorized with high

accuracy. We then applied this final set of classifiers to all non-Type 2, nongenetically identified neurons, categorizing them as Type 1, Type 3, or “unidentified.” By this method, 89% of 103 neurons analyzed were categorized as Type 1 or Type 3.

After electrophysiological characterization of D1+, D2+, and D3+ cell classes, we analyzed our post hoc morphological reconstructions to determine whether these cell classes were also morphologically distinct. D1+ neurons had relatively simple apical dendritic morphology (Fig. 1B, Table 3), consistent with previous reports of D1+ “thin-tufted” pyramidal cells (Seong and Carter, 2012). D2+ neurons had much more complex apical tuft morphology, both with respect to their broad span as well as overall apical dendritic length and branch points, similar to the “thick-tufted” D2+ neurons described previously (Gee et al., 2012). In contrast, D3+ pyramidal cells in L5 had a morphology that was intermediate to D1+ and D2+ neurons; they had an apical tuft that spanned a similar distance as D2+ pyramidal cells, but had branching and dendritic arbor length more comparable to D1+ neurons. In addition, for most morphological measures, D3+ and Type 3 neurons (genetically unlabeled) were identical (Table 3). Overall, these data suggest that there are electrophysiologically and morphologically distinct L5 pyramidal cell classes in mPFC and that these different classes correlate with expression of the D1, D2, and D3 receptors.

L5 D3+ pyramidal neurons are an IT, cortically projecting neuronal subtype

Cortical pyramidal neurons are categorized into two broad projection classes: IT, cortically projecting neurons and PT, subcortically projecting neurons. Whereas IT neurons are distributed throughout L5, PT neurons are restricted to L5b (Molnár and

Cheung, 2006; Shepherd, 2013). In the mPFC, L5 D1+ and D2+ neurons correspond to IT and PT subtypes, respectively, with D1R-expressing cells projecting to contralateral cortex and D2R-expressing cells projecting subcortically (Dembrow et al., 2010; Gee et al., 2012). Interestingly, although D3Rs are a member of the D2 family, their density in L5b is low. This suggests that they may have different long-range synaptic targets than other types of D2-family-expressing neurons.

To determine the downstream targets of D3+ pyramidal neurons, we injected DIO-ChR2-EYFP into the mPFC of D3-Cre mice (Fig. 5A), allowing visualization of axonal projections throughout the brain. Axons were prominent in the contralateral mPFC, bilateral BLA, bilateral ventral striatum, including the NAcc, and both MD and ventromedial thalamus (Fig. 5B–D), indicating that D3+ neurons project to diverse cortical and subcortical targets. However, viral transfection was not limited to D3+ neurons in L5; rather, D3+ neurons throughout cortical lamina were transfected (Fig. 5A). Therefore, we complemented these orthograde tracing experiments with injections of fluorescently conjugated cholera toxin B, which incorporates into axonal terminals and transports retrogradely to somata. Alexa Fluor 488 conjugated cholera toxin was injected into four putative downstream targets in D3-Cre::Ai14 animals: contralateral mPFC and ipsilateral BLA, NAcc, and MD thalamus (Fig. 6A, insets). We then examined the extent and laminar distribution of overlap between D3+ and retrogradely labeled cell populations (Fig. 6). Using these methods, we identified a substantial L5 D3+ projection to both the NAcc and the contralateral mPFC. Indeed, the probability that a cell projected to the NAcc or mPFC, given that it was D3R-expressing, was ~52% and ~24%, respectively. In contrast, there was <10% probability that a D3+ L5 cell projected

to the MD thalamus, a target of D2+ L5 neurons (Gee et al., 2012; Fig. 6C: n = 7/10/8/9, mPFC/NAcc/BLA/MD; ANOVA, $F_{(3,30)} = 39.24$, $p = 2 \times 10^{-10}$; two-sample t test, Holm–Sidak correction, mPFC vs NAcc: $t_{(15)} = -4.77$, mPFC vs BLA: $t_{(13)} = 3.10$, mPFC vs MD: $t_{(14)} = 3.78$, NAcc vs BLA, $t_{(16)} = 7.76$, NAcc vs MD: $t_{(17)} = 8.55$; $p < 0.05$). Therefore, though both D2R and D3R are of the same receptor family, they have distinct downstream targets. Instead, L5 D3+ and D1+ neurons share a common projection to contralateral cortex, suggesting that corticocortical networks can be modified by both G_s- and G_i-coupled dopamine receptor classes.

Dopamine regulates AIS Ca and burst initiation in D3R-expressing neurons

Recently, we found that D3Rs regulate a subset of Ca channels expressed in the AIS of auditory brainstem interneurons. Because pyramidal cells also express Ca channels in the AIS (Bender and Trussell, 2009; Yu et al., 2010), we investigated whether D3Rs had a similar function in the mPFC. Spike trains were evoked with somatic current injection (3×50 Hz, 1.5–2 nA, 2 ms per stimulus) and resultant axonal Ca transients were imaged 25–35 μm distal to the axon hillock. AIS Ca channel modulation was then assessed with the D2/D3R agonist quinpirole (2 μM) in the presence of 10 μM NBQX, 10 μM R-CPP, and 10 μM SR-95531. Although spike-evoked Ca influx was observed in the AIS of all three pyramidal subclasses, Ca influx was modulated only in fluorescently tagged D3+ neurons or neurons classified as Type 3 (Fig. 7B: normalized $\Delta G/G_{sat}$, D1+: 0.98 ± 0.02, n = 10; Type 2: 1.00 ± 0.03, n = 4; D3+: 0.69 ± 0.03, n = 10; Type 3: 0.72 ± 0.03, n = 10; D3+ or Type 3 vs D1+ and Type 2; $p < 0.05$; ANOVA, two-sample t tests, Holm–Sidak correction; see below for statistics).

Quinpirole had no effect on AIS Ca in Type 3 neurons in $D3R^{-/-}$ mice or in wild-type mice in the presence of the D3R antagonist GR103691 (5 μM) (Fig. 7B: normalized $\Delta G/G_{sat}$, $D3R^{-/-}$: 1.02 ± 0.03, n = 5; GR103691: 0.98 ± 0.04, n = 4; $p < 0.05$ vs quinpirole alone [statistical values for all comparisons shown in Fig. 7B: ANOVA, $F_{(6,41)} = 25.19$, $p = 3 \times 10^{-12}$; two-sample t test, Holm–Sidak correction, Type 3 quinpirole vs Type 3 GR103691 + quinpirole, $t_{(12)} = -4.51$, Type 3 quinpirole vs Type 3 $D3^{-/-}$ + quinpirole, $t_{(13)} = -5.90$, Type 3 quinpirole vs Type 3 $Ca_V3.2^{-/-}$ + quinpirole, $t_{(13)} = -4.85$, Type 3 quinpirole vs D1+ quinpirole, $t_{(18)} = 7.05$, Type 3 quinpirole vs Type 2 quinpirole, $t_{(12)} = 5.02$, D3+ quinpirole vs Type 3 GR103691 + quinpirole, $t_{(12)} = -5.88$, D3+ quinpirole vs Type 3 $D3^{-/-}$ + quinpirole, $t_{(13)} = -7.54$, D3+ quinpirole vs Type 3 $Ca_V3.2^{-/-}$ + quinpirole, $t_{(13)} = -6.23$, D3+ quinpirole vs D1+ quinpirole, $t_{(18)} = 9.00$, D3+ quinpirole vs Type 2 quinpirole, $t_{(12)} = -6.51$]). Furthermore, AIS Ca was sensitive to endogenous dopamine because optogenetic stimulation of endogenous TH+ fibers was sufficient to alter AIS Ca transients (TH-Cre::Ai32 mice, see Materials and Methods, Fig. 7C; normalized $\Delta G/G_{sat}$, ChR2 stimulation alone: 0.75 ± 0.04, n = 8; stimulation in 1 μM sulpiride: 0.93 ± 0.03, n = 4; Wilcoxon's rank-sum test: W = 40, p = 0.04).

In previous work in auditory brainstem, we found that D3Rs specifically modulate Ca_V3 calcium channels (Bender et al., 2010; Yang et al., 2016). Here, we found that AIS Ca was modulated only in D3+/Type 3 cells. This may reflect selective expression of Ca_V3 channels in this cell class and not in D1+ or D2+ cells. To test this, we made voltage-clamp recordings with Cs-based internal, 500 nM TTX, and 1 mM Cs to block K, Na, and HCN channels, respectively, and imaged Ca influx in the AIS of fluorescently tagged cells (Fig. 7D). Putative Ca_V3 current was isolated with voltage steps from −100

mV to −50 mV. Interestingly, all 3 cell classes displayed comparable levels of AIS Ca influx (D1+: 3.6 ± 0.6, n = 6; D2+: 3.5 ± 0.4, n = 3; D3+: 3.4 ± 1.2, n = 8; $\Delta G/G_{sat}$, ANOVA, p = 0.99) even though whole-cell Ca_V3 currents were smaller in D3+ cells (D1+: −292 ± 35 pA; D2+: −271 ± 58 pA; D3+: −148 ± 15 pA; ANOVA, $F_{(2,14)} = 8.03$, p = 0.005; two-sample t test, Holm–Sidak correction, D1+ vs D3+: $t_{(12)} = -4.14$, D2+ vs D3+: $t_{(9)} = -2.98$; $p < 0.05$). Whole-cell current and imaged Ca transients were sensitive to the selective Ca_V3 antagonist TTA-P2 (1 μM), indicating that Ca_V3 channels are found throughout dendritic and AIS compartments in all classes (Fig. 7D,E). Despite similar AIS Ca channel expression across cell classes, quinpirole-dependent modulation was observed only in the AIS of D3+ neurons (D3+ AIS G/G_{sat}: 60 ± 5% of baseline; ANOVA, D1+/D2+/D3+, $F_{(2,14)} = 13.38$, $p = 6 \times 10^{-4}$; two-sample t test, Holm–Sidak correction, D1+ vs D3+: $t_{(12)} = 5.90$, D2+ vs D3+: $t_{(9)} = 3.25$; $p < 0.05$). Consistent with these voltage-clamp results, 1 μM TTA-P2 reduced spike-evoked Ca influx in current-clamp recordings from Type 3 neurons (Fig. 7C: normalized $\Delta G/G_{sat}$: 0.67 ± 0.03, n = 5). Quinpirole did not alter AIS Ca after TTA-P2 application or in $Ca_V3.2$ knock-out mice, indicating that $Ca_V3.2$ isoforms are the target of D3R modulation (Fig. 7B,C: normalized $\Delta G/G_{sat}$, quinpirole in TTA, normalized to pre-TTA baseline: 0.66 ± 0.02, n = 5, Wilcoxon's signed-rank test vs TTA baseline: p = 0.44; $Ca_V3.2^{-/-}$: 0.98 ± 0.04, n = 5, $p < 0.05$). Overall, these data indicate that, whereas AIS Ca channels are common to multiple neuron classes (Bender and Trussell, 2009; but see Yu et al., 2010), they are subject to AIS neuromodulation only in neurons that coexpress D3R and these cells can be distinguished based on electrophysiological properties.

Ca_V3 channels underlie burst generation in multiple cell classes (Williams and Stuart, 1999; Cain and Snutch, 2010) and modulating AIS Ca_V3 channels can suppress both evoked and spontaneous spike burst generation in cartwheel cells (Bender et al., 2010, 2012). Because bursts initiate in the AIS of pyramidal neurons (Kole, 2011), we hypothesized that AIS Ca channel modulation could suppress burst firing in D3+ cells. To test this, we first suppressed AIS Ca influx during evoked spike trains with targeted iontophoresis of the Ca channel antagonist Ni. In these experiments, control and Ni-paired bursts were interleaved and iontophoretic intensity was calibrated to match the relative reduction in AIS Ca influx observed after dopaminergic modulation (Fig. 8A–D). This partial block of AIS Ca_V channels is a good approximation of the actions of D3R because we showed recently that D3R signaling acts to hyperpolarize voltage-dependent steady-state inactivation of AIS-localized $Ca_V3.2$ channels (Yang et al., 2016). This reduces channel availability at resting V_m and is therefore similar to antagonist block. Local Ca influx in response to a train of APs (3 × 50 Hz) was reduced to 0.61 ± 0.02 of baseline when Ni iontophoresis was focused on the AIS (n = 8). AIS Ca was not altered if the pipette was targeted to a neighboring basal dendrite 15–20 µm from the AIS, suggesting that Ni iontophoresis can be restricted to a small volume (Fig. 8C: 1.04 ± 0.03 of baseline, n = 4; Wilcoxon's rank-sum test, AIS vs dendrite Ni: W = 36, p = 0.004).

After calibration of Ni iontophoretic intensity, stimuli were switched from APs to trains of Poisson-distributed idealized excitatory postsynaptic conductances (EPSGs), which were adjusted in amplitude to evoke a mix of single spike and burst events throughout the train. The same EPSG stimulus was then delivered repeatedly, paired

with or without Ni application in an interleaved fashion. When Ni iontophoresis was applied to the AIS, a modest reduction in the number of events was observed (Fig. 8E: 0.82 ± 0.05 events per epoch, relative to baseline, n = 6; “events” defined as either a single spike or spike burst with an interspike interval <20 ms). In contrast, no change in event frequency was observed if Ni was applied to a neighboring dendrite (1.02 ± 0.03, n = 3; p = 0.02 vs AIS application, Wilcoxon's rank-sum test, W = 24). This event reduction was due to a selective loss of high-frequency bursts; burst occurrence was markedly reduced by AIS Ni (Fig. 8G: AIS Ni: 0.28 ± 0.08 of baseline; dendrite Ni: 0.91 ± 0.1; Wilcoxon's rank-sum test, W = 21, p = 0.02), whereas the single spike rate was unchanged (Fig. 8F: AIS Ni: 1.03 ± 0.09 of baseline, dendrite Ni: 1.03 ± 0.04; Wilcoxon's rank-sum test, p = 0.43). Similarly, D3R-dependent modulation also reduced event output through a selective suppression of bursts and these effects were blocked by preapplication of sulpiride (events, quinpirole: 0.79 ± 0.06 of baseline, n = 5; events, sulpiride + quinpirole: 1.05 ± 0.05, n = 5, Wilcoxon's rank-sum test: W = 16, p = 0.016; bursts, quinpirole: 0.14 ± 0.09; bursts, sulpiride + quinpirole: 1.08 ± 0.11, Wilcoxon's rank-sum test: W = 15, p = 0.008; single spikes, quinpirole: 0.90 ± 0.08; single spikes, sulpiride + quinpirole: 1.02 ± 0.09, Wilcoxon's rank-sum test: p = 0.22). This suggests that regulation of AIS Ca influx is a critical determinant for AP burst output in D3+ neurons and that D3Rs can regulate selectively the temporal features of spike output from this pyramidal cell class.

Discussion

Although the D3R has been observed previously in L5 PFC in both primate and rodent (Bouthenet et al., 1991; Lidow et al., 1998) and has a role in prefrontal-dependent behaviors (Nakajima et al., 2013), how it regulates neuronal function has been unclear. Combining electrophysiological and imaging approaches, we identified a novel class of IT neurons in which D3Rs regulated neuronal excitability at the AIS. Using a supervised machine learning approach, we found that dopamine receptor expression (D1, D2, D3) strongly predicted the subthreshold and suprathreshold electrophysiological properties of mPFC neurons. Dopamine receptor expression correlated with morphological differences between the subtypes, as well as differences in laminar distribution. D3+ cells were further distinguished from D2+ cells by their axonal projection targets. Although D2+, Type 2 neurons targeted subcortical regions such as the pons and thalamus, D3+ neurons had projection patterns more consistent with D1+ neurons, including projections to contralateral mPFC and bilateral NAcc and BLA (Dembrow et al., 2010; Gee et al., 2012; Seong and Carter, 2012; Land et al., 2014). Based on these results, we propose that D1R, D2R, and D3R expression defines largely distinct L5 pyramidal cell classes in mPFC, each with unique catecholaminergic responses.

Cell-class-specific function of neuromodulatory receptors

Although we describe three prefrontal L5 pyramidal neuron subtypes, prior studies largely focused on two subtypes: thick-tufted PT neurons with regular firing and large voltage sag and thin-tufted IT neurons with spike adaptation and low voltage sag

(Morishima and Kawaguchi, 2006; Dembrow et al., 2010; Gee et al., 2012; Seong and Carter, 2012). D3+ neurons are likely a subset of the previously described IT neurons and were identified by characterizing multiple electrophysiological parameters. This is consistent with other recent studies reporting heterogeneity in cortically projecting, low-voltage-sag subtypes, in which both intrinsic firing patterns and response to neuromodulators help to describe two to three distinct groups (Otsuka and Kawaguchi, 2011; Avesar and Gulledge, 2012; van Aerde et al., 2015).

Although we found that D1+, D2+, and D3+ pyramidal neurons were generally distinct cell classes, we did identify a fraction of genetically labeled neurons (~14%) that had an electrophysiological phenotype not predicted by their fluorescent marker (Fig. 2F). These cross-classified cells may represent a subset of cells that coexpress dopamine receptors because colabeled cells were also observed in D1-tdTomato/D3-cre animals (29% of D3+ cells and 9% of D1+ cells). Coexpression of D1R and D2R occurs in a similar fraction of cells in areas of the ventral striatum, including the NAc core and shell (Bertran-Gonzalez et al., 2008). Although coexpressing neurons comprise a small fraction of the pyramidal cell population in mPFC, further work will be needed to determine whether dopamine affects these neuronal populations differently than those that express a single dopamine receptor. In addition, all five dopamine receptor subtypes are expressed in L5 PFC (Lidow et al., 1998). D4 and D5 reporter lines suggest that both receptors localize to cells in L5b and L6 and colabeling studies in nonhuman primates indicate that D1 and D5 colabel pyramidal cells (Bergson et al., 1995; Gong et al., 2003; Noaín et al., 2006). How these different distributions of dopamine receptors contribute to PFC processing will be important to determine.

The mPFC also receives convergent input from numerous ascending neuromodulatory pathways, including serotonergic, cholinergic, and adrenergic afferent systems. Our study adds to growing evidence that modulatory regulation of prefrontal neurons depends strongly on their long-range targets (Dembrow and Johnston, 2014). For example, pyramidal cell integration of serotonergic input is also subtype specific, with excitatory and biphasic responses to serotonin by IT neurons via 5-HT2A receptors and purely inhibitory responses by PT neurons via 5-HT1A receptors (Avesar and Gulledge, 2012). This result suggests the PT D2+ subtype may coexpress the 5-HT1A receptor, whereas D1+ and/or D3+ subtypes may coexpress the 5-HT2A receptor. In addition, IT and PT mPFC neurons also undergo differential adrenergic and cholinergic modulation, with both neuromodulators having larger effects on PT cell excitability, in part through HCN channels that are expressed at higher levels in PT cells (Dembrow et al., 2010). Determining the overlap or segregation of these subcircuits within the mPFC will advance our understanding of how concerted actions by neuromodulators affect prefrontal network activity.

Implications for mPFC D3 receptor function in health and disease

An analysis of mPFC pyramidal cell subclass anatomy and electrophysiology, combined with the functional analysis of D3R here and D1R/D2R in previous work (Gee et al., 2012; Seong and Carter, 2012), revealed that some cell-intrinsic aspects of dopaminergic modulation in mPFC are subclass dependent. Although Ca_V3-mediated AIS Ca influx was present in all three cell classes (Fig. 7, but see Yu et al., 2010), channel modulation occurred only in D3R-expressing neurons, identified either through

fluorescent tag (D3-Cre::Ai14) or electrophysiological identification (Type 3). Modulation was restricted to AIS-localized Ca_V3 channels, consistent with previous findings in D3R-expressing auditory brainstem neurons (Bender et al., 2010, 2012; Yang et al., 2016). Within these neurons, we observed a marked reduction of both evoked and spontaneous bursts (Bender and Trussell, 2009; Bender et al., 2012). Here, we find similar effects in D3+ mPFC pyramidal cells (Fig. 8). AIS Ca channels are common to broad neuronal classes (Schiller et al., 1995; Callewaert et al., 1996; Lüscher et al., 1996; Bender and Trussell, 2009; Yu et al., 2010; François et al., 2015; Gründemann and Clark, 2015; Martinello et al., 2015; Apostolides et al., 2016) and D3Rs are broadly distributed, especially in limbic regions (Bouthenet et al., 1991; Lévesque et al., 1992, also see Fig. 5). Therefore, AIS Ca modulation may be a common mechanism by which D3Rs regulate neuronal excitability throughout the brain.

In vivo, prefrontal neurons exhibit sparse AP firing, interspersed with short, high-frequency bursts (Boudewijns et al., 2013). Selective reduction of AP burst output in D3R-expressing neurons provides a novel mechanism for dopaminergic modulation to regulate mPFC information processing because both behavioral and physiological evidence suggests that AP bursts contain a distinct neural code. Prefrontal bursting is both modulated by and predictive of learning within multiple behavioral paradigms (Laviolette et al., 2005; Burgos-Robles et al., 2007). At the synaptic level, bursts facilitate plasticity, producing dendritic Ca-regenerative activity and depolarization required for NMDA receptor activation (Kampa et al., 2007). In addition, high-frequency bursts increase synaptic transmission reliability, especially at synapses with low release probability that exhibit short-term facilitation (Lisman, 1997). Moreover, release

probability can vary based on postsynaptic target (Markram et al., 1998). If this variability exists within D3R-expressing pyramidal cell networks, then burst regulation may route information to specific postsynaptic networks in a dopamine-dependent manner.

D3Rs have long been considered a potential therapeutic target for the treatment of serious mental illness (Sokoloff and Le Foll, 2017), especially because currently prescribed antipsychotics have high D3R affinity (Joyce and Millan, 2005). Determining a specific role for D3R in mental illness has been hampered by our poor understanding of its cellular distribution and function in prefrontal circuits. Here, we demonstrated that D3Rs have a distinct role within mPFC. Although both D2Rs and D3Rs are generally thought to signal through Gi/o, AIS Ca was only modulated in D3R-expressing neurons, not in neighboring D2R-expressing neurons. Indeed, we showed recently that D3Rs regulate AIS $Ca_V3.2$ channels through a noncanonical, arrestin-dependent pathway, both in auditory brainstem neurons and in heterologous expression systems (Yang et al., 2016). Interestingly, arrestin-biased compounds have been shown recently to alleviate schizophrenia-like phenotypes in mouse models (Urs et al., 2016). As targeted therapies continue to be developed, future work will be critical to determine whether interactions with mPFC D3Rs contribute to antipsychotic efficacy.

Footnotes

This work was supported by the National Science Foundation (Graduate Research Fellowship 1144247 to R.L.C.) and the National Institutes of Health (Grants DC011080, DA035913, and MH112729 to K.J.B. and Grant MH100292 to V.S.S.). TTA-

P2 was generously provided by Merck. We thank Howard Fields, Michael Roberts, Sidney Kuo, Gregory Hjelmstad, Patrick Sheets, and members of the Bender laboratory for discussions and comments on this work and Madeline Ferwerda, Jiggy Athilingam, and Caroline Keeshen for sharing their genotyping expertise.

The authors declare no competing financial interests.

Figures

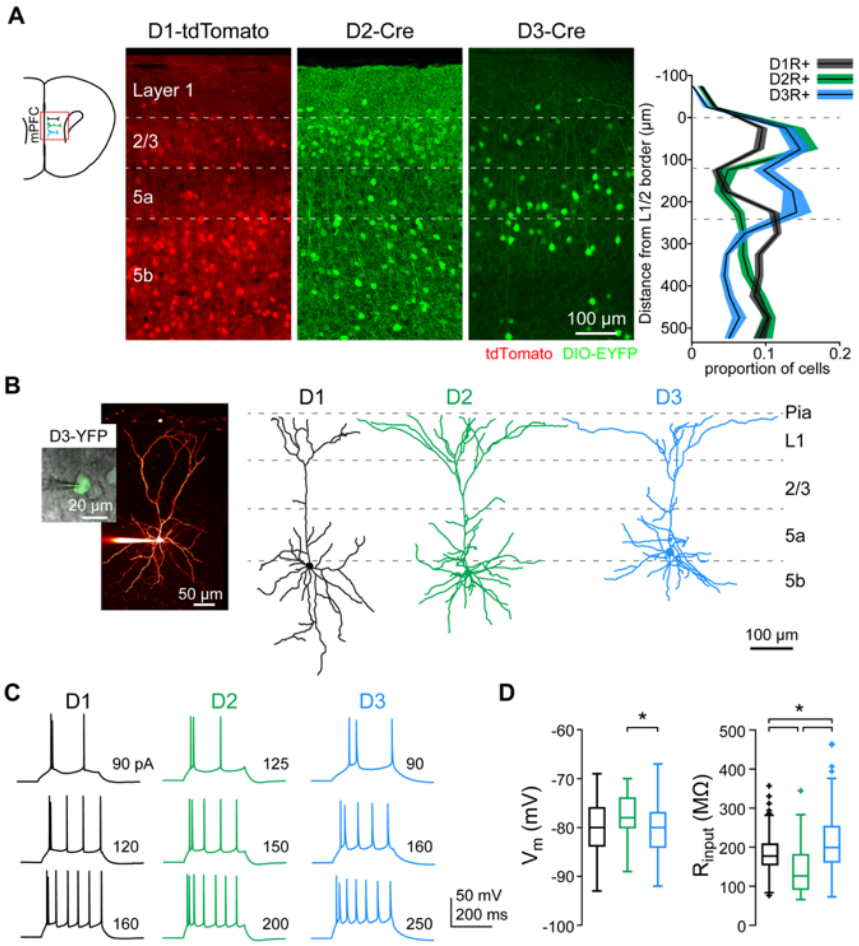

Figure 1. Laminar distribution, morphology, and intrinsic membrane properties of D1+, D2+, and D3+ L5 pyramidal cell classes in mPFC.

(A) Left, Schematic of coronal brain slice; red rectangle highlights mPFC recording region. Middle, Coronal mPFC sections showing fluorescently labeled (tdTomato or EYFP) D1R-, D2R-, or D3R-expressing neurons from either D1-tdTomato/D3-cre or D2-cre mice after AAV-DIO-EYFP injection. Laminar boundaries are designated with dashed white lines. Right, Distribution of D1+, D2+, and D3+ somatic distances from L1/2 border normalized to total fluorescently labeled cells within each mPFC section. Distributions for each cell type pooled from 3 D1-tdTmt/D3-cre animals and 3 D2-cre animals, 3 slices/animal. Solid line with shaded region indicates mean ± SEM.

(B) Left, 2PLSM z-projection of mPFC D3+ pyramidal cell fluorescently identified via EYFP injection (inset). Right, Dendritic arbor reconstructions of L5 subtypes (D1+: black, D2+: green, D3+: blue; color code throughout figure). Reconstructions are aligned to midline pia.

(C) Example AP firing patterns in response to somatic current injection for all three cell classes (one set per class, injection amplitude noted to right of traces, 300 ms duration).

(D) Resting V_m and R_{in} across cell classes. R_{in} was assessed with −50 pA steps from rest. *p < 0.05, Kruskal–Wallis, Wilcoxon rank-sum (Holm–Sidak correction); n = 95/35/188, D1+/D2+/D3+. Boxplots are median, 25th (Q1), and 75th (Q3) percentiles; whiskers extend to all data points that are not outliers. Outliers are defined as Q3 + 1.5*(Q3–Q1) and Q1–1.5*(Q3–Q1).

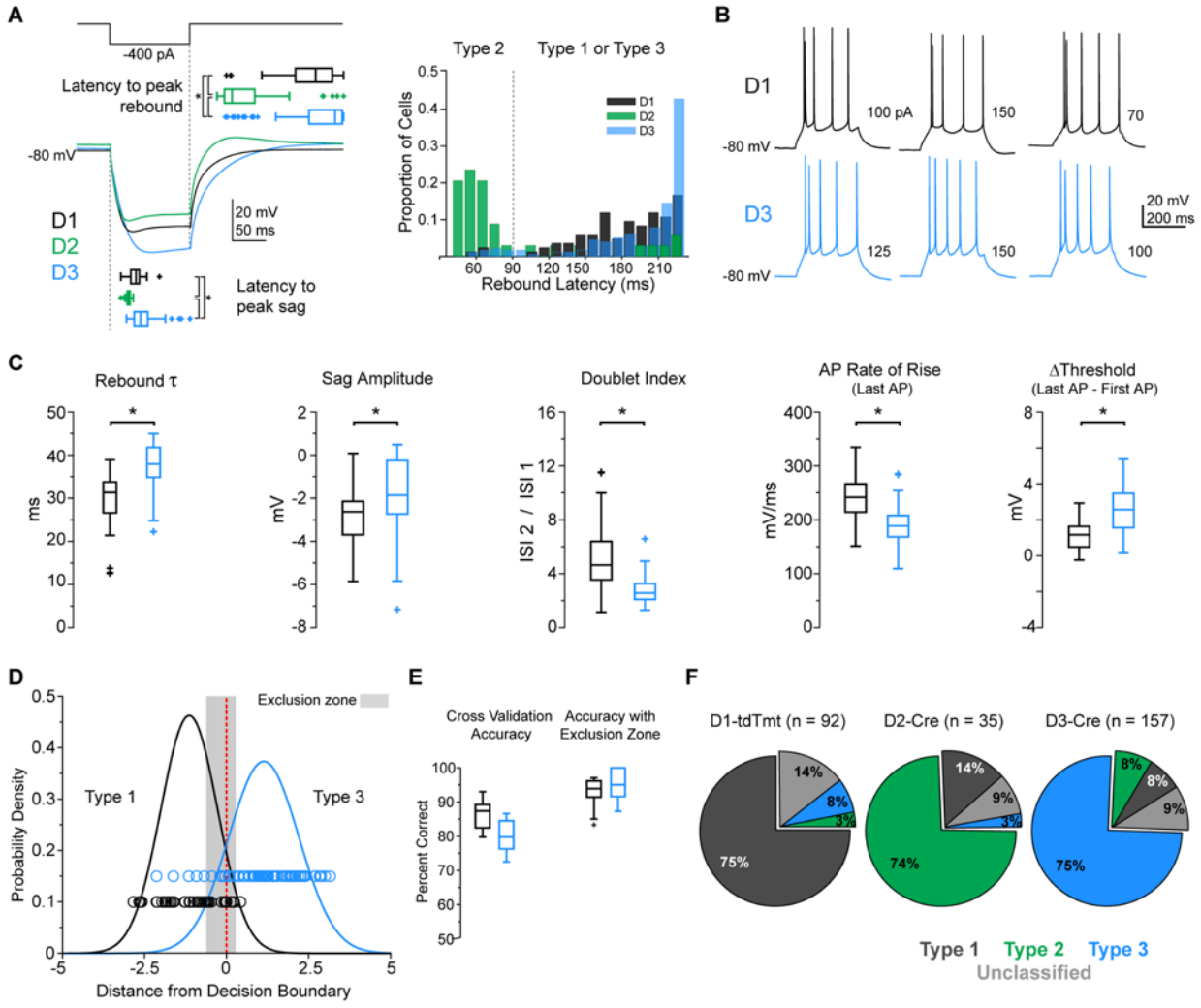

Figure 2. Electrophysiological classification of D1+, D2+, and D3+ pyramidal cell classes.

(A) Left, Responses to −400 pA hyperpolarizing steps differ between cell classes (D1+: black, D2+: green, D3+: blue; color code same in B–E). Boxplots quantify latency to peak rebound (maximum voltage relative to baseline after current offset) and latency to peak voltage sag (maximum voltage relative to steady-state after current onset). *p < 0.05, Kruskal–Wallis, Wilcoxon rank-sum, Holm–Sidak correction; rebound: n = 85/35/185, D1+/D2+/D3+; sag: n = 95/35/188, D1+/D2+/D3+. Right, Histogram of rebound latency by cell type. Dotted line represents cutoff between Type 2 and Type 1/Type 3 neurons.

(B) Example responses to somatic current injection in D1+ and D3+ neurons (three per class, amplitudes noted to right of traces).

(C) Electrophysiological features used for linear discriminant classifiers, shown for classification of five AP spike trains with Fluo-5F-based internal solution. D1+ and D3+ cell classes differ between all five parameters, which include responses to both hyperpolarizing (sag and rebound) and depolarizing (spike train properties) somatic current injection. *p < 0.05, two-sample t test; n = 47/72, D1+/D3+.

(D) Visualization of linear discriminant classifier (as in C) with individual D1+ and D3+ cells (circles) plotted with respect to Euclidean distance from the discriminant decision boundary (red dashed line). These distances were fit by normal distributions, which defined the

"exclusion zone," the area near the discriminant where cell classes are imperfectly separated and therefore "unidentified" (see Materials and Methods).

(E) Left, Results of holdout cross-validation for all 12 discriminant classifiers in predicting D1R or D3R expression. Right, Percentage accuracy of final models with "unclassified" D1+ and D3+ cells removed due to the exclusion zone.

(F) Percentage of fluorescent cells in D1-tdTomato, D2-Cre, and D3-Cre lines classified as Type 1, Type 2, Type 3, or unidentified. (Type 1: dark gray, Type 2: green; Type 3: blue; unidentified: light gray).

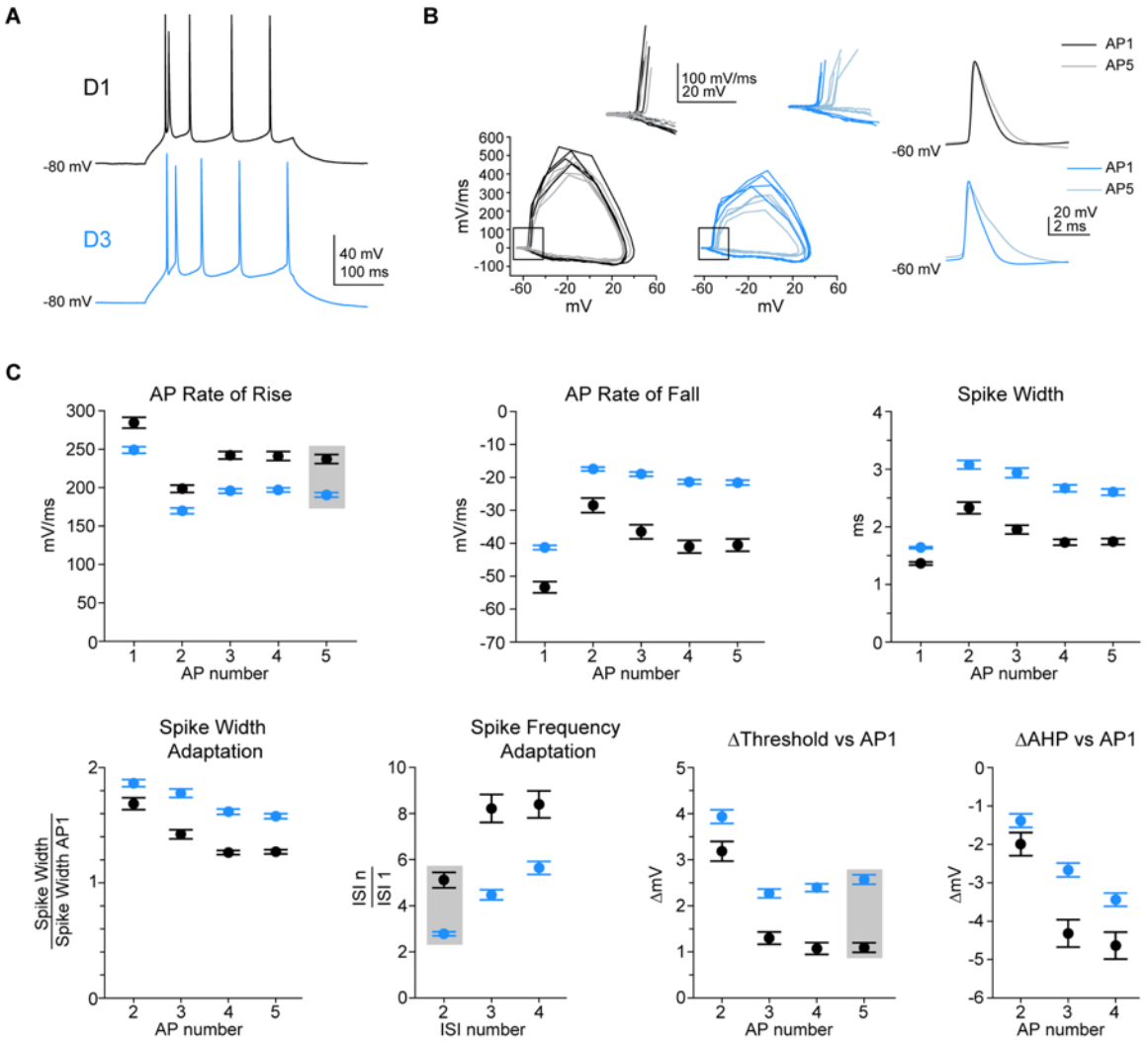

Figure 3. D1+ and D3+ mPFC pyramidal classes differ in AP waveform and AP spike train properties.

(A) Example spike trains from somatic current injection in D1+ (black) and D3+ (blue) neurons. Color code throughout figure. All analyses in this figure are for five AP spike trains from 300 ms current injections with Fluo-5F in the internal solution.

(B) Left, Phase plane plots demonstrate shifting AP threshold in D3+ cell class, but not in D1+ cell class (see insets). Right, Example changes in AP waveform across a five AP spike train for D1+ and D3+ cell classes.

(C) AP waveform and AP spike train properties differ between D1+ and D3+ cell classes. Gray boxes indicate parameter chosen for discriminant analysis; n = 47/72, D1+/D3+. Error bars indicate mean ± SEM.

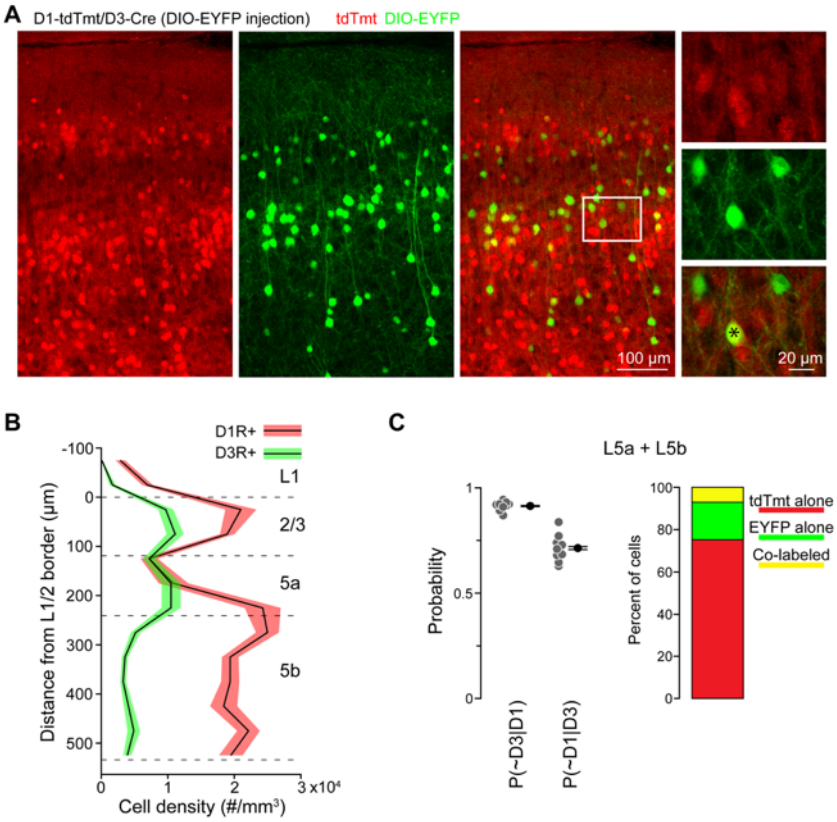

Figure 4. D1R and D3R expression in the mPFC occurs in largely separate cell populations.

(A) Confocal images of mPFC (maximal z-projection) from D1-tdTomato/D3-Cre mouse injected with AAV-DIO-EYFP. Right, Inset, Single optical section showing both single- and double-labeled cells. Asterisk denotes D1R and D3R colabeling.

(B) Distribution of D1+ and D3+ somatic distances from L1/2 border as a function of cell density (data same as plotted in Fig. 1A). Distributions for each cell type were pooled from three injections with three slices/animal. Solid line with shaded region indicates mean ± SEM.

(C) Left, Probability that a D1R- or D3R-expressing neuron lacks coexpression of the other receptor. Gray circles are single mPFC sections (three animals, three sections/animal), black circles are mean ± SEM. Right, tdTomato, EYFP, and colabeled cells as a percentage of all labeled cells within L5.

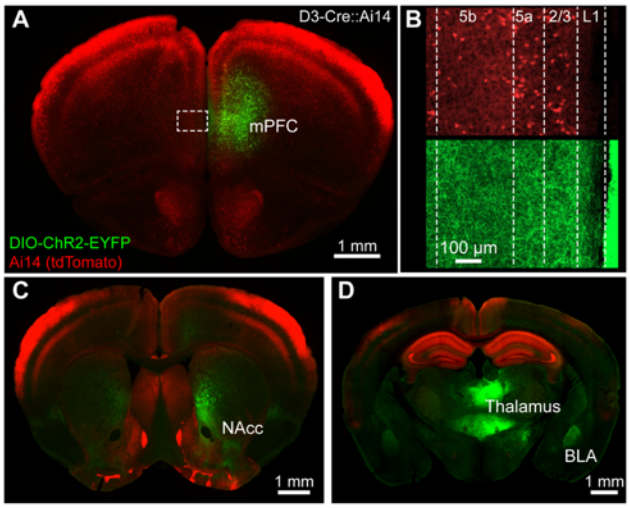

Figure 5. Prefrontal D3+ neuron projection patterns are revealed by orthograde tracing.
(A) Coronal section of D3-Cre::Ai14 mouse transfected with AAV-DIO-ChR2-EYFP in the right hemisphere (replicated in three animals). D3+ neurons throughout mPFC cortical laminae are labeled.
(B) Confocal images (area from inset in A) of mPFC D3+ neurons (top) and transfected axon fibers (bottom) contralateral to the injection site.
(C and D) Images taken from same animal as in A. Axons are prominent bilaterally within ventral striatum, including NAcc, BLA, and multiple thalamic nuclei.

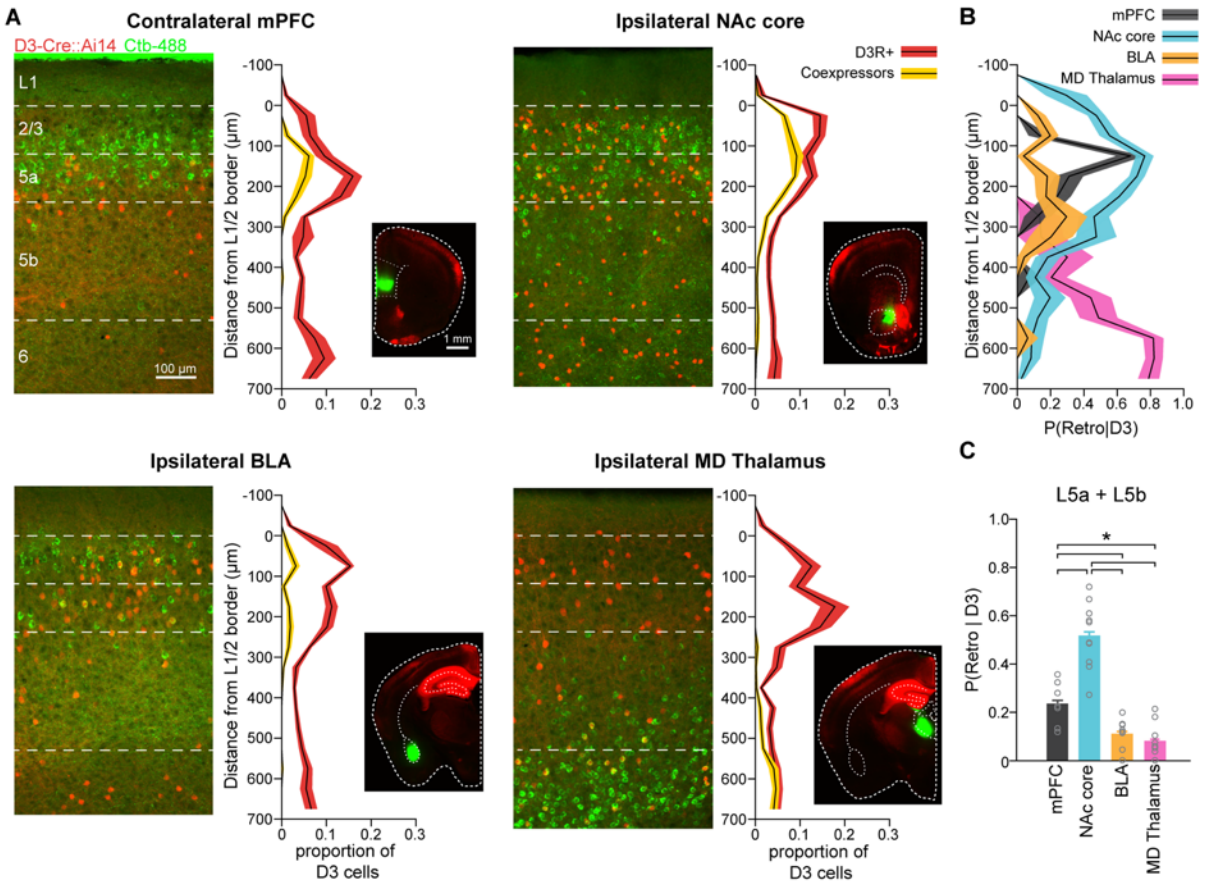

Figure 6. Retrograde tracing confirms IT targets of L5 D3+ mPFC neurons.

(A) D3-Cre::Ai14 adult mice were injected in four brain regions with retrograde tracer cholera toxin conjugated to green fluorophore Alexa Fluor 488. Left, Confocal images of mPFC showing D3R+ and retrogradely labeled cells. Right, Distribution of both D3R+ (red) and colabeled (yellow) somatic distances from L1/2 border normalized to maximum number of D3+ cells. Distributions are pooled from two to three injections per group, three to four slices/animal. Solid line with shaded region indicates mean ± SEM. Insets, Example images of injection targeting.

(B) Probability that a D3R+ cell projected to a particular brain region plotted as a function of distance from L1/2 border. Solid line with shaded region indicates mean ± SEM.

(C) Probability as in B, specifically within L5. Error bars indicate mean ± SEM. *$p < 0.05$, ANOVA, two-sample t test (Holm–Sidak correction); n = 7/10/8/9, mPFC/NAcc/BLA/MD.

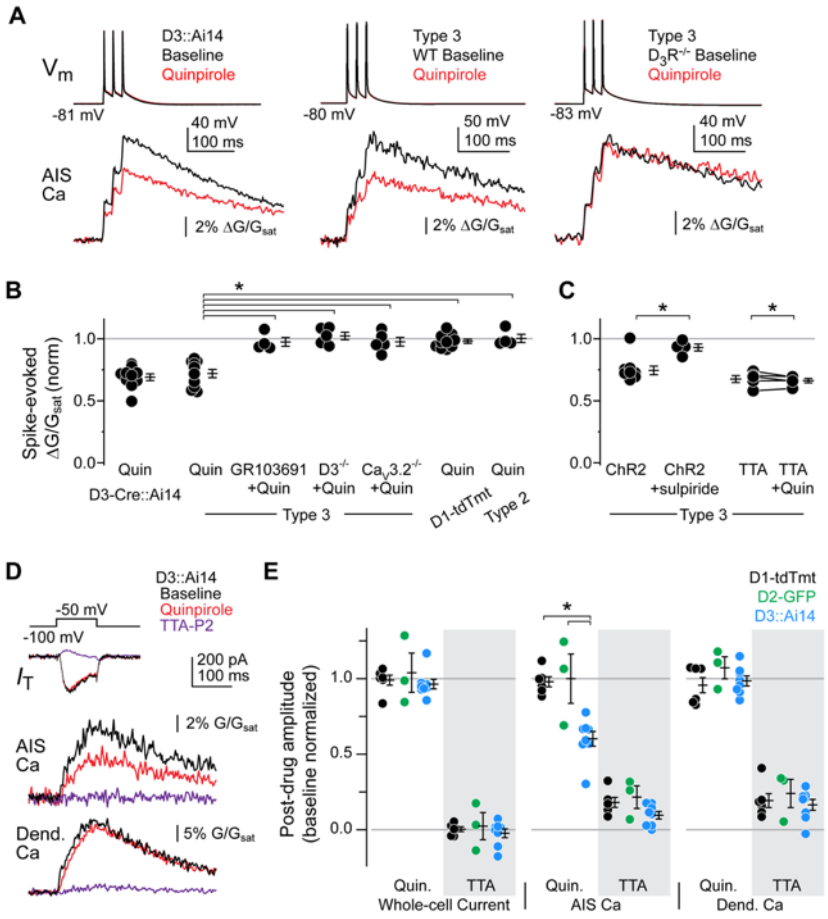

Figure 7. D3R modulation of AIS Ca is specific to a subclass of pyramidal cell.

(A) Spike-evoked (3 × 50 Hz) AIS Ca influx was imaged at identical time points before and after quinpirole in D3+ neurons from D3-Cre::Ai14 mice (left) and Type 3 neurons from wild-type (middle) or $D3R^{-/-}$ mice (right).

(B) AIS Ca transient amplitude normalized to baseline. GR103691 was present during baseline imaging. Circles are single cells. Error bars indicate mean ± SEM. *p < 0.05, ANOVA, two-sample t test (Holm–Sidak correction). Note: For clarity in the figure, we only indicate significant comparisons in relationship to quinpirole-treated Type 3 cells.

(C) Left, Optogenetic activation of endogenous catecholaminergic fibers in TH-Cre::Ai32 mice was sufficient to modulate AIS Ca. Effects were blocked by sulpiride. *p < 0.05, Wilcoxon's rank-sum test. Right, In TTA experiments, lines connect cells in which quinpirole was applied after the Ca_V3 channel antagonist TTA-P2. Data are normalized to pre-TTA conditions. *p = 0.44, Wilcoxon's signed-rank test. Circles are single cells. Error bars indicate mean ± SEM.

(D) Voltage step that activates Ca_V3 channels in a D3+ neuron evoked both AIS and dendritic Ca influx; quinpirole Ca modulation was specific to AIS. Ca influx in both locations and whole-cell current were suppressed by TTA-P2.

(E) Voltage-clamp experiments performed in fluorescently identified D1+, D2+, and D3+ mPFC neurons, using a voltage step to activate T-type channels as in D. Whole-cell current and AIS or dendrite Ca influx after quinpirole and then TTA-P2 application are plotted normalized to baseline. Circles are single cells. Error bars indicate mean ± SEM. *p < 0.05, ANOVA, two-sample t test (Holm–Sidak correction).

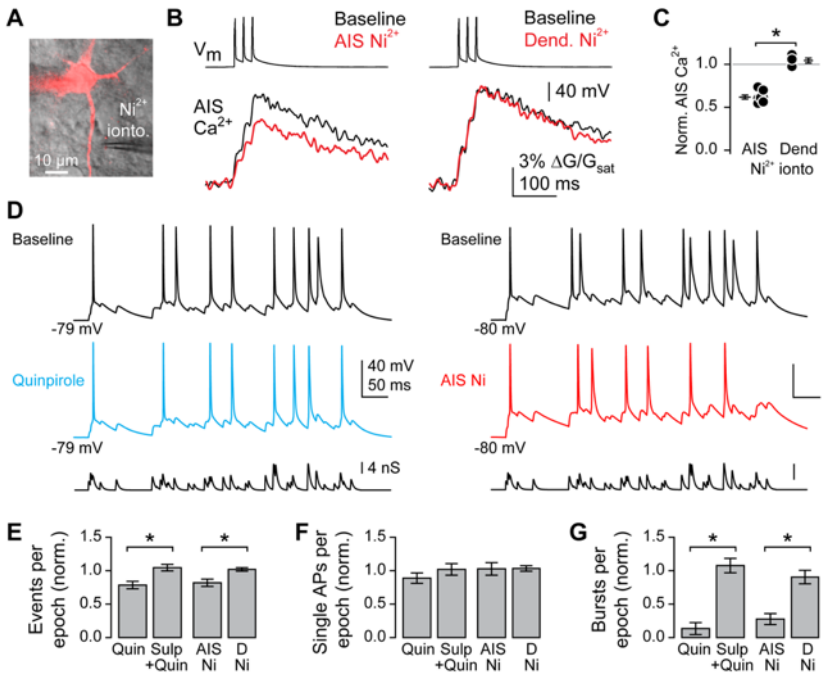

Figure 8. Modulation of AIS Ca suppresses burst initiation.

(A) Schematic of Ni iontophoresis location.

(B) AIS Ca influx was suppressed only when Ni was localized to the AIS. Traces are from a single experiment.

(C) AIS Ca transient amplitude normalized to interleaved controls after AIS- and dendrite-targeted Ni iontophoresis. *p < 0.05, Wilcoxon's rank-sum test.

(D) Spiking in response to a train of EPSG-like stimuli after bath quinpirole (left, cyan) or before and during AIS Ni (right, red) application.

(E–G) Spike events in baseline and drug-treated conditions normalized to baseline values in each experiment. Bursts (defined as spike frequencies >50 Hz) were reduced after AIS Ca modulation. Error bars indicate mean ± SEM. *p < 0.05, Wilcoxon's rank-sum test; n = 5/5/6/3, quinpirole, sulpiride + quinpirole, AIS Ni, AIS dendrite, respectively.

Tables

Ca Buffer	Number of APs	Sag Amplitude	Rebound Time Constant	Doublet Index	AP Rate of Rise	Threshold Change	Intercept
EGTA	3	0.552	0.381	-0.089	-1.826	0.036	-0.043
	4	0.000	0.329	-0.653	-1.664	0.943	-0.082
	5	0.211	0.279	-0.844	-1.285	1.058	-0.117
	6	-0.111	0.578	-1.009	-1.750	0.612	-0.194
	7	0.369	0.192	-0.998	-1.785	1.479	-0.589
	8	0.537	0.345	-0.883	-1.162	1.736	-1.029
Fluo5	3	0.339	1.408	-0.622	-1.030	0.317	0.469
	4	0.144	1.304	-1.147	-0.271	0.818	0.533
	5	0.181	1.272	-1.282	-1.058	0.949	0.550
	6	0.037	1.292	-1.152	-1.300	1.038	0.543
	7	-0.095	0.981	-1.370	-0.589	0.961	-0.179
	8	0.216	0.435	-0.753	-1.015	0.783	-0.752

Table 1. Coefficients for LDA
Standardized linear coefficients for all variables used for all linear discriminant classifiers (3-8 APs with either EGTA or Fluo5 in the internal solution).

Ca Buffer	Number of APs	Sag Amplitude (mV)	Rebound Time Constant (ms)	Doublet Index (ISI 2 / ISI 1)	AP Rate of Rise (V/s)	Threshold Change (ΔmV)	No. of Cells (D1; D3)
EGTA	3	-2.38 ± 0.94	32.53 ± 4.55	1.83 ± 0.80	229.23 ± 46.01	1.16 ± 1.29	34; 32
	4	-2.47 ± 0.98	32.30 ± 4.47	1.57 ± 0.62	234.56 ± 51.99	1.30 ± 1.18	36; 33
	5	-2.42 ± 0.96	32.56 ± 4.37	1.33 ± 0.45	220.07 ± 47.18	1.96 ± 1.37	35; 31
	6	-2.51 ± 0.94	32.21 ± 4.20	1.16 ± 0.35	216.11 ± 46.95	2.42 ± 1.79	35; 29
	7	-2.54 ± 0.95	31.79 ± 4.48	1.03 ± 0.30	213.77 ± 38.19	2.83 ± 1.49	36; 23
	8	-2.65 ± 0.88	31.47 ± 3.63	0.96 ± 0.25	211.66 ± 35.28	3.31 ± 1.61	34; 14
Fluo5	3	-2.12 ± 1.48	34.87 ± 6.52	1.68 ± 0.83	226.52 ± 49.14	0.83 ± 1.28	47; 85
	4	-2.13 ± 1.55	35.37 ± 6.17	1.38 ± 0.66	217.77 ± 46.87	1.38 ± 1.06	45; 78
	5	-2.21 ± 1.50	34.58 ± 6.82	1.18 ± 0.50	208.95 ± 42.70	1.99 ± 1.24	47; 72
	6	-2.29 ± 1.38	34.97 ± 6.20	1.04 ± 0.37	200.73 ± 44.81	2.62 ± 1.47	44; 65
	7	-2.39 ± 1.50	32.97 ± 6.46	0.99 ± 0.31	205.25 ± 40.55	2.93 ± 1.44	44; 37
	8	-2.55 ± 1.39	31.51 ± 4.63	1.00 ± 0.24	196.18 ± 40.14	3.32 ± 1.50	40; 15

Table 2. Mean ± SD

Mean and SD used to standardize data for classifiers (standardized data used for standardized linear coefficients).

Morphological Property		D1 (n = 11)	D2 (n = 10)	D3 (n = 29)	Type 3 (T3) (n = 33)	Significant Comparisons (p < .05)
Tuft Width (μm)		195.46 ± 17.93	345.94 ± 30.74	287.67 ± 19.81	280.48 ± 14.60	D2, D3, T3 > D1
Dendritic Length (mm)	Apical	1.66 ± 0.20	2.82 ± 0.36	1.67 ± 0.11	1.70 ± 0.12	D2 > D1, D3, T3
	Basal	1.41 ± 0.20	2.14 ± 0.12	2.16 ± 0.13	1.56 ± 0.09	D2, D3 > D1, T3
Branch Points (#)	Apical	10.27 ± 1.30	18.50 ± 2.28	10.14 ± 0.77	9.79 ± 0.88	D2 > D1, D3, T3
	Basal	5.45 ± 0.86	13.40 ± 1.39	12.48 ± 0.71	8.48 ± 0.53	D2, D3 > T3 > D1
Apical Obliques (#)		4.45 ± 0.67	7.10 ± 1.09	2.31 ± 0.27	2.21 ± 0.25	D1, D2 > D3, T3
Pia to soma (μm)		359.45 ± 9.85	405.53 ± 11.69	306.24 ± 6.24	302.16 ± 7.75	D2 > D1 > D3, T3

Table 3. Morphology of pyramidal cell classes
Morphological parameters of D1+, D2+, D3+, and Type 3 (T3) pyramidal neuron subclasses. Parameters are as follows: Tuft width (μm) was determined as the diameter of a circle parallel to pia that encompasses all L1 tuft dendrites. Dendritic length was the overall length of dendritic apical and basal structures. “Apical” includes the primary apical dendrite, all apical obliques, and apical tuft. Total number of branch points was calculated using the same apical and basal designations as dendritic length. Apical oblique number is the number of oblique dendrites emerging from the primary apical dendrite before tuft formation. Pia to soma is the distance from pia/L1 border to center of soma. Values are mean ± SEM. Significant comparisons ($p < 0.05$) determined by ANOVA followed by two-sample t-tests with Holm-Sidak correction.

References

Apostolides PF, Milstein AD, Grienberger C, Bittner KC, Magee JC (2016) Axonal filtering allows reliable output during dendritic plateau-driven complex spiking in CA1 neurons. Neuron 89:770–783.

Avesar D, Gulledge AT (2012) Selective serotonergic excitation of callosal projection neurons. Front Neural Circuits 6:1–11.

Bender KJ, Ford CP, Trussell LO (2010) Dopaminergic modulation of axon initial segment calcium channels regulates action potential initiation. Neuron 68:500–511.

Bender KJ, Trussell LO (2009) Axon initial segment Ca2+ channels influence action potential generation and timing. Neuron 61:259–271.

Bender KJ, Uebele VN, Renger JJ, Trussell LO (2012) Control of firing patterns through modulation of axon initial segment T-type calcium channels. J Physiol 590:109–118.

Bergson C, Mrzljak L, Smiley JF, Pappy M, Levenson R, Goldman-Rakic PS (1995) Regional, cellular, and subcellular variations in the distribution of D1 and D5 dopamine receptors in primate brain. J Neurosci 15:7821–7836.

Bertran-Gonzalez J, Bosch C, Maroteaux M, Matamales M, Herve D, Valjent E, Girault JA (2008) Opposing patterns of signaling activation in dopamine D1 and D2 receptor-expressing striatal neurons in response to cocaine and haloperidol. J Neurosci 28:5671–5685.

Boudewijns ZSRM, Groen MR, Lodder B, McMaster MTB, Kalogreades L, de Haan R, Narayanan RT, Meredith RM, Mansvelder HD, de Kock CPJ (2013) Layer-specific high-frequency action potential spiking in the prefrontal cortex of awake rats. Front Cell Neurosci 7:99.

Bouthenet M-L, Souil E, Martres M-P, Sokoloff P, Giros B, Schwartz J-C (1991) Localization of dopamine D3 receptor mRNA in the rat brain using in situ hybridization histochemistry: comparison with dopamine D2 receptor mRNA. Brain Res 564:203–219.

Burgos-Robles A, Vidal-Gonzalez I, Santini E, Quirk GJ (2007) Consolidation of Fear Extinction Requires NMDA Receptor-Dependent Bursting in the Ventromedial Prefrontal Cortex. Neuron 53:871–880.

Cain SM, Snutch TP (2010) Contributions of T-type calcium channel isoforms to neuronal firing. Channels (Austin) 4:475–482.

Callewaert G, Eilers J, Konnerth A (1996) Axonal calcium entry during fast “sodium” action potentials in rat cerebellar Purkinje neurones. J Physiol 495:641–647.

Dembrow N, Johnston D (2014) Subcircuit-specific neuromodulation in the prefrontal cortex. Front Neural Circuits 8:1–9.

Dembrow NC, Chitwood RA, Johnston D (2010) Projection-specific neuromodulation of medial prefrontal cortex neurons. J Neurosci 30:16922–16937.

DeNardo LA, Berns DS, DeLoach K, Luo L (2015) Connectivity of mouse somatosensory and prefrontal cortex examined with trans-synaptic tracing. Nat Neurosci 18:1687–1697.

François A, Schüetter N, Laffray S, Sanguesa J, Pizzoccaro A, Dubel S, Mantilleri A, Nargeot J, Noël J, Wood J, Moqrich A, Pongs O, Bourinet E (2015) The Low-Threshold Calcium Channel Cav3.2 Determines Low-Threshold Mechanoreceptor Function. Cell Rep 10:370–382.

Gee S, Ellwood I, Patel T, Luongo F, Deisseroth K, Sohal VS (2012) Synaptic activity unmasks dopamine D2 receptor modulation of a specific class of layer V pyramidal neurons in prefrontal cortex. J Neurosci 32:4959–4971.

Gerfen CR, Surmeier DJ (2011) Modulation of striatal projection systems by dopamine. Annu Rev Neurosci 34:441–466.

Glickstein SB, Desteno DA, Hof PR, Schmauss C (2005) Mice lacking dopamine D2 and D3 receptors exhibit differential activation of prefrontal cortical neurons during tasks requiring attention. Cereb Cortex 15:1016–1024.

Glickstein SB, Hof PR, Schmauss C (2002) Mice lacking dopamine D2 and D3 receptors have spatial working memory deficits. J Neurosci 22:5619–29.

Gong S, Zheng C, Doughty ML, Losos K, Didkovsky N, Schambra UB, Nowak NJ, Joyner A, Leblanc G, Hatten ME, Heintz N (2003) A gene expression atlas of the central nervous system based on bacterial artificial chromosomes. Nature 425:917–925.

Gross G, Wicke K, Drescher KU (2013) Dopamine D_3 receptor antagonism--still a therapeutic option for the treatment of schizophrenia. Naunyn Schmiedebergs Arch Pharmacol 386:155–166.

Gründemann J, Clark BA (2015) Calcium-Activated Potassium Channels at Nodes of Ranvier Secure Axonal Spike Propagation. Cell Rep 12:1715–1722.

Hooks BM, Hires SA, Zhang Y-X, Huber D, Petreanu L, Svoboda K, Shepherd GMG (2011) Laminar analysis of excitatory local circuits in vibrissal motor and sensory cortical areas. PLoS Biol 9:e1000572.

Joyce JN, Millan MJ (2005) Dopamine D3 receptor antagonists as therapeutic agents. Drug Discov Today 10:917–925.

Kampa BM, Letzkus JJ, Stuart GJ (2007) Dendritic mechanisms controlling spike-timing-dependent synaptic plasticity. Trends Neurosci 30:456–463.

Kole M (2011) First node of ranvier facilitates high-frequency burst encoding. Neuron 71:671–682.

Land BB, Narayanan NS, Liu RJ, Gianessi CA, Brayton CE, Grimaldi DM, Sarhan M, Guarnieri DJ, Deisseroth K, Aghajanian GK, DiLeone RJ (2014) Medial prefrontal D1 dopamine neurons control food intake. Nat Neurosci 17:248–253.

Laruelle M (2014) Schizophrenia: From dopaminergic to glutamatergic interventions. Curr Opin Pharmacol 14:97–102.

Laviolette SR (2005) A Subpopulation of Neurons in the Medial Prefrontal Cortex Encodes Emotional Learning with Burst and Frequency Codes through a Dopamine D4 Receptor-Dependent Basolateral Amygdala Input. J Neurosci 25:6066–6075.

Lévesque D, Diaz J, Pilon C, Martres MP, Giros B, Souil E, Schott D, Morgat JL, Schwartz JC, Sokoloff P (1992) Identification, characterization, and localization of the dopamine D3 receptor in rat brain using 7-[3H]hydroxy-N,N-di-n-propyl-2-aminotetralin. Proc Natl Acad Sci U S A 89:8155–8159.

Lidow MS, Wang F, Cao Y, Goldman-Rakic PS (1998) Layer V neurons bear the majority of mRNAs encoding the five distinct dopamine receptor subtypes in the primate prefrontal cortex. Synapse 28:10–20.

Lisman JE (1997) Bursts as a unit of neural information: making unreliable synapses reliable. Trends Neurosci 20:38–43.

Lüscher C, Lipp P, Lüscher HR, Niggli E (1996) Control of action potential propagation by intracellular Ca2+ in cultured rat dorsal root ganglion cells. J Physiol 490 (Pt 2):319–324.

Markram H, Wang Y, Tsodyks M (1998) Differential signaling via the same axon of neocortical pyramidal neurons. Proc Natl Acad Sci U S A 95:5323–8.

Martinello K, Huang Z, Lujan R, Tran B, Watanabe M, Cooper EC, Brown DA, Shah MM (2015) Cholinergic afferent stimulation induces axonal function plasticity in adult hippocampal granule cells. Neuron 85:346–363.

McCormick DA, Prince DA (1987) Post-natal development of electrophysiological properties of rat cerebral cortical pyramidal neurones. J Physiol 393:743–762.

McCormick DA, Shu Y, Yu Y (2007) Neurophysiology: Hodgkin and Huxley model - still standing? Nature 445:E1–E2.

Millan MJ, Buccafusco JJ, Loiseau F, Watson DJG, Decamp E, Fone KCF, Thomasson-Perret N, Hill M, Mocaer E, Schneider JS (2010) The dopamine D(3) receptor antagonist, S33138, counters cognitive impairment in a range of rodent and primate procedures. Int J Neuropsychopharmacol 13:1035–1051.

Minzer K, Lee O, Hong JJ, Singer HS (2004) Increased prefrontal D2 protein in Tourette syndrome: A postmortem analysis of frontal cortex and striatum. J Neurol Sci 219:55–61.

Molnár Z, Cheung AFP (2006) Towards the classification of subpopulations of layer V pyramidal projection neurons. Neurosci Res 55:105–115.

Morishima M, Kawaguchi Y (2006) Recurrent connection patterns of corticostriatal pyramidal cells in frontal cortex. J Neurosci 26:4394–4405.

Nakajima S, Gerretsen P, Takeuchi H, Caravaggio F, Chow T, Le Foll B, Mulsant B, Pollock B, Graff-Guerrero A (2013) The potential role of dopamine D3 receptor neurotransmission in cognition. Eur Neuropsychopharmacol 23:799–813.

Noaín D, Avale ME, Wedemeyer C, Calvo D, Peper M, Rubinstein M (2006) Identification of brain neurons expressing the dopamine D4 receptor gene using BAC transgenic mice. Eur J Neurosci 24:2429–2438.

Otsuka T, Kawaguchi Y (2011) Cell diversity and connection specificity between callosal projection neurons in the frontal cortex. J Neurosci 31:3862–3870.

Schiller J, Helmchen F, Sakmann B (1995) Spatial profile of dendritic calcium transients evoked by action potentials in rat neocortical pyramidal neurones. J Physiol 487:583–600.

Seong HJ, Carter AG (2012) D1 receptor modulation of action potential firing in a subpopulation of layer 5 pyramidal neurons in the prefrontal cortex. J Neurosci 32:10516–10521.

Shepherd GMG (2013) Corticostriatal connectivity and its role in disease. Nat Rev Neurosci 14:278–291.

Sokoloff P, Le Foll B (2016) The dopamine D3 receptor, a quarter century later Herman J, ed. Eur J Neurosci:1–18.

Urs NM, Gee SM, Pack TF, McCorvy JD, Evron T, Snyder JC, Yang X, Rodriguiz RM, Borrelli E, Wetsel WC, Jin J, Roth BL, O'Donnell P, Caron MG (2016) Distinct cortical and striatal actions of a β-arrestin-biased dopamine D2 receptor ligand reveal unique antipsychotic-like properties. Proc Natl Acad Sci U S A 113:201614347.

van Aerde KI, Qi G, Feldmeyer D (2015) Cell type-specific effects of adenosine on cortical neurons. Cereb Cortex 25:772–787.

Williams SR, Stuart GJ (1999) Mechanisms and consequences of action potential burst firing in rat neocortical pyramidal neurons. J Physiol 521:467–482.

Yang S, Ben-Shalom R, Ahn M, Liptak AT, van Rijn RM, Whistler JL, Bender KJ (2016) β-Arrestin-Dependent Dopaminergic Regulation of Calcium Channel Activity in the Axon Initial Segment. Cell Rep 16:1518–1526.

Yu Y, Maureira C, Liu X, McCormick D (2010) P/Q and N channels control baseline and spike-triggered calcium levels in neocortical axons and synaptic boutons. J Neurosci 30:11858–11869.

Zhang Z (2004) Maturation of layer V pyramidal neurons in the rat prefrontal cortex: intrinsic properties and synaptic function. J Neurophysiol 91:1171–1182.

Chapter 3

Further characterization of transgenic mouse lines expressing D1, D2, and D3 receptors

Introduction

D1-tdtomato, D1-Cre, D2-Cre, and D3-Cre transgenic mouse lines are critical tools for the study of dopamine receptor expressing neurons, allowing the visualization and/or manipulation of genetically-identified cells both *in vivo* and *in vitro* (Gee et al., 2012; Seong and Carter, 2012; Land et al., 2014; Clarkson et al., 2017). In this study, I further characterize these transgenic mouse lines, with a particular focus on the D3-Cre line, as the work from Chapter 2 (Clarkson et al., 2017) is, to my knowledge, the first published study using this animal. Our lab recovered the D3-Cre mouse line from cryopreservation, subsequently crossing it to an Ai14 line for fluorescent identification of D3R-expressing cells.

In the previous chapter, by using this D3-Cre mouse line, we identified a novel cell class within layer 5 (L5) of medial prefrontal cortex (mPFC); this cell class is intratelencephalic (IT), projecting to the contralateral cortex and expressing the dopamine D3 receptor (D3R). Here, I examine D3R-expressing pyramidal neuron projections in more detail, as well as the distribution of D3R-expressing cells throughout the brain. In addition, I further characterize the mouse lines utilized in Chapter 2, which we relied upon for our comparative analyses of D1R-, D2R, and D3R-expressing (D1+, D2+, D3+) neurons.

Materials and Methods

In Chapter 3, I further analyze experiments reported in Chapter 2. Therefore, methods are exactly as described in Chapter 2, Materials and Methods: “Laminar distribution and orthograde/retrograde tracing,” except for the additional use of D1-Cre mice (EY262, www.gensat.org) for laminar distribution comparison with the D1-tdTomato line.

In brief, for laminar expression analyses, P28-P35 D1-tdTomato/D3-cre, D1-cre, or D2-cre mice were injected bilaterally with large volumes of either AAV-EF1α-DIO-EYFP or AAV-EF1α-DIO-mCherry in the mPFC. Four to 5 weeks after injection, animals were perfused. After full brain fixation (4 h), 50 μm coronal sections of the mPFC were made in PBS using a vibratome.

For orthograde tracing, P28 D3-Cre::Ai14 mice were unilaterally injected with 300 nl AAV-EF1α-DIO-ChR2-EYFP in the mPFC. After three weeks, animals were perfused and the full brain fixed overnight; 50-μm-thick coronal sections of the entire brain were then obtained to assess axonal projection patterns. For retrograde tracing experiments, P52+ D3-Cre::Ai14 mice were stereotaxically-injected with 200-300 nl of Alexa Fluor 488 conjugated to cholera toxin subunit B (Ctb-488) in mPFC, basolateral amygdala (BLA), nucleus accumbens core (NAcc), and mediodorsal (MD) thalamus. 3-4 d after injection, animals were perfused and 50 μm-thick coronal mPFC sections were obtained for laminar and colocalization analyses, with 75 μm sections taken for injection site confirmation. For retrograde tracing, all injections except mPFC were ipsilateral to prefrontal analysis region. Laminar depths were used as previously determined by L3

and L5b markers Cux1 and Ctip2 (DeNardo et al., 2015), with boundaries defined with respect to the L1/2 border given variability in L1 thickness.

Results

Further characterization of D3+ axonal projections

In Chapter 2, we injected 3 D3-Cre::Ai14 mice with DIO-ChR2-EYFP in the mPFC, assessing projection patterns of D3+ mPFC cells across the brain via orthograde tracing (Fig. 5). Here, I further examined one of these animals, including the mPFC injection site and resultant labeled axon fibers throughout the brain. EYFP+ cells could be seen across multiple mPFC subregions: medial orbital (MO), infralimbic (IL), and prelimbic (PL). In addition, as shown previously, the injection site included all cortical laminae (Fig. 5, 9).

D3+ cells projected to contra- and ipsilateral cortex, both within and outside the mPFC. These cortical areas included all the injected mPFC subregions (MO, IL, PL), as well as the lateral orbital cortex (LO) and agranular insular cortex (AI) (Fig. 10). In addition to the cerebral cortex, D3+ fibers were labeled bilaterally in the anterior olfactory nucleus (AON), claustrum (CLA), lateral septum (LS), and olfactory tubercle (OT) (Fig. 10; Fig. 11, A1).

Both the dorsal and ventral striatum were densely labeled, including the caudate putamen (CPu), NAcc, and nucleus accumbens shell (NAcs) (Fig. 10, 11). Projections to all striatal regions were bilateral, with fiber density highest ipsilaterally, a pattern seen often across the brain (Fig. 11, A1-2, B1). For example, midline thalamic nuclei (Fig. 11, B2, C1-2) and multiple amygdalar nuclei (Fig. 11, C1-2) had a similar bilateral projection

pattern. In the amygdala, the BLA projection was most prominent, but sparse fibers were seen in the basomedial and central nuclei (BMA, CeA) (Fig. 11, C1-2). Finally, D3+ mPFC cells projected bilaterally to the midbrain, though with lower fiber density than to the telencephalon or diencephalon. Brainstem projections included the hypothalamus (Hyp), periaqueductal gray (PAG), mesencephalic reticular formation (MRF), and interpeduncular nucleus (IP) (Fig. 11, C2, D1-2).

D3R-expressing cells are distributed throughout the brain

We previously utilized D3-Cre transgenic mice (founder line KJ302), which we recovered from the GENSAT cryo-archive. Here, I examined the pattern of D3R-expressing cells throughout the brain, from the frontal lobes and olfactory bulb (OB) to the midbrain. D3R-expressing cells were distributed throughout the brain (Fig. 12).

In addition to the mPFC, D3R-expressing cells were found in numerous other cortical regions, including primary somatosensory cortex (Fig. 14i), primary visual cortex, (Fig. 16i), retrosplenial cortex (Fig. 16ii), and secondary motor cortex (Fig. 13ii). Interestingly, many cortical regions had stark laminar boundaries in D3R expression. For example, in primary somatosensory cortex, D3R-expressing cells were densely contained in L23 but were absent in L4 (Fig. 14i).

D3+ cells were found throughout both dorsal and ventral striatum, but cell density was much higher in the ventral striatum, including the nucleus accumbens and OT. Within the OT, densest expression was found in the Islands of Calleja (Fig. 14iii). In addition to the ventral striatum, other limbic regions had high D3R expression, such as the hippocampus and the amygdala (e.g. BLA, CeA) (Fig. 15).

Prefrontal L5 D3R expression is not developmentally regulated

To visualize D3+ neurons for electrophysiological and pharmacological analyses, we crossed a D3-Cre mouse line with the Ai14 Cre reporter mouse line. In the resulting D3-Cre::Ai14 line, Cre recombinase was expressed under the control of the Drd3 gene, resulting in Cre-dependent tdTomato expression. With this experimental design, tdTomato expression could result from transient developmental D3R expression. However, D3R expression did not appear to be downregulated after early postnatal development, in contrast to observations in sensory cortex (Gurevich and Joyce, 2000), as there was strong overlap between Ai14 reporter tdTomato expression and EYFP expression mediated by viral transfection at P28 (Fig. 17).

D3R-expressing neurons are a small percentage of prefrontal IT output

As described in Chapter 2, we previously injected Ctb-488 into the contralateral mPFC or ipsilateral NAcc, mPFC, or BLA, and examined the distribution of retrogradely-labeled mPFC cells (Fig. 18). As expected from orthograde tracing (Fig. 5), we observed retrogradely-labeled cells in mPFC following all injections, though with distinct distributions and cell densities (Figs. 6, 18, 19). We found that L5 D3+ cells predominantly projected to contralateral mPFC or ipsilateral NAcc (~25%, ~52%), and therefore are an IT pyramidal subtype.

Here, I additionally determined the probability that a L5 mPFC projection neuron also expresses the D3R. In other words, what percentage are D3+ cells of total prefrontal output to these regions? L5 D3+ cells comprised ~10% of prefrontal cells

projecting to IT regions (BLA, mPFC, NAcc), whereas <3% of L5 MD thalamus projecting neurons expressed D3R (Fig. 20C). Therefore, while many D3+ cells project to IT regions, D3+ cells are a relatively small percentage of total prefrontal IT output. Indeed, D3+ cells had a much lower mPFC density as compared to D1+ and D2+ cells, except in L5a, where they had a similar density (Fig. 22; see Figs. 9, 21, 23A,B for representative mPFC widefield images).

D1-Cre and D1-tdtomato mice have similar D1+ mPFC expression patterns

In Chapter 2, we characterized the electrophysiology, morphology, and laminar expression of D1+ neurons using the D1-tdtomato BAC transgenic line. Here, I compare D1tmt+ (Fig. 23A) and D1cre+ (Fig. 23B) expression patterns, using either D1-tdTomato mice or D1-Cre mice injected with DIO-mCherry or DIO-EYFP bilaterally in the mPFC. The overall distribution pattern was the same, with peaks in L2/3 and at the L5a/5b border. However, the D1tmt+ cell population was smaller than the D1cre+ population, particularly in the superficial layers (Fig. 23C). This could potentially be explained by lower D1R mRNA expression in the superficial cortical laminae; in D1-tdTomato mice, lower mRNA expression would lead to fainter fluorescence, which could be indistinguishable from background fluorescence.

Discussion

Dopamine receptor transgenic mouse lines (D1-tdtomato, D1-Cre, D2-Cre, and D3-Cre) have been crucial tools for classifying mPFC pyramidal neuron subtypes, with numerous studies demonstrating that dopamine receptor expression in L5 correlates

with electrophysiological and morphological properties, as well as projection patterns (Gee et al., 2012; Seong and Carter, 2012; Land et al., 2014; Clarkson et al., 2017). In this study, I find that mPFC D1+, D2+, and D3+ cell populations are differentially distributed across prefrontal cortex, providing additional context for prior results. Following an in depth examination of D3+ projection patterns, I further validate the D3-Cre mouse line used for the first time in Chapter 2 (Clarkson et al., 2017); as described below, the D3+ cell population distribution in this line largely recapitulated D3R mRNA distribution.

D3R-expressing cells throughout the brain: comparison with prior reports

The distribution of D3+ cells in the D3-Cre::Ai14 mouse line was qualitatively very similar to prior in situ hybridization studies of D3R mRNA distribution in both human and rodent. In particular, D3+ cells were densely packed within limbic regions with very high D3R mRNA expression, including the nucleus accumbens, OT, islands of Calleja complex, and hippocampus. Furthermore, D3+ cells were much less abundant in the dorsal striatum, a region consistently reported to have low expression of D3R mRNA (Sokoloff et al., 1990; Bouthenet et al., 1991; Meador-Woodruff et al., 1996; Suzuki et al., 1998).

In this study, cortical expression density varied widely, though D3+ cells were observed throughout the neocortex, consistent with prior reports of low to moderate mRNA expression (Bouthenet et al., 1991; Suzuki et al., 1998). However, while L23 somatosensory cortex was densely packed with D3+ cells (Fig. 14i), this region has not been noted to have high D3R mRNA expression. Inconsistencies between mRNA and

Cre-dependent expression could arise from transient developmental D3R expression (Gurevich and Joyce, 2000). In addition, while cellular mRNA expression levels are graded, Cre-dependent expression is binary. Low single cell mRNA levels would nonetheless lead to Cre-dependent fluorescence, while high mRNA levels within a given brain region would not necessarily correlate with high cell numbers. Overall, however, D3+ cell fluorescence expression in the D3-Cre::Ai14 mouse line matches well with prior studies of D3R mRNA distribution, suggesting that D3R expression in the D3-Cre::Ai14 animals does not arise from transient developmental expression. I confirmed this in the mPFC via injection of DIO-ChR2-EYFP in P28 animals, showing a high colocalization of EYFP and Ai14 (tdTomato) within L5 mPFC (Fig. 17).

However, neither the presence of the gene encoding the D3R (Drd3) nor the level of D3R mRNA provides information about the amount of D3R mRNA translated to protein, D3R subcellular localization, or presence of active D3R protein and ligand binding sites. Therefore, complementary approaches have also been utilized, such as D3R-selective antibodies for detection of D3R protein or ligand-binding autoradiography to probe for the pharmacologically-active receptor (Hall et al., 1996; Diaz et al., 2000; Stanwood et al., 2000). With respect to D3R-expressing brain regions, these studies are in general agreement with both the D3-Cre::Ai14 and mRNA distribution results, though future studies will be needed to confirm and extend these findings as drugs with higher D3R selectivity over D2R become available (Burris, 1995).

D3+ prefrontal projections to cortical and subcortical targets

Prefrontal D3+ axon fibers were found bilaterally throughout the brain, with fiber density generally highest ipsilaterally. As described in Chapter 2, axons were prominent in the contralateral mPFC as well as bilateral BLA, ventral striatum, and midline thalamic nuclei (Fig. 5). In Chapter 3, I examined D3+ targets more extensively, noting additional ipsilateral cortical targets (Fig. 10, 11-A1, A2), as well as several additional subcortical targets, including the PAG and hypothalamus (Fig. 11-C1, D1, D2). Based on these results, D3+ mPFC neurons project to the vast majority of mPFC output regions, both cortical and subcortical (Vertes, 2004; Hoover and Vertes, 2011).

Regardless of target, D3+ mPFC neurons comprise a small percentage of prefrontal projection neurons, consistent with their overall low numbers. Future studies will be needed to explore the impact of these projections on prefrontal-dependent behaviors, perhaps through optogenetic or DREADD pharmacological manipulations of D3+ mPFC cell bodies or specific axonal projections. The behavioral impact of these manipulations will depend on many factors, including target cell-type specificity and synaptic strength and dynamics. In addition, local connectivity may play important role in regulating prefrontal output, via interactions with neighboring D1+ and D2+ projection neurons.

Figures

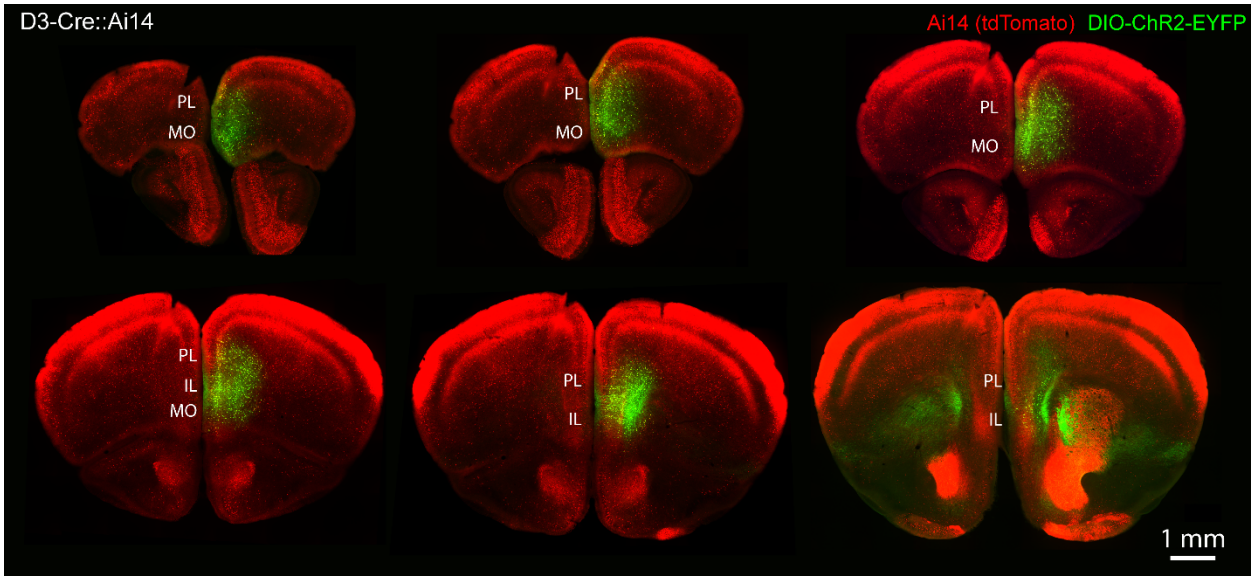

Figure 9. DIO-ChR2-EYFP injection site is restricted to mPFC.
Coronal sections of D3-Cre::Ai14 mouse injected with AAV-DIO-ChR2-EYFP in the right hemisphere. Note: Figs. 9-16 are all from the same D3-Cre::Ai14 mouse.

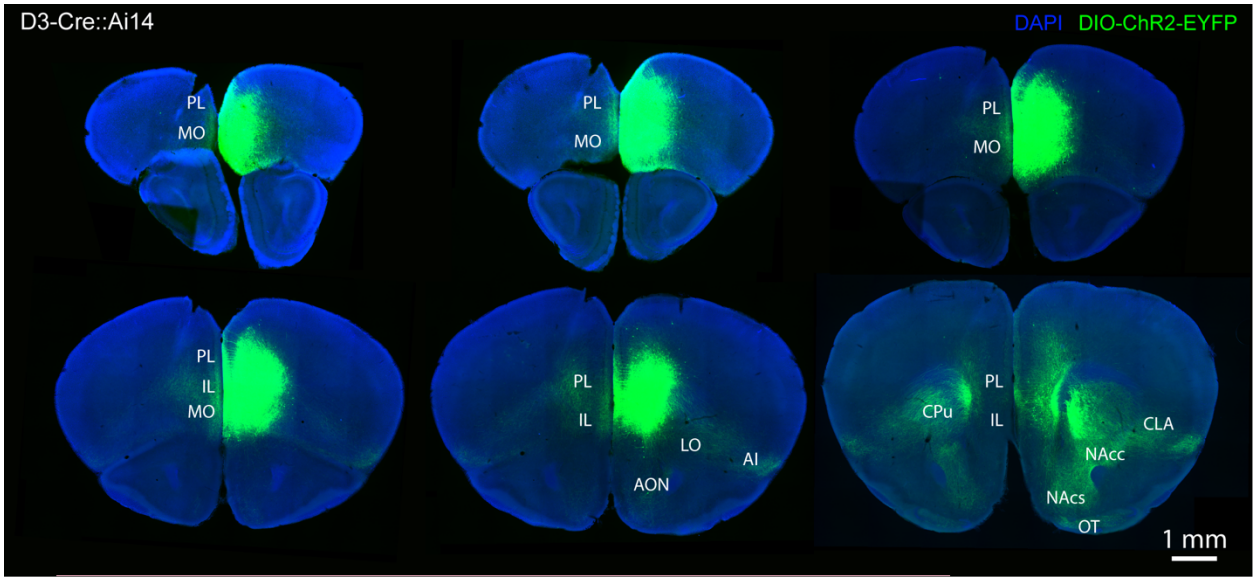

Figure 10. mPFC D3+ neurons project to both contra- and ipsilateral cortex.
Coronal sections of D3-Cre::Ai14 mouse injected with AAV-DIO-ChR2-EYFP in the right hemisphere, with increased gain of the green channel in order to visualize axonal fibers.

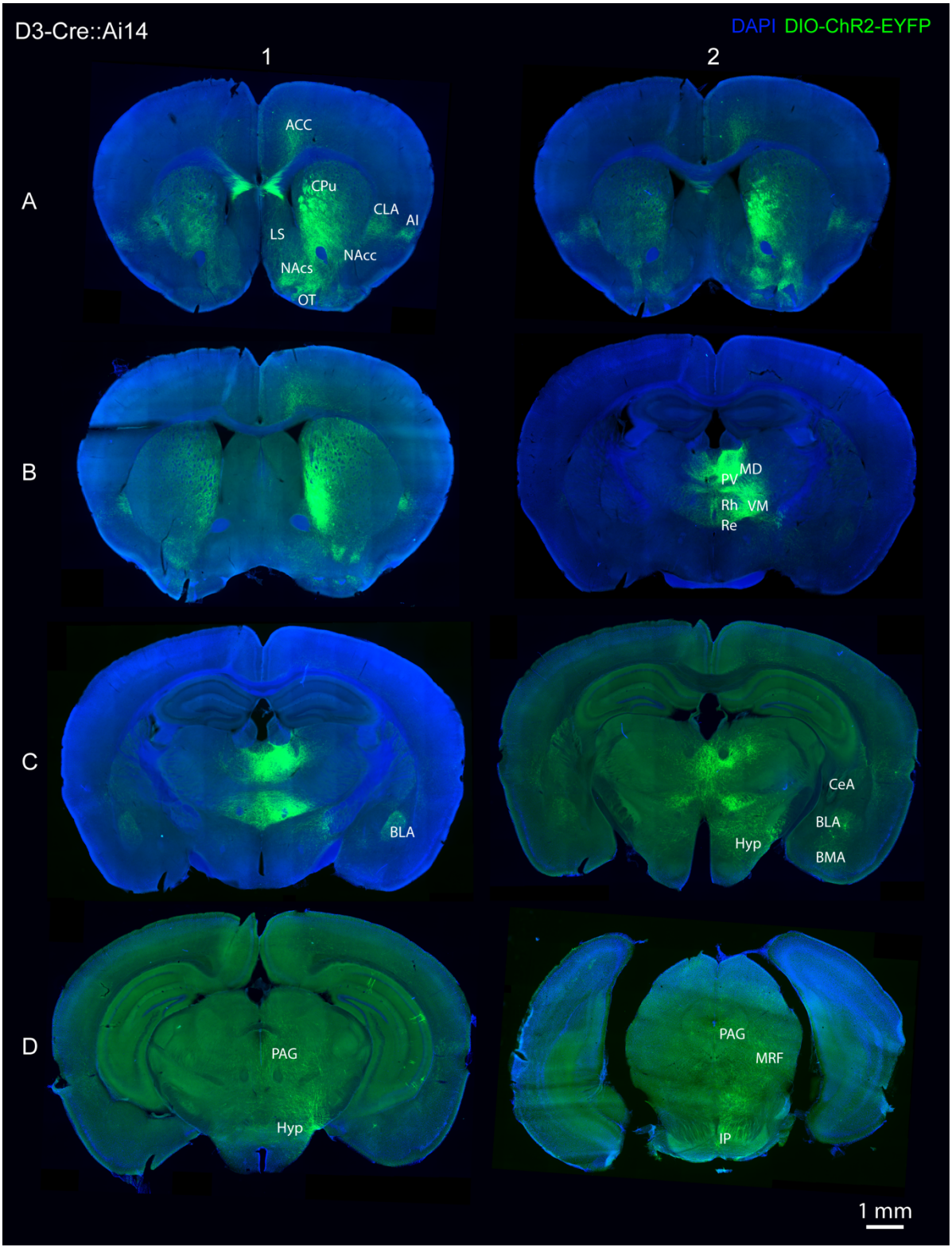

Figure 11. Orthograde tracing reveals additional cortical and subcortical projection targets of mPFC D3+ neurons.
Coronal sections of D3-Cre::Ai14 mouse injected with AAV-DIO-ChR2-EYFP in the right hemisphere.

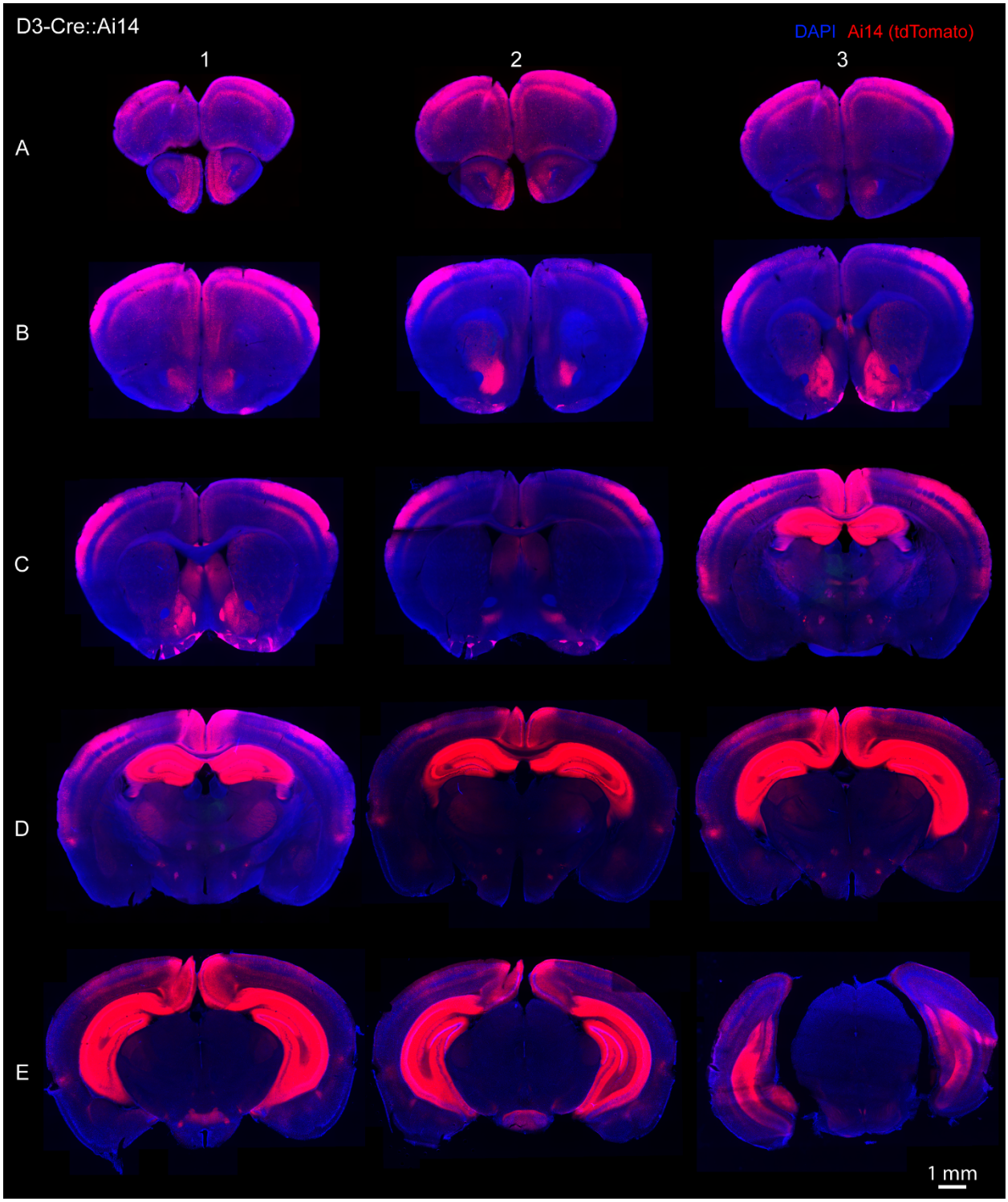

Figure 12. D3R-expressing cells are distributed across the brain.
Coronal sections of D3-Cre::Ai14 mouse, showing D3R expression from the frontal lobes and OB to the midbrain.

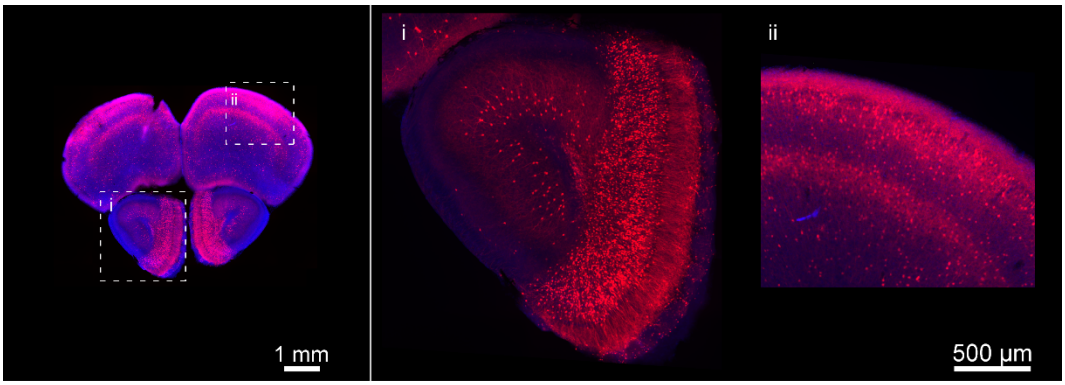

Figure 13. D3+ cells across the brain, 4x magnification (Figure 12, A1)
D3R-expressing cells are found in the OB (i) and the secondary motor area (ii).

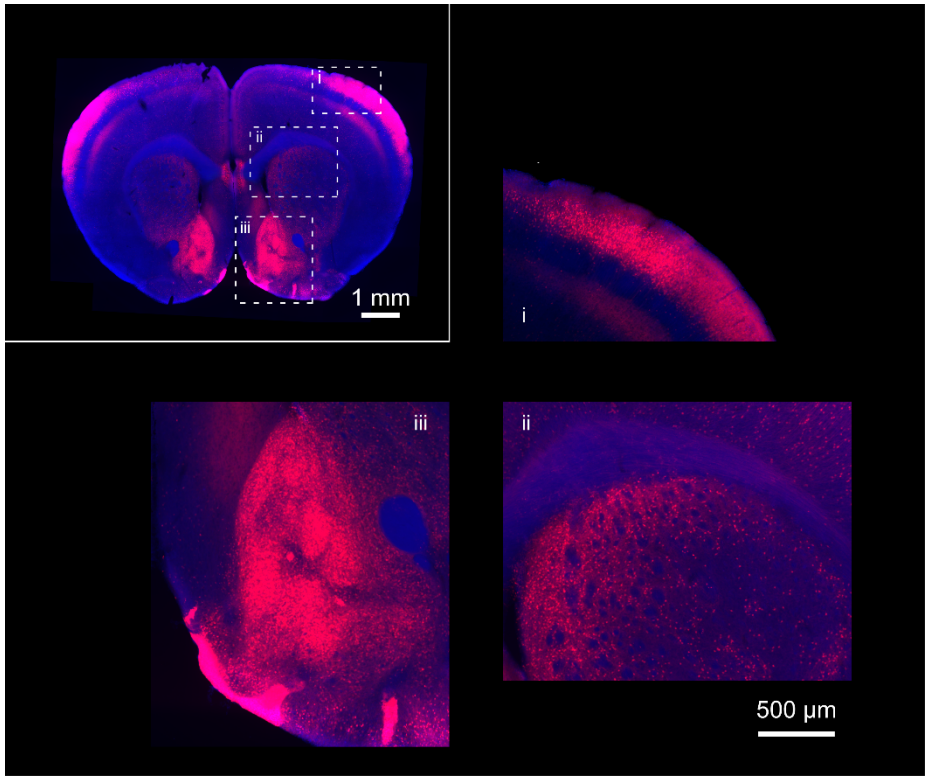

Figure 14. D3+ cells across the brain, 4x magnification (Fig. 12, B3).
D3R-expressing cells are found in the somatosensory cortex (i), dorsal striatum (ii), and ventral striatum (including NAcc, NAcs, and Islands of Calleja) (iii).

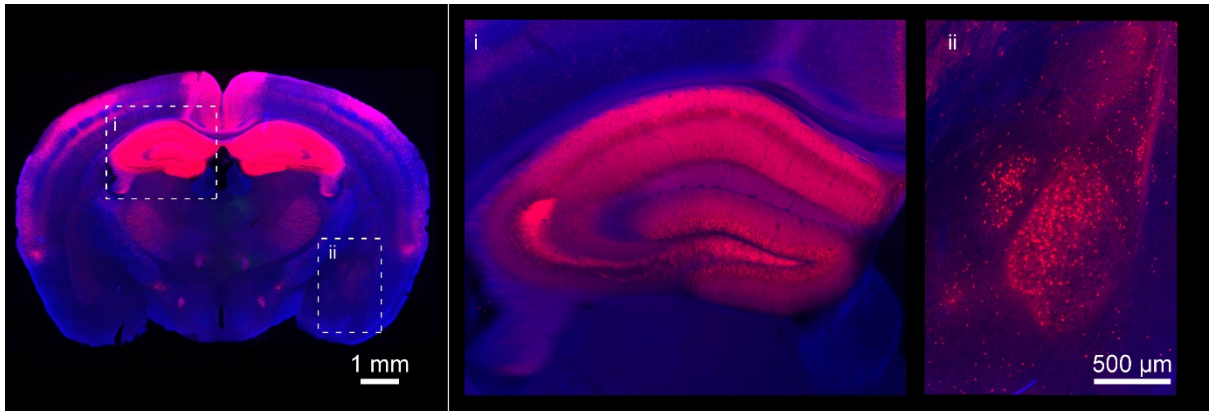

Figure 15. D3+ cells across the brain, 4x magnification (Fig. 12, D1).
D3R-expressing cells are found in limbic regions, including the hippocampus (i) and the amygdala (basolateral and central nuclei) (ii).

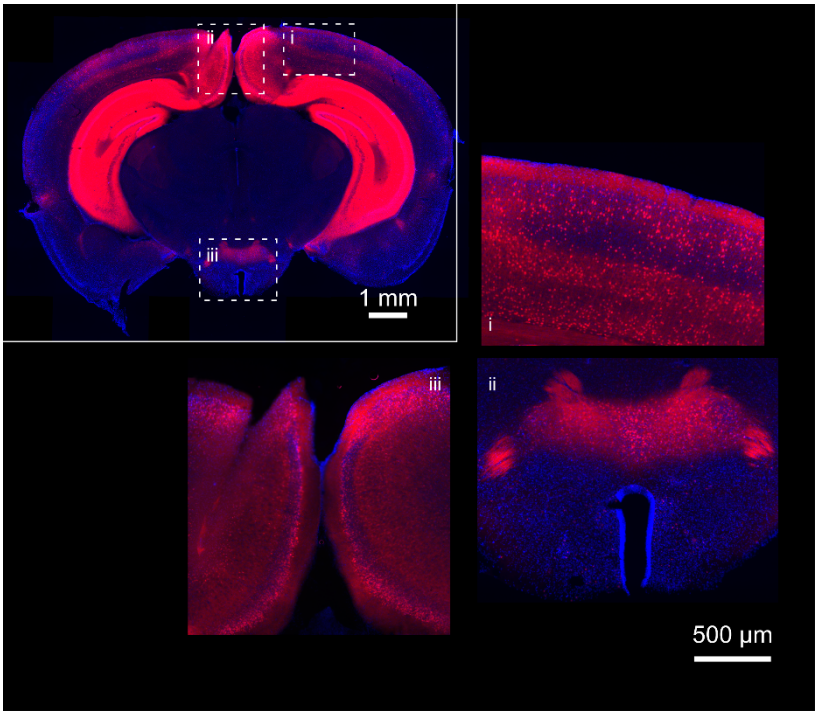

Figure 16. D3+ cells across the brain, 4x magnification (Fig. 12, E1).
D3R-expressing cells are found in the visual cortex (i), the retrosplenial cortex (ii), and part of the hypothalamus (iii).

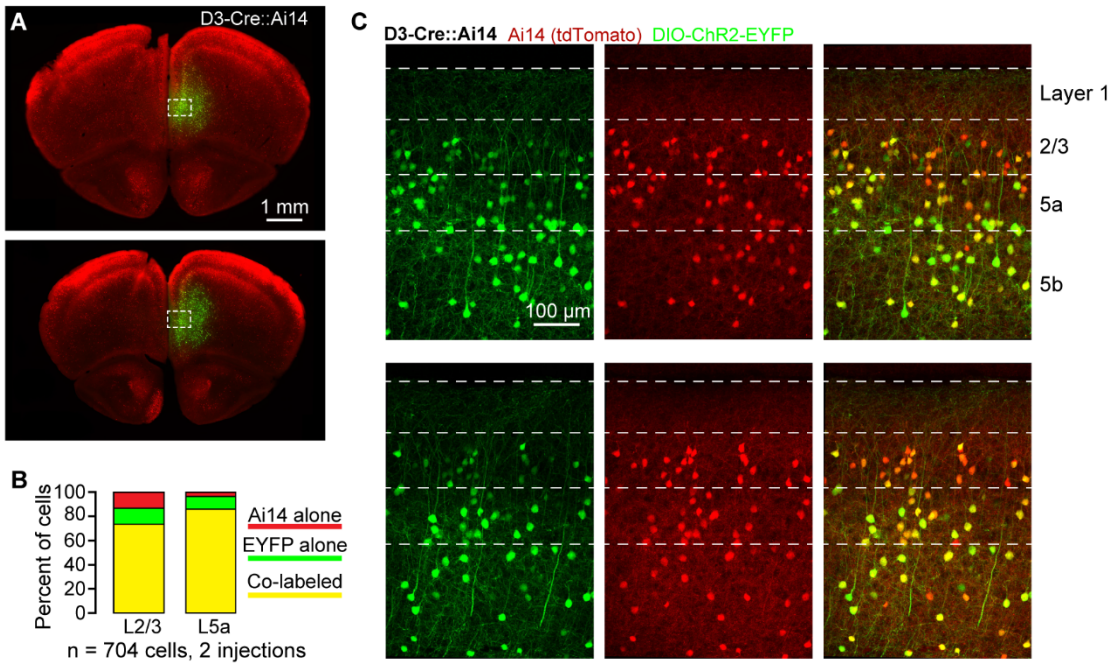

Figure 17. L5 D3+ neurons in D3-Cre::Ai14 express D3R throughout ages studied.
(A) P28 D3-Cre::Ai14 mice (n = 2 animals) were injected in the mPFC with AAV-DIO-ChR2-EYFP.
(B) Ai14, EYFP, and co-labeled cells, as percent of all labeled cells, specifically in L2/3 and L5a.
(C) Confocal images of transfected region (from insets, A), shows EYFP- (left) and Ai14-expression (middle) cells. Right, Image shows strong overlap in expression.

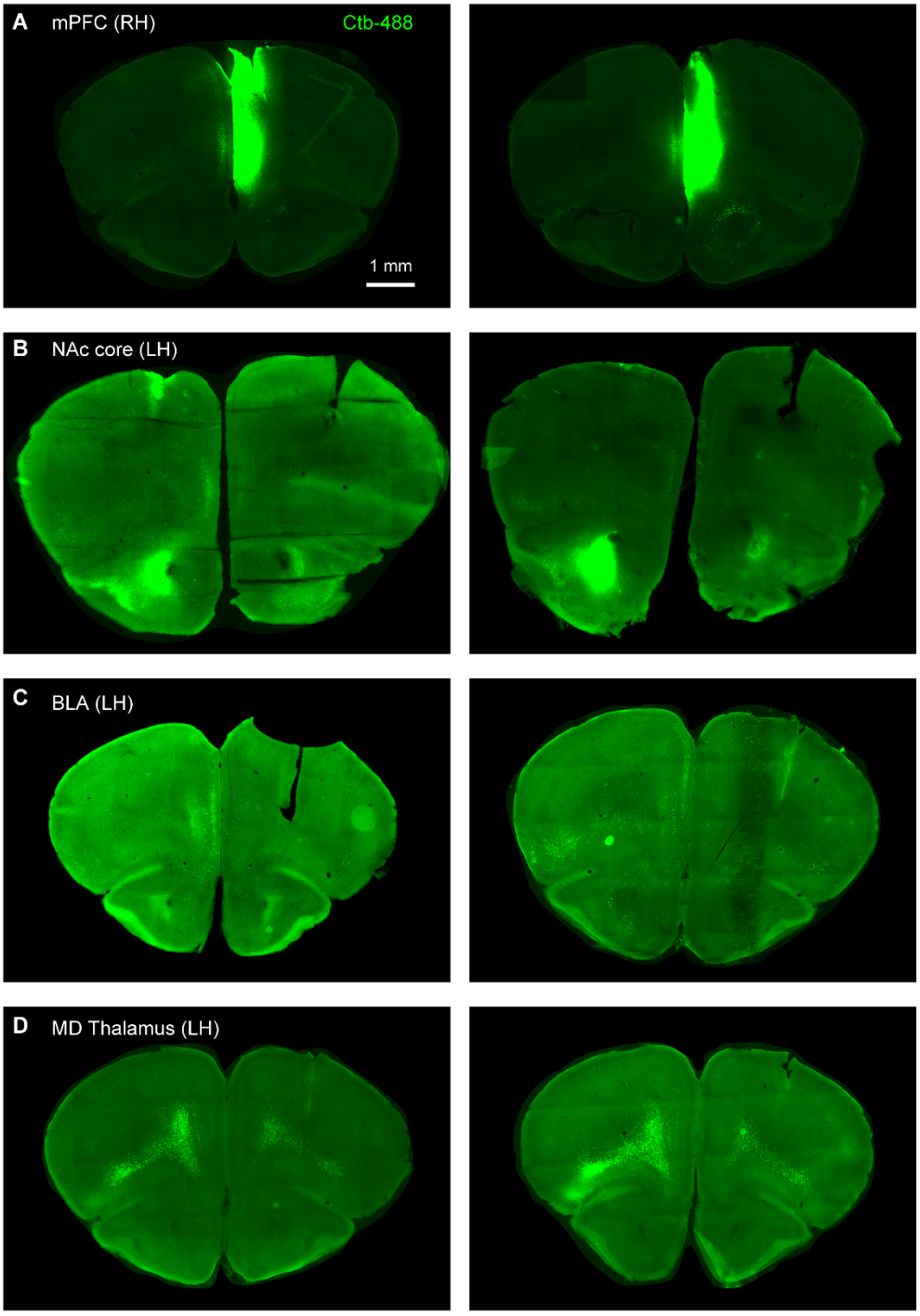

Figure 18. Distribution of retrogradely-labeled cells across mPFC
D3-Cre::Ai14 adult mice were injected in four brain regions with Ctb-488. Widefield images of coronal mPFC sections show retrogradely-labelled cells from mPFC (A), NACc (B), BLA (C), and MD thalamus (D). Each section comes from a different animal.

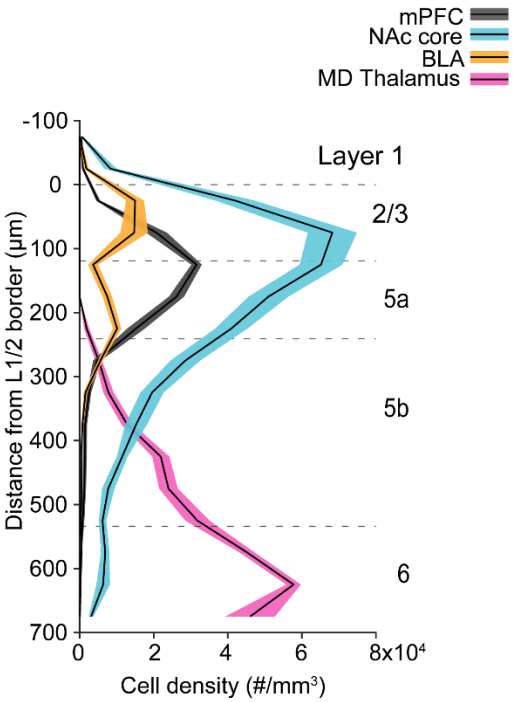

Figure 19. Laminar densities of retrogradely-labeled cells in mPFC
Cell densities of retrogradely-labelled somatic distances from L1/2 border. Data are pooled from two to three injections per group, three to four slices/animal. Solid line with shaded region indicates mean ± SEM.

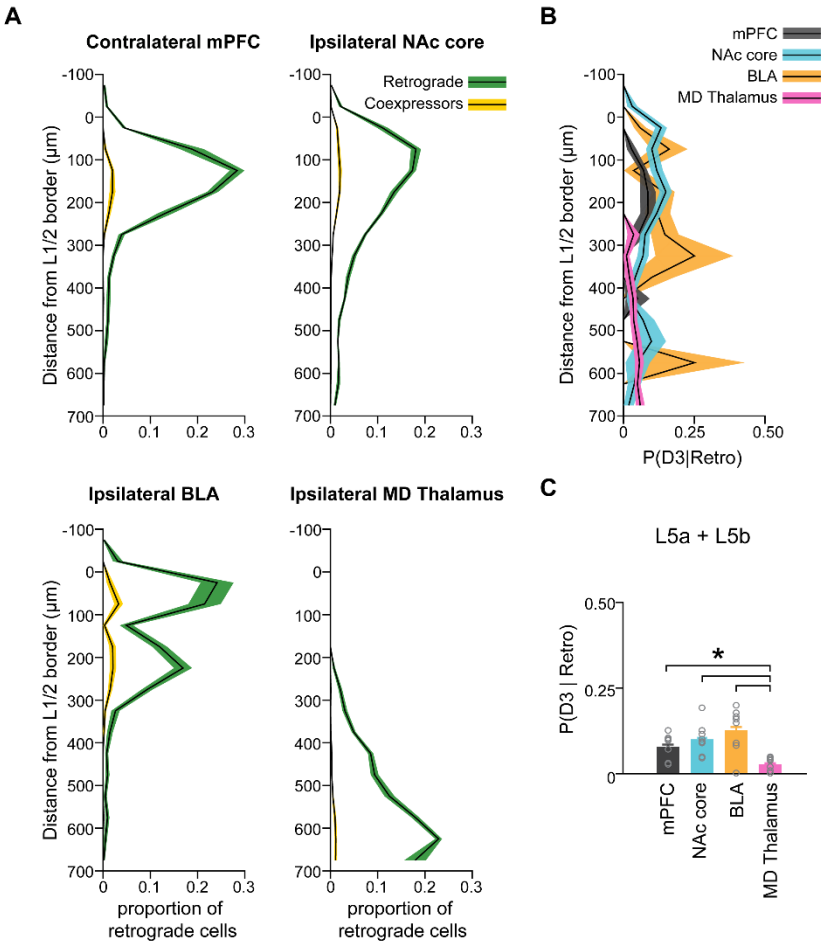

Figure 20. Proportion of D3R+ neurons in retrogradely-labeled populations.

(A) Distribution of somatic distances from L1/2 border for both retrogradely-labeled cells (green) and those colabelled with D3R-marker Ai14 (yellow), normalized to maximum number of retrogradely-labeled cells. Solid line with shaded region indicates mean ± SEM.

(B) Probability that a cell projecting to a particular region was also D3+, plotted as a function of distance from L1/2 border. Solid line with shaded region indicates mean ± SEM.

(C) Probability as in B, specifically in L5. Error bars are mean ± SEM. * = $p < 0.05$, Kruskal-Wallis, Wilcoxon rank sum (Holm-Sidak correction).

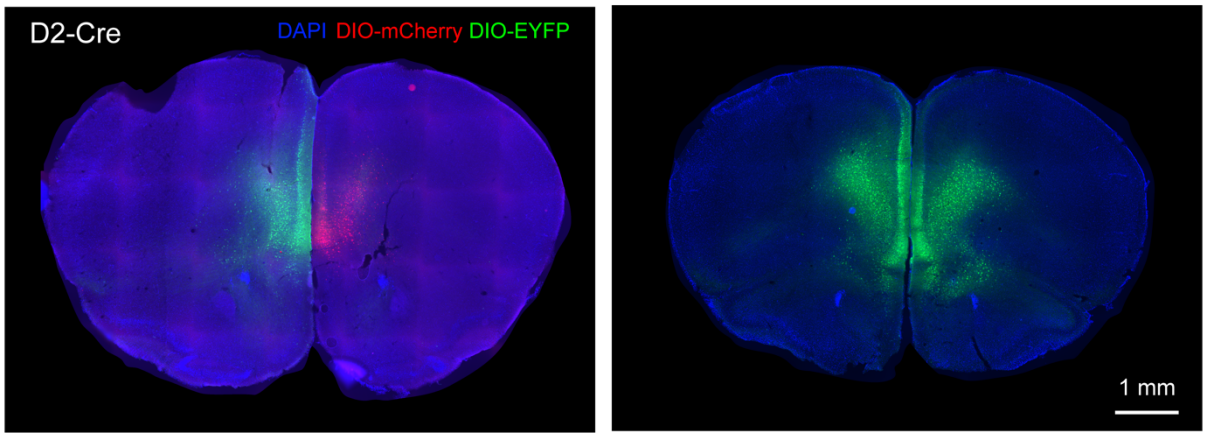

Figure 21. D2+ cell distribution within mPFC
Coronal mPFC sections showing fluorescently labeled (mCherry or EYFP) D2+ cells from D2-Cre mice transfected bilaterally with either AAV-DIO-EYFP or AAV-DIO-mCherry.

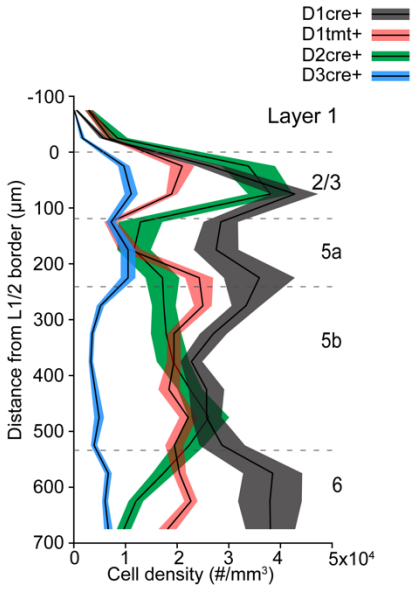

Figure 22. D3+ cells in mPFC comprise a smaller population than D1+ or D2+ cells. Distribution of somatic distances from L1/2 border for D1+, D2+, and D3+ cells, using D1-Cre, D1-tdTomato/D3-Cre, and D2-Cre mice, injected with DIO-mCherry or DIO-ChR2-EYFP. Distributions for each cell type pooled from 3 animals, with 3 slices/animal. Solid line with shaded region indicates mean ± SEM.

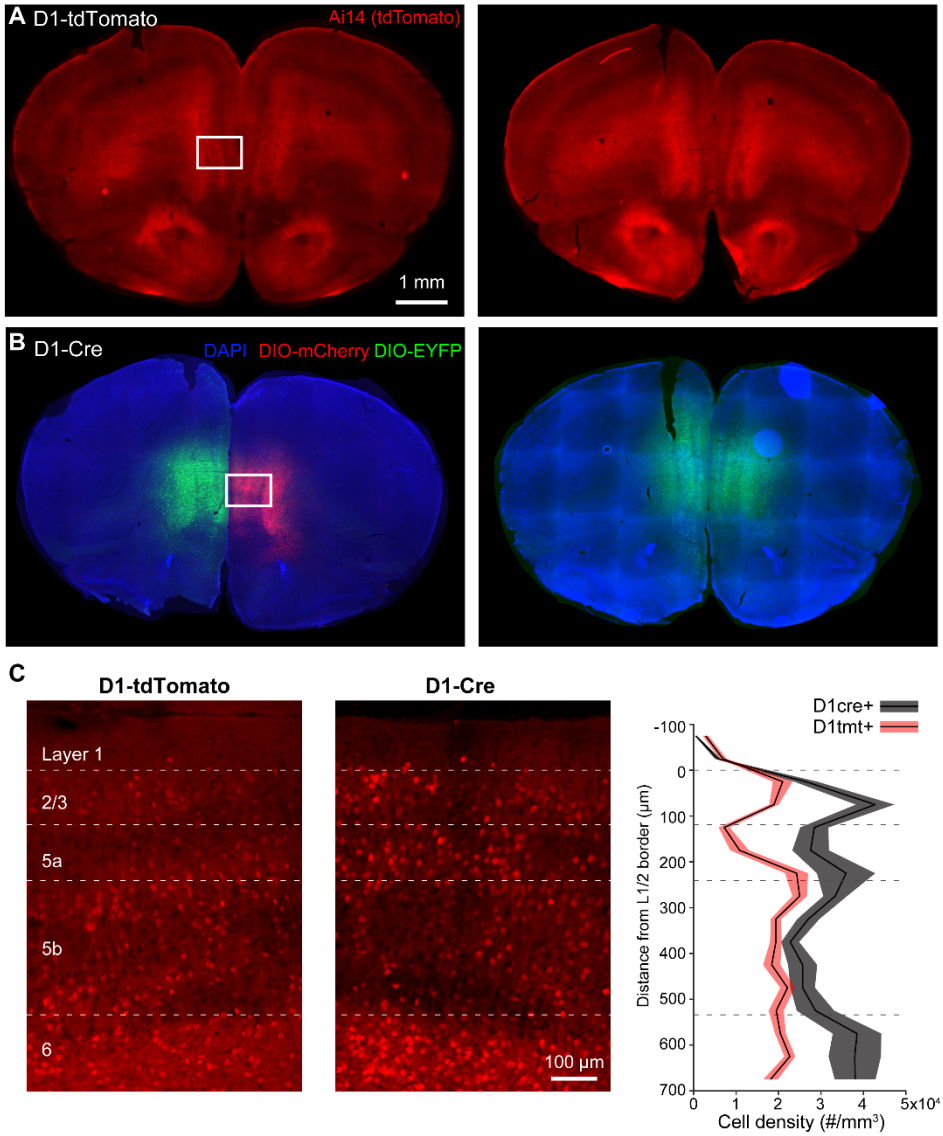

Figure 23. D1R-expressing cells: D1-tdTomato vs. D1-Cre expression

- Coronal mPFC sections from two D1-tdTomato mice.

(D) Coronal mPFC sections from two D1-Cre mice, injected bilaterally with either DIO-mCherry or DIO-EYFP.

(E) Left, middle, Confocal images of mPFC (maximal z-projection) from either D1-tdTomato or D1-Cre mice; region of interest marked in (A) and (B) by white rectangles. Right, Cell densities of D1cre+ and D1tmt+ somatic distances from L1/2 border. Solid line with shaded region indicates mean ± SEM. Histogram data same as in Fig. 22.

Tables

Anatomical Abbreviation	*Brain Region*
ACC	*anterior cingulate cortex*
AI	*agranular insular area*
AON	*anterior olfactory nucleus*
BLA	*basolateral amygdala*
BMA	*basomedial amygdala*
CeA	*central amygdala*
CLA	*claustrum*
CPu	*caudate putamen*
EC	*entorhinal cortex*
Hyp	*hypothalamus*
IL	*infralimbic cortex*
IP	*interpeduncular nucleus*
LO	*lateral orbital cortex*
LS	*lateral septal nucleus*
MD	*mediodorsal thalamus*
MO	*medial orbital cortex*
mPFC	*medial prefrontal cortex*
MRF	*mesencephalic reticular formation*
NAcc	*nucleus accumbens core*
NAcs	*nucleus accumbens shell*
OT	*olfactory tubercle*
PAG	*periaqueductal grey*
PFC	*prefrontal cortex*
PL	*prelimbic cortex*
PV	*paraventricular nucleus*
Re	*nucleus of reunions*
Rh	*rhomboid nucleus*
VM	*ventral medial nucleus*

Table 3. Anatomical Abbreviations

References

Bouthenet, M.-L., Souil, E., Martres, M.-P., Sokoloff, P., Giros, B., and Schwartz, J.-C. (1991). Localization of dopamine D3 receptor mRNA in the rat brain using in situ hybridization histochemistry: comparison with dopamine D2 receptor mRNA. Brain Res. *564*, 203–219.

Burris, K. (1995). Lack of Discrimination by Agonists for D2 and D3 Dopamine Receptors. Neuropsychopharmacology *12*, 335–345.

Clarkson, R.L., Liptak, A.T., Gee, S.M., Sohal, V.S., and Bender, K.J. (2017). D3 Receptors Regulate Excitability in a Unique Class of Prefrontal Pyramidal Cells. J. Neurosci. *37*, 5846–5860.

DeNardo, L.A., Berns, D.S., DeLoach, K., and Luo, L. (2015). Connectivity of mouse somatosensory and prefrontal cortex examined with trans-synaptic tracing. Nat. Neurosci. *18*, 1687–1697.

Diaz, J., Pilon, C., Le Foll, B., Gros, C., Triller, A., Schwartz, J.C., and Sokoloff, P. (2000). Dopamine D3 receptors expressed by all mesencephalic dopamine neurons. J.Neurosci. *20*, 8677–8684.

Gee, S., Ellwood, I., Patel, T., Luongo, F., Deisseroth, K., and Sohal, V.S. (2012). Synaptic activity unmasks dopamine D2 receptor modulation of a specific class of layer V pyramidal neurons in prefrontal cortex. J. Neurosci. *32*, 4959–4971.

Gurevich, E. V, and Joyce, J.N. (2000). Dopamine D(3) receptor is selectively and transiently expressed in the developing whisker barrel cortex of the rat. J. Comp. Neurol. *420*, 35–51.

Hall, H., Halldin, C., Dijkstra, D., Wikström, H., Wise, L.D., Pugsley, T.A., Sokoloff, P., Pauli, S., Farde, L., and Sedvall, G. (1996). Autoradiographic localisation of D3-dopamine receptors in the human brain using the selective D3-dopamine receptor agonist (+)-[3H]PD 128907. Psychopharmacology (Berl). *128*, 240–247.

Hoover, W.B., and Vertes, R.P. (2011). Projections of the medial orbital and ventral orbital cortex in the rat. J. Comp. Neurol. *519*, 3766–3801.

Land, B.B., Narayanan, N.S., Liu, R.J., Gianessi, C.A., Brayton, C.E., Grimaldi, D.M., Sarhan, M., Guarnieri, D.J., Deisseroth, K., Aghajanian, G.K., et al. (2014). Medial prefrontal D1 dopamine neurons control food intake. Nat. Neurosci. *17*, 248–253.

Meador-Woodruff, J.H., Damask, S.P., Wang, J., Haroutunian, V., Davis, K.L., and Watson, S.J. (1996). Dopamine receptor mRNA expression in human striatum and neocortex. Neuropsychopharmacology *15*, 17–29.

Seong, H.J., and Carter, A.G. (2012). D1 receptor modulation of action potential firing in a subpopulation of layer 5 pyramidal neurons in the prefrontal cortex. J. Neurosci. *32*, 10516–10521.

Sokoloff, P., Giros, B., Martres, M.P., Bouthenet, M.L., and Schwartz, J.C. (1990). Molecular cloning and characterization of a novel dopamine receptor (D3) as a target for neuroleptics. Nature *347*, 146–151.

Stanwood, G.D., Artymyshyn, R.P., Kung, M., Kung, H.F., Lucki, I., and Mcgonigle, P. (2000). Quantitative Autoradiographic Mapping of Rat Brain Dopamine D3 Binding with [125 I] 7-OH-PIPAT : Evidence for the Presence of D3 Receptors on Dopaminergic and Nondopaminergic Cell Bodies and Terminals 1. J. Pharmacol. Exp. Ther. *295*, 1223–1231.

Suzuki, M., Hurd, Y.L., Sokoloff, P., Schwartz, J.-C., and Sedvall, G. (1998). D3 dopamine receptor mRNA is widely expressed in the human brain. Brain Res. *779*, 58–74.

Vertes, R.P. (2004). Differential projections of the infralimbic and prelimbic cortex in the rat. Synapse *51*, 32–58.

Chapter 4

Machine learning approach to neuronal classification: prefrontal pyramidal neuron dopamine receptor-expressing subtypes

Abstract

To understand how anatomical and functional neuronal connections give rise to neural circuits and ultimately drive behavior, it is critical to systemically identify the distinct types of neurons comprising these circuits. To understand the whole, we must clearly identify the parts. Systematic identification with complex datasets can be greatly facilitated via the implementation of machine learning techniques. In Chapter 2, we applied supervised machine learning to prefrontal neurons expressing either the D1 receptor (D1R) or D3 receptor (D3R), finding that five electrophysiological parameters were sufficient to predict genetic marker expression. Here, I elaborate on the exploratory data analysis techniques used to develop this classifier, both by displaying the full set of analyzed electrophysiological features, and also through highlighting experimental concerns of relevance for the development of future classification efforts in the field.

Introduction

Historical background of neuronal cell types

Early neuroanatomists supported the “reticular theory” of the nervous system, which postulated that the nervous system was a diffuse and continuous network of nerve fibers. However, tremendous technical advances in both microscopy and cytohistological methods during the latter half of the 19th century provided the

groundwork for Santiago Ramón y Cajal's revolutionary "neuron doctrine". The neuron doctrine states that the nervous system is comprised of discrete functional units (i.e. neurons), as opposed to a diffuse and continuous network (DeFelipe, 2013). Cajal's observations were derived from his usage of and improvements on the recently developed Golgi stain, which allowed observation of the full extent of neuronal processes, revealing their axonal and dendritic morphology (López-Muñoz et al., 2006). Once it was understood that the nervous system was comprised of separate cells, the process of identifying these distinct types could begin.

Historically, neuronal cell type identification has been largely qualitative, employing descriptive methods. For example, Cajal drew detailed neuronal morphologies, conveying the neuronal diversity both within and between different brain regions (López-Muñoz et al., 2006). Qualitative analyses provided crucial insight into both the structure and function of neuronal cell types, such as the identification of the two major cortical neuron classes: glutamatergic pyramidal neurons with long-range connections, and GABAergic interneurons, with predominantly local connectivity. Pyramidal neurons and interneurons were initially purely morphologically defined – first by cell body shape, and subsequently by the extent of their axonal arborization: "long axon" projection neurons as compared to "short axon" neurons whose processes did not leave the local circuit (DeFelipe, 2002).

However, both pyramidal and interneuron classes are themselves incredibly diverse, and this neuronal complexity can preclude obvious demarcations in cell type, especially with increasingly rich datasets. Fortunately, in recent decades, computational methods have become available that can capitalize on larger experimental data sets to

allow for the systematic and automatic classification of neurons, regardless of experimental domain.

Machine learning applications for neuroscience

Machine learning techniques provide a powerful set of tools for finding patterns within data. These computer algorithms can learn from and make predictions about experimentally-determined biological variables. For example, as applied to the problem of neuronal cell type classification, this biological data could include electrophysiological, morphological, and molecular properties. Both unsupervised and supervised machine learning techniques can be applied to the problem of neuronal type identification (Armañanzas and Ascoli, 2015).

Unsupervised classifiers probe for the number (or even existence) of distinct neuron classes within an unlabeled dataset, looking for hidden patterns in the data that best explain any observed variability. These are largely exploratory techniques for discovering new cell types; these methods have been used extensively for interneuron subtype classification (Cauli et al., 2000; Karube et al., 2004; Helmstaedter et al., 2009; Karagiannis et al., 2009; McGarry et al., 2010). For example, McGarry et al., 2010 identified three somatostatin-positive interneuron subtypes; importantly, they found that clustering on 19 electrophysiological variables agreed well with an independent clustering based on 16 morphological variables. In a different study, Karagiannis et al., 2009 gathered data on 200 neuropeptide Y (NPY)-expressing cortical neurons, including laminar location and electrophysiological and molecular properties. Through multiple unbiased unsupervised methods, they confirmed that NPY-expressing neurons

are GABAergic and found that they can be divided into three distinct classes. In addition, unsupervised clustering techniques have distinguished dopamine midbrain neuron subtypes (Lammel et al., 2008) as well as layer 2/3 (L2/3) pyramidal neuron subtypes in monkey prefrontal cortex (Zaitsev et al., 2012).

While an advantage of unsupervised machine learning is its independence from prior assumptions, this can also be a disadvantage; unsupervised clustering techniques ignore prior knowledge that could guide classification. For example, one study found that supervised approaches outperformed unsupervised clustering for distinguishing pyramidal neurons from interneurons (with “ground truth” defined as presence of an apical dendrite), with classification based solely on other morphological parameters (Guerra et al., 2011).

In supervised machine learning, known class labels guide learning about the relationship between the inputs and these labels (Armañanzas and Ascoli, 2015), thus allowing for a predictive mapping between experimental variables (e.g. electrophysiology, morphology) and a known aspect of cell identity (e.g. molecular marker expression). In other words, are there electrophysiological features that can be used to predict what molecular marker is expressed? To my knowledge, the majority of automated neuronal cell type classification research thus far has implemented unsupervised techniques. However, as described above, supervised learning approaches to classification outperform unsupervised methods when some information is known *a priori,* and additionally can be used to determine how well measured experimental variables can predict group membership.

Supervised machine learning for prefrontal pyramidal cell classes

In Chapter 2, we recorded from fluorescently-labelled D1R-, D2R-, and D3R-expressing pyramidal neurons in layer 5 (L5) medial prefrontal cortex (mPFC), and asked whether these electrophysiological variables could predict dopamine receptor expression. Given that D2R-expressing (D2+), "Type 2" pyramidal neurons can be distinguished from both D1R-expressing (D1+) and D3R-expressing (D3+) neurons by a single electrophysiological parameter (Gee et al., 2012; Seong and Carter, 2012), we focused on the D1+ and D3+ cell populations. D1+ and D3+ neurons could not individually be distinguished from each other via any single parameter, though as a population these groups were clearly different (Figs. 2, 3). Given that class labels were already known (D1+, D3+), this provided a perfect opportunity to employ supervised machine learning for automated cell classification.

By employing supervised machine learning to determine what electrophysiological parameters (if any) accurately predicted D1R- or D3R-expression, we could 1) test the hypothesis that D1+ and D3+ L5 mPFC pyramidal neurons were separate cell classes and 2) apply the resulting classifier to previously recorded nongenetically identified cells. We wanted apply this classifier to previous recordings because these recordings included numerous pharmacological manipulations that would have been both expensive and time-consuming to replicate in the transgenic mouse lines.

Prior to algorithmic selection and implementation, it is crucial to examine the full dataset. In Chapter 4, I display many components of the exploratory and preparatory analyses done prior to the classification done in Chapter 2. First, I visualized the

distributions of all electrophysiological variables. Second, given that data was collected across multiple experimenters and experimental conditions, I performed a thorough inventory of the dataset to check for missing data (i.e. were all features known for all cells), and assessed potential influences of experimental variability. Finally, I selected optimal electrophysiological features for the classifier, removing highly correlated variables providing redundant information.

Materials and Methods

Electrophysiological Recordings.

Electrophysiological recordings were performed as described in Chapter 2, Materials and Methods, “Electrophysiological recordings.” In brief, para-coronal mPFC slices were made from post-natal day (P)25-60 D1-tdTomato or D3-Cre::Ai14 transgenic mice. Following 30 minutes incubation at 33°C in either sucrose cutting solution or ACSF recording solution, slices were moved to room temperature. Whole-cell current clamp recordings were then performed in mPFC L5, using a K+-gluc-based internal solution containing either EGTA (100 μM) or Fluo-5F (250 μM) as a Ca buffer (Fluo-5F used for Ca imaging experiments as reported in Chapter 2).

Electrophysiological analysis for classification

As described in Materials and Methods, Chapter 2, “Electrophysiological analysis for classification,” electrophysiological characteristics (sag/rebound, action potential [AP] spike train/waveform) were determined from voltage responses to hyperpolarizing (−400 pA, 120 ms) and depolarizing (300 ms, 20–300 pA) square current pulses from a

holding potential of −80 mV. Electrophysiological data reported in this chapter comprises the subset of recordings used for classification of non-Type 2 D1+ and D3+ neurons in Chapter 2.

Sag and rebound variables

As implemented in the final classifier from Chapter 2, *sag amplitude* was defined as the one-term exponential model fit to the voltage between peak sag onset and the end of the current pulse. In Chapter 3, this is called *sag amplitude fit* for differentiation from other measurements of sag amplitude; *sag tau fit* is the associated time constant. *Latency to peak sag* was calculated as the time from current pulse onset to the negative peak of the voltage. Initial exploratory analyses involved additional calculations of both sag amplitude and sag timing. *Absolute sag* was defined as the difference between peak sag voltage and the steady state voltage reached during the current pulse. *Normalized sag* was defined as absolute sag divided by the voltage difference between peak sag and baseline. *Sag onset time* was defined as the duration after current onset for a voltage decrease from 20-80% of the difference between the peak sag voltage and the voltage at current onset.

Rebound time constant, as implemented in the final classifier, was defined as the duration after current offset for a voltage increase from 20–80% of the difference between the peak rebound voltage and the voltage at current offset. *Latency to peak rebound* was defined as the time from the end of the current pulse to the maximum voltage within 230 ms of pulse offset. *Rebound amplitude* was defined as the difference between baseline and the maximum voltage within 230 ms of pulse offset.

AP waveform and spike train shape variables

Numerous AP waveform and train shape variables (threshold, AP amplitude, afterhyperpolarization potential [AHP], spike width, AP rate of rise, AP rate of fall, doublet index) were defined in Chapter 2, Materials and Methods, "Electrophysiological analysis for classification." In addition, *AHP* timing is defined as the time from AP peak amplitude to the AHP. *AHP timing ratio 1* and *AHP timing ratio 2* are the ratios of each later AHP timing to the first or second AHP timing, respectively. Finally, *adaptation ratio* 1 and *adaptation ratio 2* are the ratios of each subsequent interspike interval (ISI) to the first or second ISI, respectively.

Cross-validation of linear discriminant classifiers

For model evaluation, cross-validation was performed as described in Chapter 2, Materials and Methods: "Linear discriminant analysis (LDA): model development and application." In brief, model accuracy was evaluated with repeated holdout cross-validation (2000x), with the labelled data randomly partitioned into a training set (90%) and testing set (10%). In each round, prediction accuracy was evaluated by calculating the percentage of correctly identified cells in the testing set when using the linear discriminant defined by the training set. Predication accuracy was averaged across rounds.

Results

Initial exploratory analysis of electrophysiological features

For my initial exploratory analysis, I examined the distributions of all electrophysiological features extracted from whole cell patch clamp recordings of genetically-identified D1+ and D3+ non-Type 2 neurons. Histograms facilitated qualitative assessment of normality, while boxplots clarified the degree of separation between the populations (Figs. 24-36). As noted previously, no one variable cleanly discriminated D1+ and D3+ populations, but significant differences were seen across many different electrophysiological features.

I started with baseline measurements of resting membrane potential (V_m) and input resistance (R_{in}), as well as the relationship between injection current and firing frequency ("FI Curve"), gathering information about cellular excitability. FI curve slope and R_{in} differed between D1+ and D3+ cell populations. Interestingly, despite D3+ cells having higher average R_{in}, they had a smaller FI curve slope, with current injection having smaller relative effect on AP frequency (Fig. 24) (though both variables strongly overlapped between the D1+ and D3+ cell populations).

Given that previous studies show that different prefrontal pyramidal cell classes express varying degrees of "h-current," corresponding to hyperpolarization-activated cyclic nucleotide-gated (HCN) channel expression (Gee et al., 2012; Seong and Carter, 2012; Kalmbach et al., 2013), I examined responses to large hyperpolarizing current injection (-400 pA), looking at measurements of sag and rebound. D3+ cells had a delayed onset to peak sag, as well as smaller sag values across all sag amplitude variables (Fig. 25). Latency to peak rebound values were statistically different between

the populations, but in all cases latencies were extremely delayed compared to current offset (Fig. 26); these differences were likely driven by differences in rebound time constant, and not indicative of the canonical “rebound” of high HCN channel expression.

Finally, I examined AP spike train and waveform properties, conceptualizing these as three main groups: 1) AP shape (within the spike train) 2) overall spike train shape, and 3) spike frequency adaptation. Here, I show the results for 6 AP spike trains (20 Hz firing). With respect to individual AP shape, D3+ neurons had both slower rate of rise and slower rate of fall, and therefore, as expected, broader APs than D1+ neurons (Figs. 27-29). These cell populations also differed in terms of the spike train shape, with D3+ neurons consistently having more depolarized threshold and AHP values for later APs in the spike train, compared to the first AP (Figs. 30, 31). Finally, I examined spike train adaptation measures (Figs. 33-37). D1+ neurons had a tighter initial doublet (Fig. 33), but less overall adaptation following this doublet (note plateau of ISI ratios for D1+ neurons as compared to the linearly increasing ISIs for D3+ neurons; Fig. 37).

Dataset observation: experimental differences between recordings, incomplete data

The genetically-labelled dataset contained electrophysiological parameters from a total of 268 genetically-identified (D1+ or D3+) neurons. In addition, a second dataset contained electrophysiological parameters from 124 non-fluorescently identified neurons. As described in Chapter 2, we replaced EGTA with Fluo5 for our calcium imaging experiments; therefore, both datasets had a mixture of recordings with either EGTA or Fluo5 as the Ca buffer in the internal solution (Table 4). Given that Ca currents play important roles in determining both AP shape and firing patterns (Bean, 2007), I

examined whether Ca buffer affected spiking parameters. Spiking properties for D3+ neurons differed depending upon Ca buffer, with Fluo5 resulting in a broader AP waveform and decreased spike frequency adaptation (Figs 38, 39). Therefore, for classification purposes, I divided the datasets based on Ca buffer.

In addition to Ca buffer variability, the electrophysiological recordings in both datasets varied with respect to FI curve completeness. In particular, the data for the non-fluorescently labeled cells were sparse (Table 5). These recordings were done prior to D3+ mouse line recovery from cryo-preservation; our initial assumption, based upon earlier characterization of the D1+ and D2+ populations (Gee et al., 2012; Seong and Carter, 2012), was that sag and rebound properties would distinguish D3+ neurons. Initial qualitative observations of a novel cell population with D3R-dependent modulation that had low or no sag supported this assumption, but recordings from D3+ neurons revealed a broad spread in sag amplitudes that overlapped the D1+ distribution. Therefore, we examined spiking properties for separating D1+ and D3+ neuron populations.

Given the relatively sparse data in the non-fluorescently identified neuron population, an optimal classifier needed to accommodate a range of firing frequencies. However, AP firing and spike train properties differed based on how many APs were elicited within the 300 ms depolarizing current injection (Fig. 40). Therefore, in addition to creating separate classifiers for EGTA and Fluo5 recordings, separate classifiers were needed for 3-8 APs per 300 ms current pulse.

Feature selection: correlation analysis for removing redundant variables

The exploratory data analysis began with a large number of electrophysiological variables. We found that many of these variables were strongly correlated, and therefore simplified our model by selecting only a subset of these features to avoid overfitting. After initial visualization with numerous pairwise scatterplots (data not shown), I examined the overall dataset structure with correlation matrix heat maps, in which all pairwise correlations from 0 to 1 (calculated as the absolute value of the Pearson correlation coefficient) are graphically represented by color (Fig. 41). Variables were grouped into subsets: baseline, sag/rebound, and spiking.

Between these major variable groups (e.g. baseline vs. spiking, spiking vs. sag/rebound), there were minimal correlations (Fig. 41A, B), confirming that these groups measured distinct physiological properties. However, there were substantial within-group correlations for the sag variables and spiking variables. Unsurprisingly, all measurements of sag amplitude (normalized sag, absolute sag, sag amplitude fit) were highly correlated (Fig. 41C, middle), but sag vs. rebound variable pairwise correlations were low. Spiking variables were divided into three subsets: adaptation, train shape, and AP shape; low between-group and high within-group correlation indicated that these variable divisions captured distinct spiking properties (Fig. 41C, right; Fig. 41D).

By combining knowledge of the overall data structure (Fig. 41) with D1+ and D3+ neuron variable distributions (Figs. 24-36), I chose 5 variables to capture the prominent discriminating electrophysiological features: sag amplitude fit, rebound time constant, log of the doublet index (ratio of 2^{nd} ISI to 1^{st} ISI, from “adaptation ratio 1” measurements), difference in AP threshold between first and last AP, and rate of AP

rising phase for the last AP in the spike train. All variables were not strongly non-normal (Lilliefors test, $p < 0.001$).

Application of supervised machine learning algorithm: linear discriminant analysis

Finally, I chose linear discriminant analysis (LDA), a supervised machine learning algorithm, as it is a robust classifier for discriminating two labelled classes (assuming normally distributed features), with easily interpreted results (Fisher, 1938; Li et al., 2006; Vasques et al., 2016). By fitting linear discriminant functions to the D1+ and D3+ cell data, I determined that a linear combination of the chosen five electrophysiological features could successfully predict D1R- or D3R-expression, as verified through cross-validation (>70% accuracy for all classifiers, Fig. 2E). This analysis required 12 total classifiers, depending on Ca buffer in the recording pipette (EGTA or Fluo-5F) and number of APs evoked in 300 ms (3–8 APs). The final set of classifiers was applied to all nongenetically identified cells to predict D1R or D3R expression, with the addition of an "exclusion zone" to further increase prediction accuracy, as described in Chapter 2. Here, I visualize two examples of this classification technique as applied to nongenetically identified cells (Figs. 42, 43).

In LDA, the standardized discriminant function coefficients (Table 1) can be used to assess the importance of each variable's contribution in discriminating the two labelled groups (Fig. 44). Overall, spiking variables made a larger contribution to the discriminant functions than either sag or rebound. Interestingly, in addition, both the doublet index and AP rate of rise increased their impact on discrimination at higher AP frequencies. Given these observations, I compared cross-validation accuracy of the final

linear discriminant classifier (across all frequencies and Ca buffers) with classifiers generated from either the three AP spiking variables or sag and rebound. Spiking variables alone could discriminate D1+ and D3+ cells nearly as well as all 5 variables, while a model based on sag and rebound alone performed much more poorly (Fig. 45).

Discussion

LDA, a supervised machine learning approach, enabled the discrimination of D1+ and D3+ cell populations, despite considerable overlap in their electrophysiological variable distributions; as previously noted, no single feature was sufficient to distinguish these populations. Analysis of the discriminant classifier itself provided insight into the critical parameters distinguishing D1+ and D3+ neurons, highlighting the strength of automated classification techniques. In this chapter, I showed the full development of the D1+ and D3+ cell type classification described in Chapter 2, from data visualization and feature selection to model choice and validation. During this process, I reflected upon details of experimental method and data collection, including challenges encountered in this analysis that may inform future experimental preparation and data collection techniques.

Possible electrophysiological features for a neuronal model

Though ultimately 5 variables were chosen for the discriminant classifier, there were many possible electrophysiological features to base a model upon; understanding key features prior to model selection enabled rational choice of relevant variables. A neuron's subthreshold and suprathreshold electrophysiological properties critically

contribute to its role in neuronal information processing. By comprehensively assessing and then describing these properties one can begin to isolate key features defining a neuronal population. Subthreshold properties include passive membrane properties (e.g. resting membrane potential, input resistance) and hyperpolarization-evoked responses, while suprathreshold properties include both AP waveform and complex AP firing patterns, evoked by depolarizing current injection.

Of the subthreshold properties, responses to hyperpolarizing current injection were of particular interest, as hyperpolarization activates HCN channels, expression of which is known to differ between cortical pyramidal cell classes (Sheets et al., 2011; Gee et al., 2012; Kalmbach et al., 2013). This h-current strongly modulates a neuron's input-output properties (Shah, 2014). For example, corticospinal specific HCN-channel expression reduced summation of incoming synaptic inputs; blocking this channel facilitated the ability of presynaptic inputs to drive spiking (Sheets et al., 2011).

AP shape differs dramatically between neuronal subtypes across the brain (Bean, 2007), from extremely narrow APs of fast-spiking interneurons (McCormick et al., 1985) to the much broader APs of many (though not all) midbrain dopamine neurons (Lammel et al., 2008; Margolis et al., 2008). In both cortex and hippocampus, GABAergic interneurons typically have narrower spikes than glutamatergic pyramidal neurons; this is clearly seen with intracellular recordings (McCormick et al., 1985), but can also be used to distinguish these cell types *in vivo* (Henze et al., 2000; Klausberger et al., 2003).

Finally, APs are proposed to encode information in their frequency and firing pattern, thereby shaping a neuron's impact on both the local circuit and downstream

targets. For example, high frequency AP bursts encode distinct information from single spikes, increasing synaptic transmission reliability and promoting synaptic plasticity (Lisman, 1997). In addition to propensity for bursts, AP firing patterns differ with respect to the stability of spike frequency in response to extended depolarization; while some neurons maintain a constant firing rate, others show spike frequency adaptation or acceleration (Connors and Gutnick, 1990; Miller et al., 2008).

Important experimental considerations

The complexity of my final classification approach (i.e. twelve total classifiers) was driven in part by insufficient data collection in the early experimental stages. The assumption that D1+ and D3+ neurons would be discriminable by sag and rebound properties alone led to our incomplete dataset regarding AP firing properties. This result highlights the importance of probing as many parameters as possible from the beginning, regardless of initial hypothesis.

The second source of classification complexity derived from experimental demands: for Ca imaging experiments, Fluo5 replaced EGTA in the internal solution. This change in Ca buffer affected both AP waveform and spike train properties. AP-evoked Ca influx promotes AP repolarization through coupling to Ca-activated potassium channels (Bean, 2007). I found that APs recording with EGTA, a much higher-affinity Ca buffer than Fluo5, paradoxically led to narrower APs, the reverse of what would be expected from an increase in bound Ca (and therefore a decrease in available Ca). The reasons for this result are unclear, but regardless this necessitated

separate classification of D1+ and D3+ pyramidal neurons based on recording condition.

D1+ and D3+ neurons: electrophysiologically-distinct IT cell types

Extensive prior work has focused on the separation between IT, cortically-projecting, and PT, subcortically-projecting, neocortical pyramidal neurons with respect to both subthreshold and suprathreshold electrophysiological properties. AP waveform, firing pattern, and h-current have been found to strongly correlate with pyramidal neuron projection class (Harris and Shepherd, 2015). Specifically, PT neurons have narrow APs and maintain stable AP frequencies during repetitive firing, while IT neurons have wide APs and exhibit strong spike frequency adaptation. In addition, PT and IT neurons exhibit high and low sag and rebound responses, respectively, indicative of varying degrees of h-current (Hattox and Nelson, 2007; Dembrow et al., 2010; Gee et al., 2012; Oswald et al., 2013; Suter et al., 2013).

However, cortically-projecting pyramidal neurons are themselves heterogeneous (Otsuka and Kawaguchi, 2011), as further revealed here through an in depth analysis of D1+ and D3+ IT neuron electrophysiological properties. By inspecting the linear discriminant model developed in Chapter 2, I determined that spiking properties were the most important features for successful prediction of D1R- and D3R-expression, in contrast to the sharp separation between PT and IT neurons with respect to sag and rebound properties. Indeed, a linear discriminant classifier based solely on AP waveform and firing properties performed nearly as well as one including sag and rebound (Fig. 45). Whether this newfound information could be applied to distinguishing

pyramidal neuron prefrontal subtypes by their waveform *in vivo* (as has been used to distinguish pyramidal neurons and interneurons) would be worth further study.

Figures

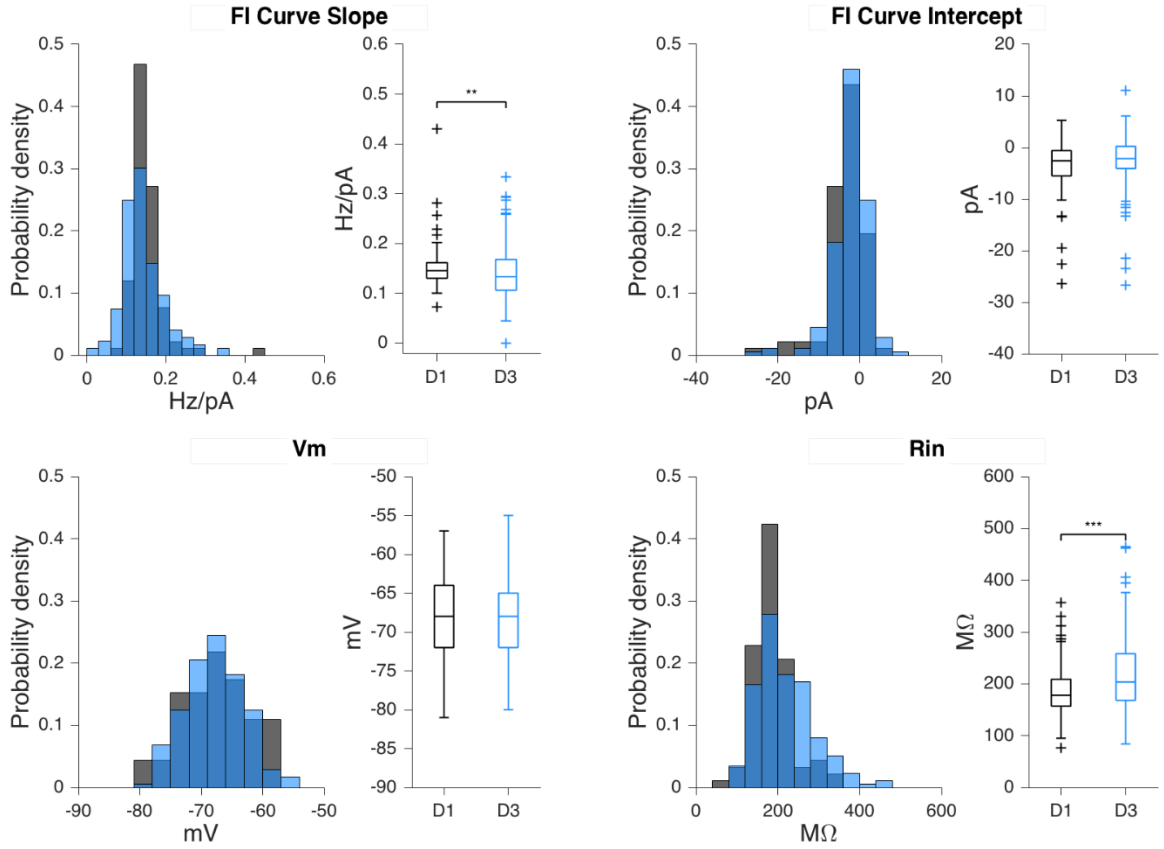

Figure 24. Baseline variables and FI curve variables for D1+ and D3+ pyramidal cell classes

In Figs. 24-36, both histograms and boxplots compare AP spike train or waveform electrophysiological properties for D1+ (black) and D3+ (blue) pyramidal neurons. Boxplots are median, 25th (Q1), and 75th (Q3) percentiles; whiskers extend to all data points that are not outliers. Outliers are defined as Q3 + 1.5*(Q3–Q1) and Q1–1.5*(Q3–Q1). Wilcoxon's rank-sum test, * $p < 0.05$, ** $p < 0.01$, *** $p < 0.001$

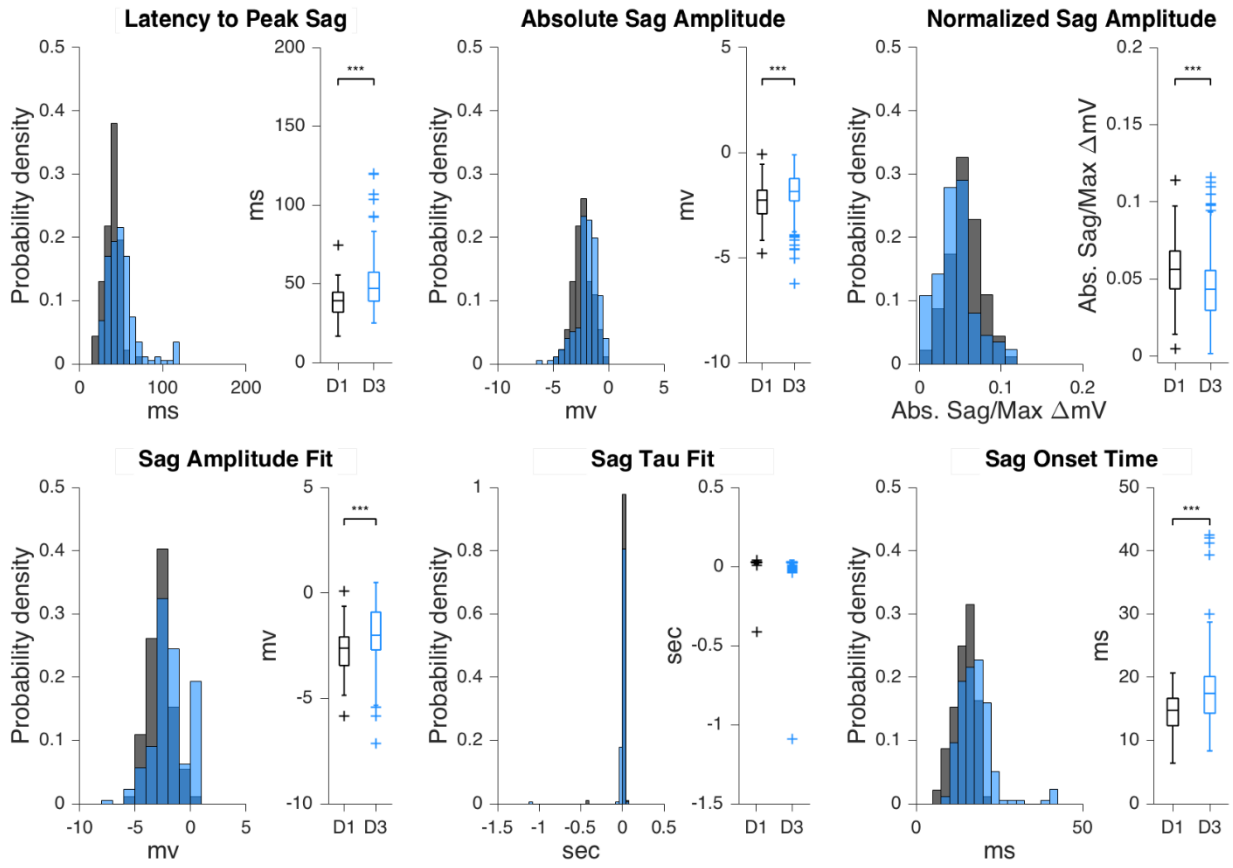

Figure 25. Sag variables for D1+ and D3+ pyramidal cell classes

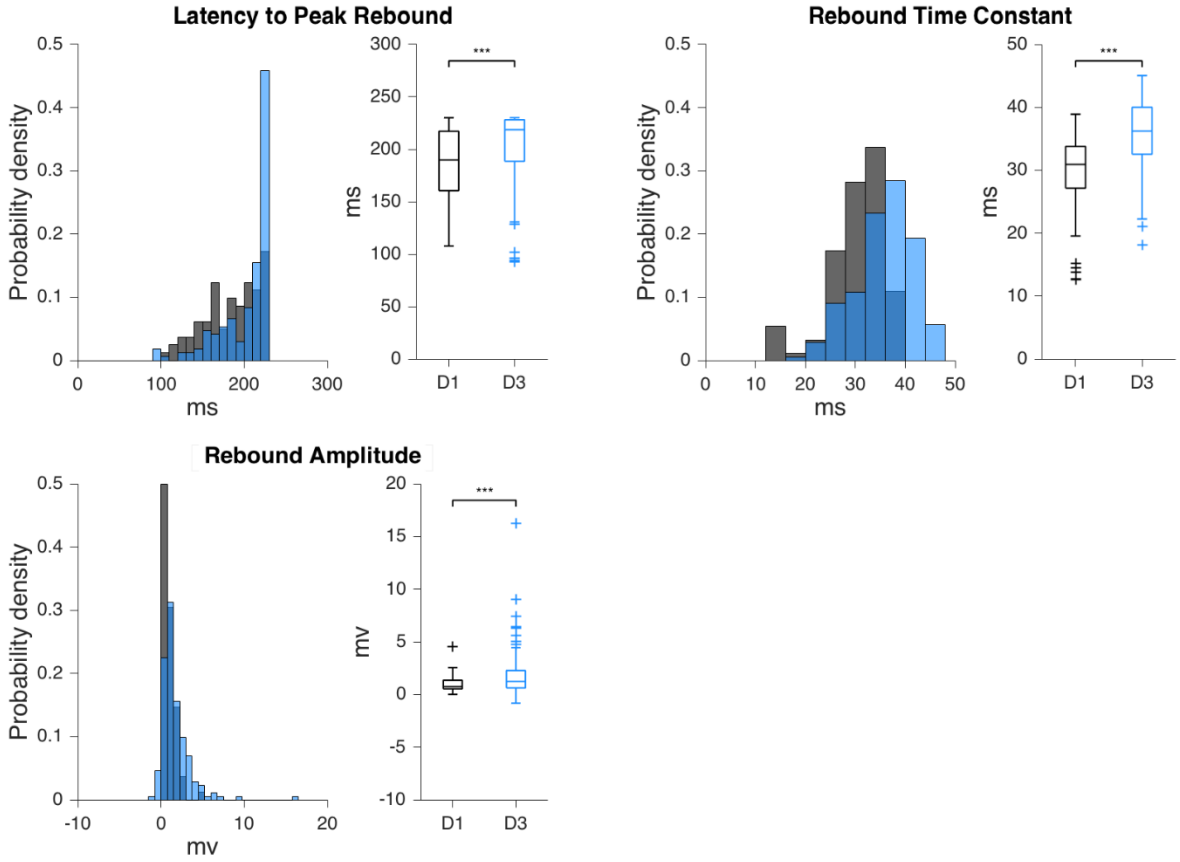

Figure 26. Rebound variables for D1+ and D3+ pyramidal cell classes
Both latency to peak rebound and rebound amplitude were calculated within 230 ms of current offset.

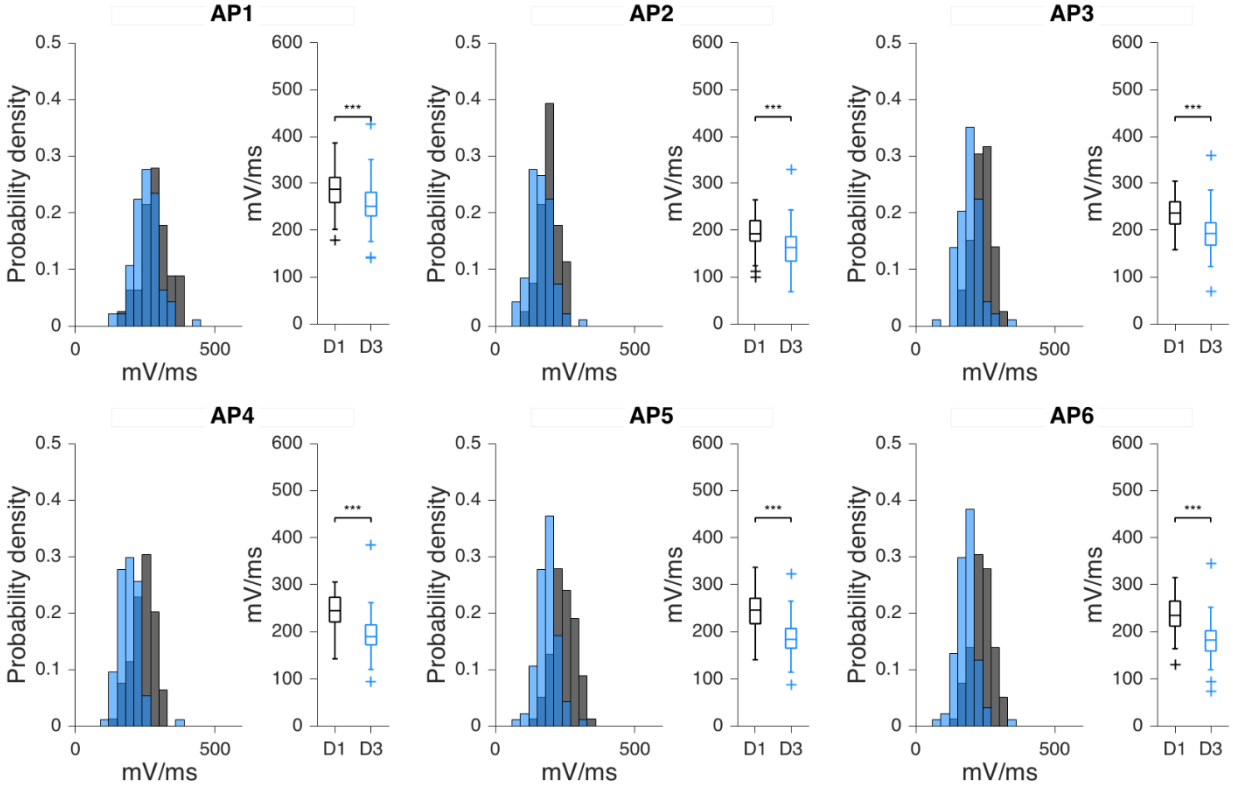

Figure 27. AP rate of rise for D1+ and D3+ pyramidal cell classes.
For Figs. 27-36 data shown for 6 AP spike trains.

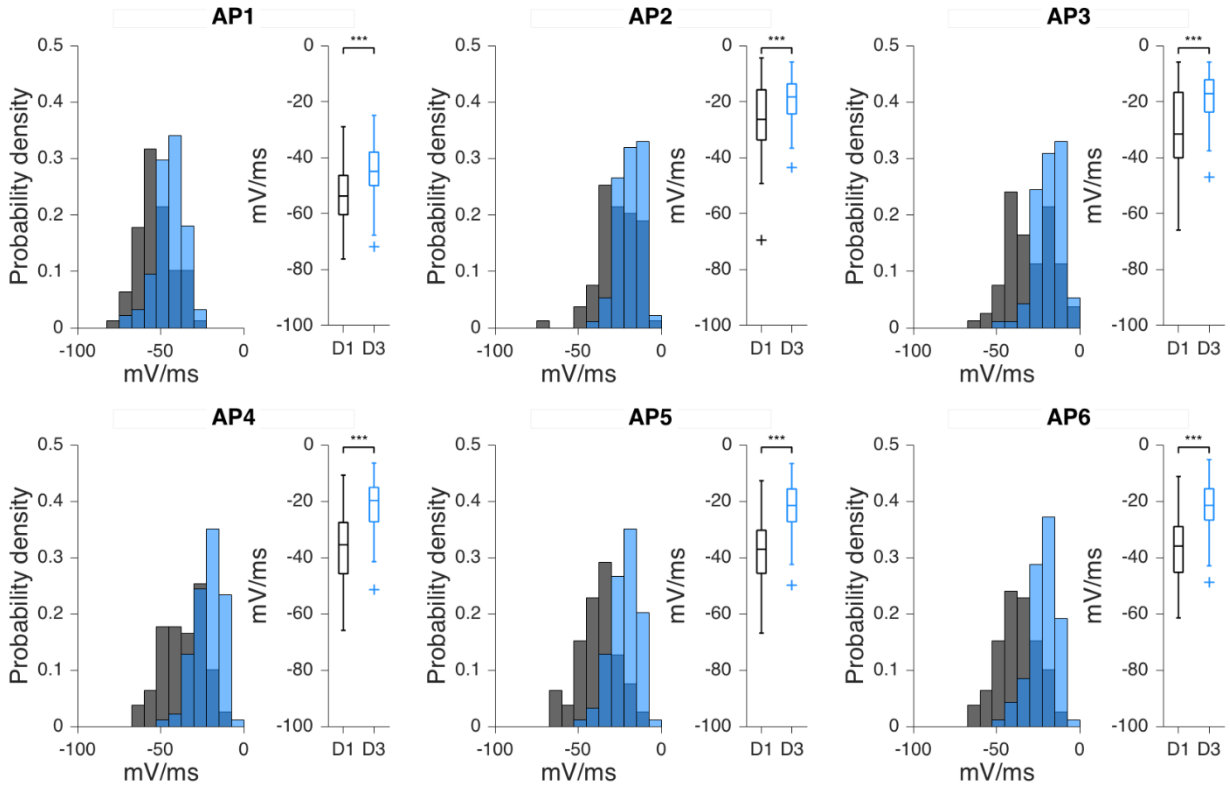

Figure 28. AP rate of fall for D1+ and D3+ pyramidal cell classes.

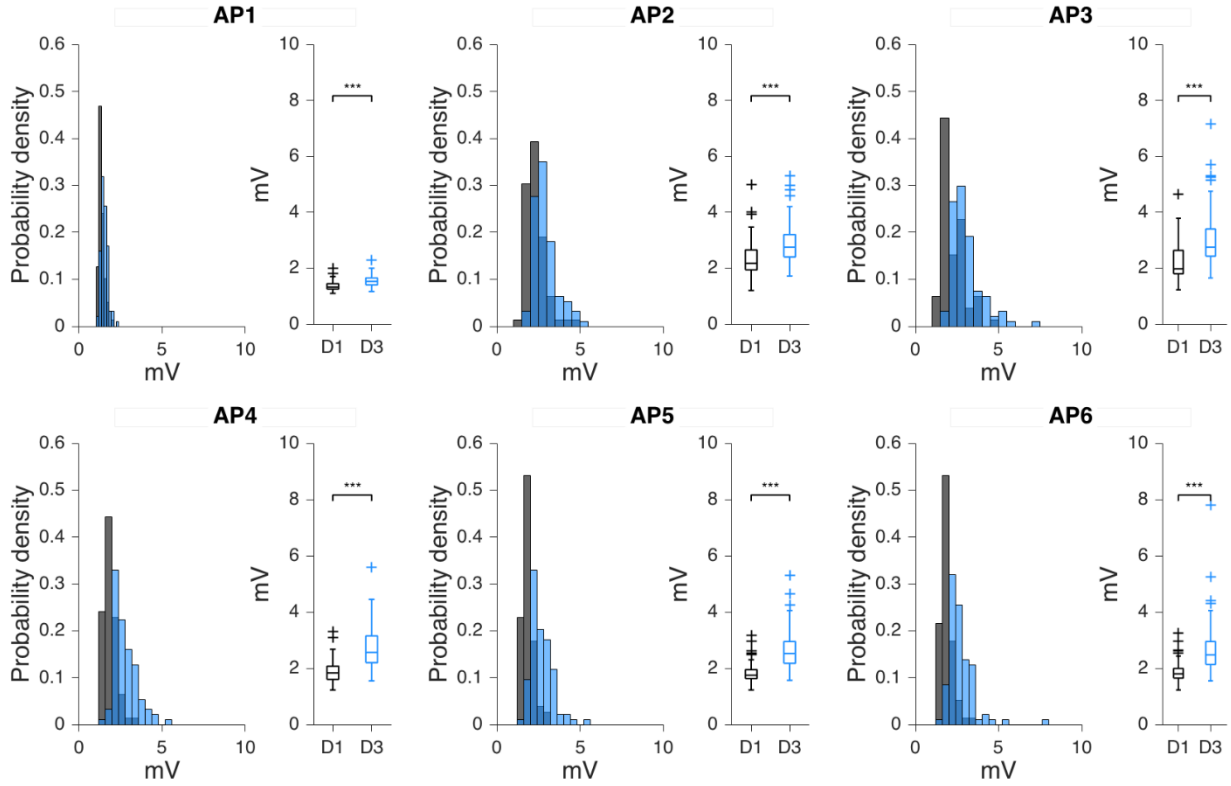

Figure 29. AP spike width distributions for D1+ and D3+ pyramidal cell classes.

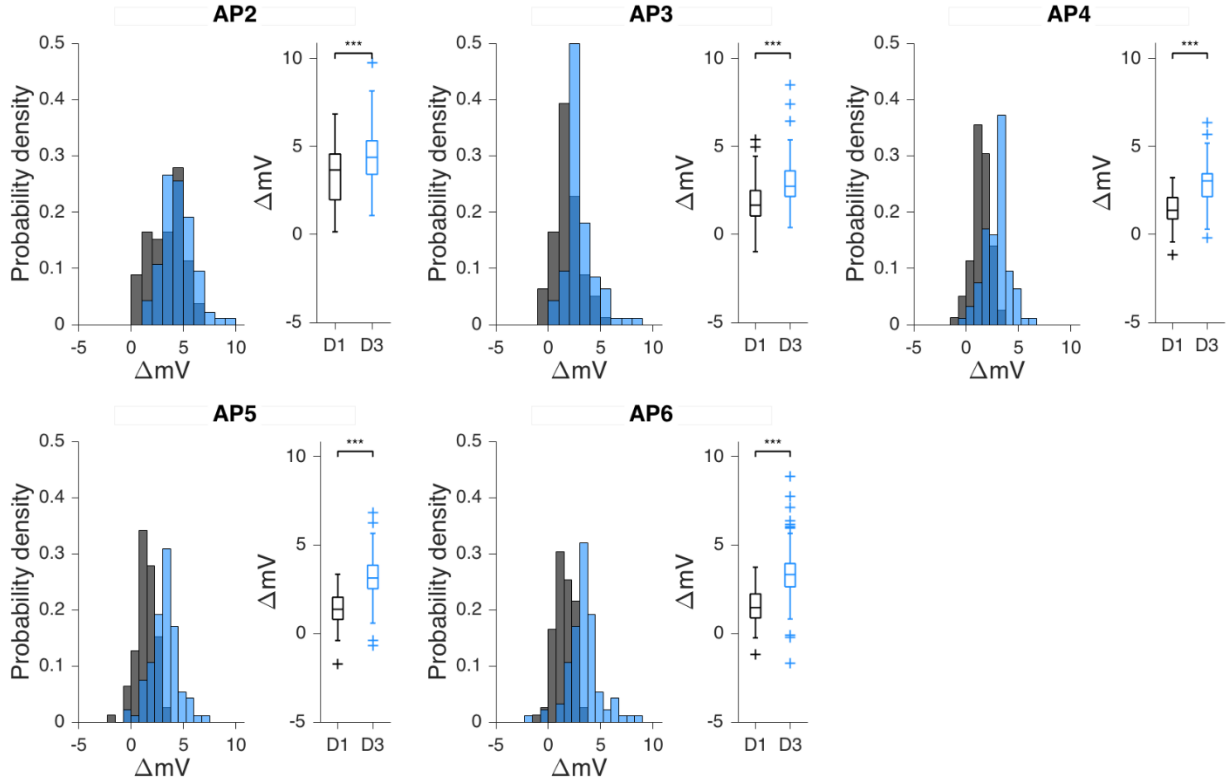

Figure 30. Changes in AP threshold (compared to AP1) throughout spike trains for D1+ and D3+ pyramidal cell classes.

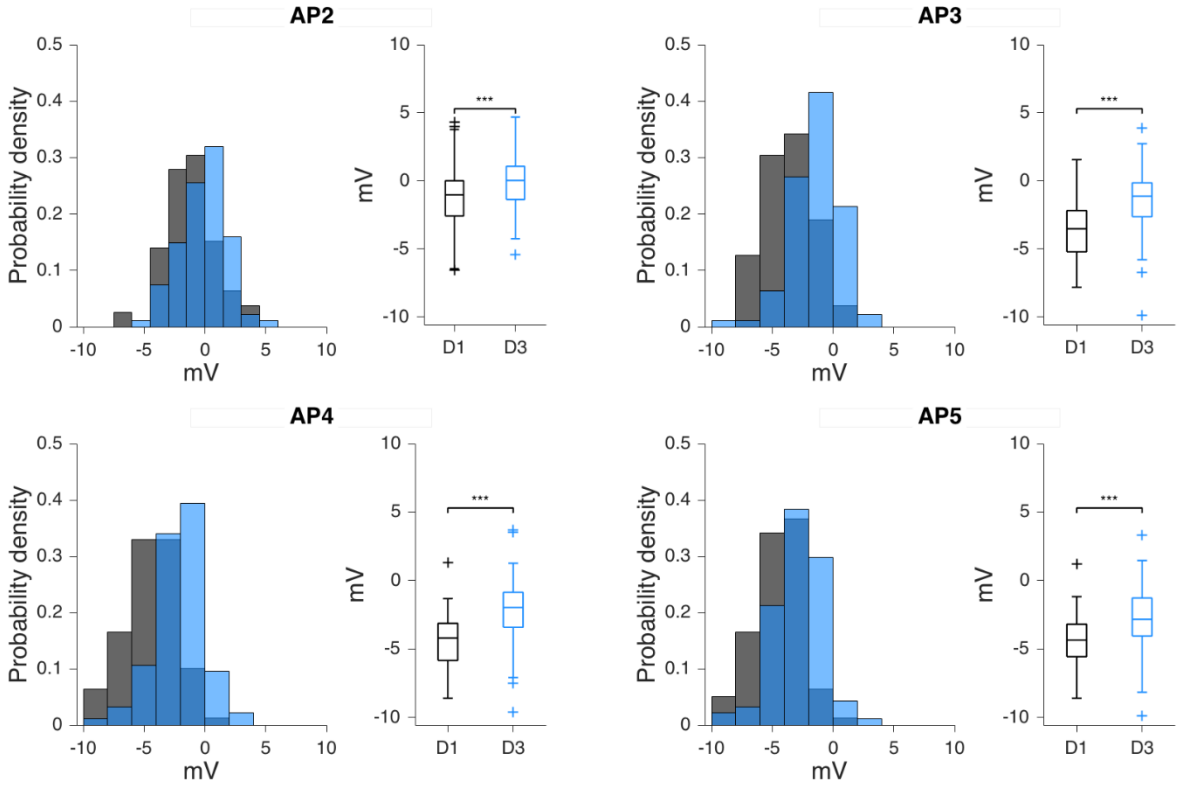

Figure 31. Change in AHP (compared to AP1) throughout a spike train for D1+ and D3+ pyramidal cell classes

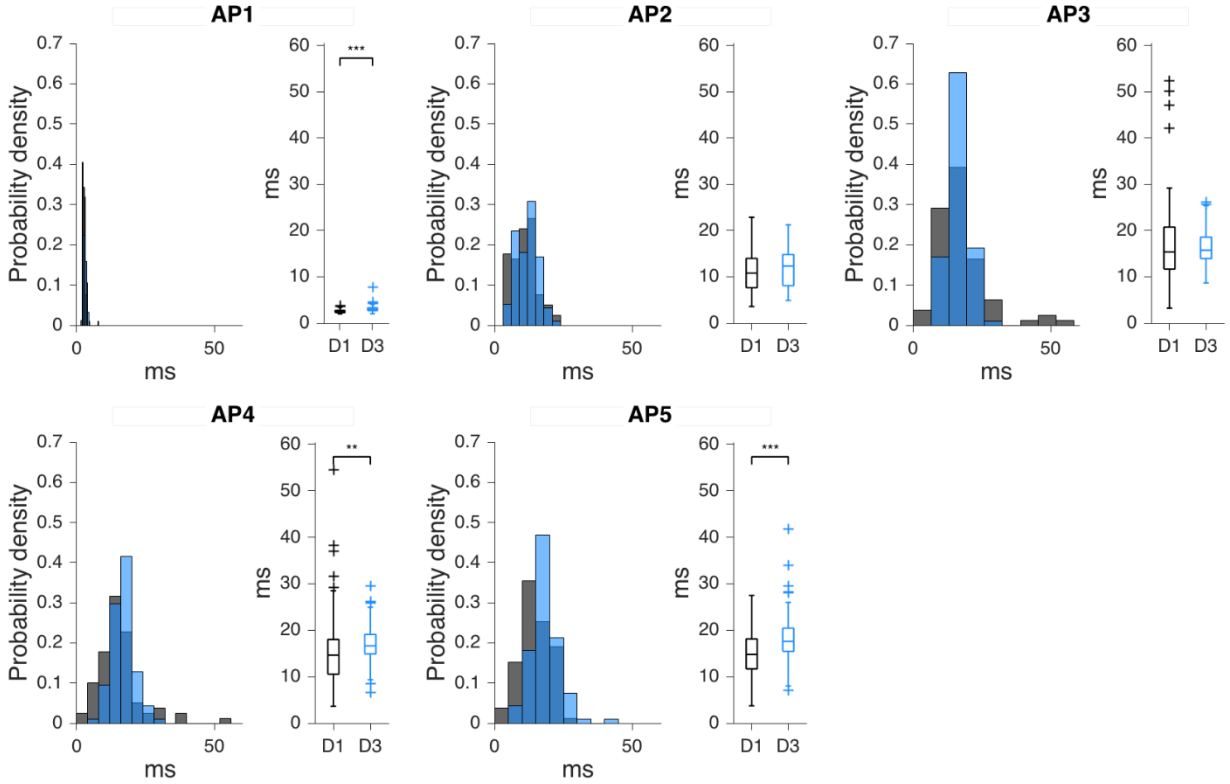

Figure 32. AHP timing relative to timing of AP peak for D1+ and D3+ pyramidal cell classes

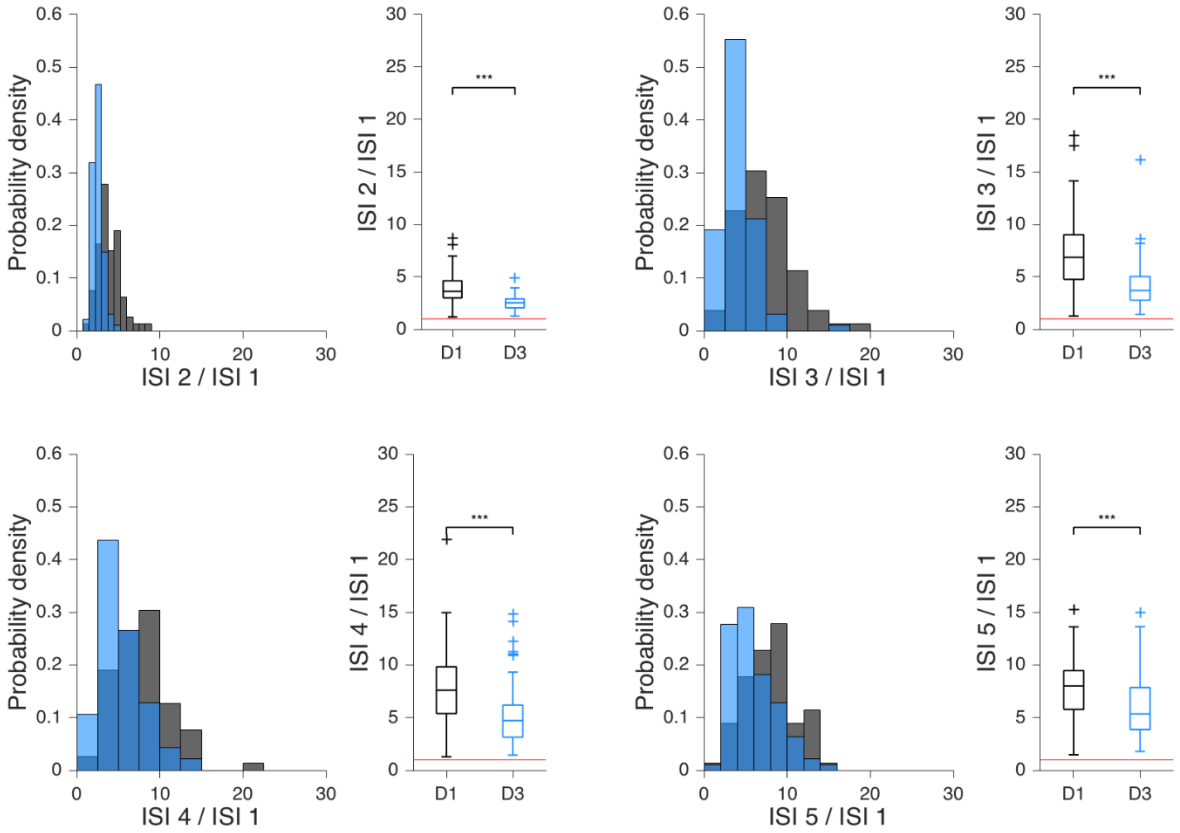

Figure 33. ISI ratios relative to ISI 1 for D1+ and D3+ pyramidal cell classes ("adaptation ratio 1")

Red horizontal line indicates a ratio of 1.

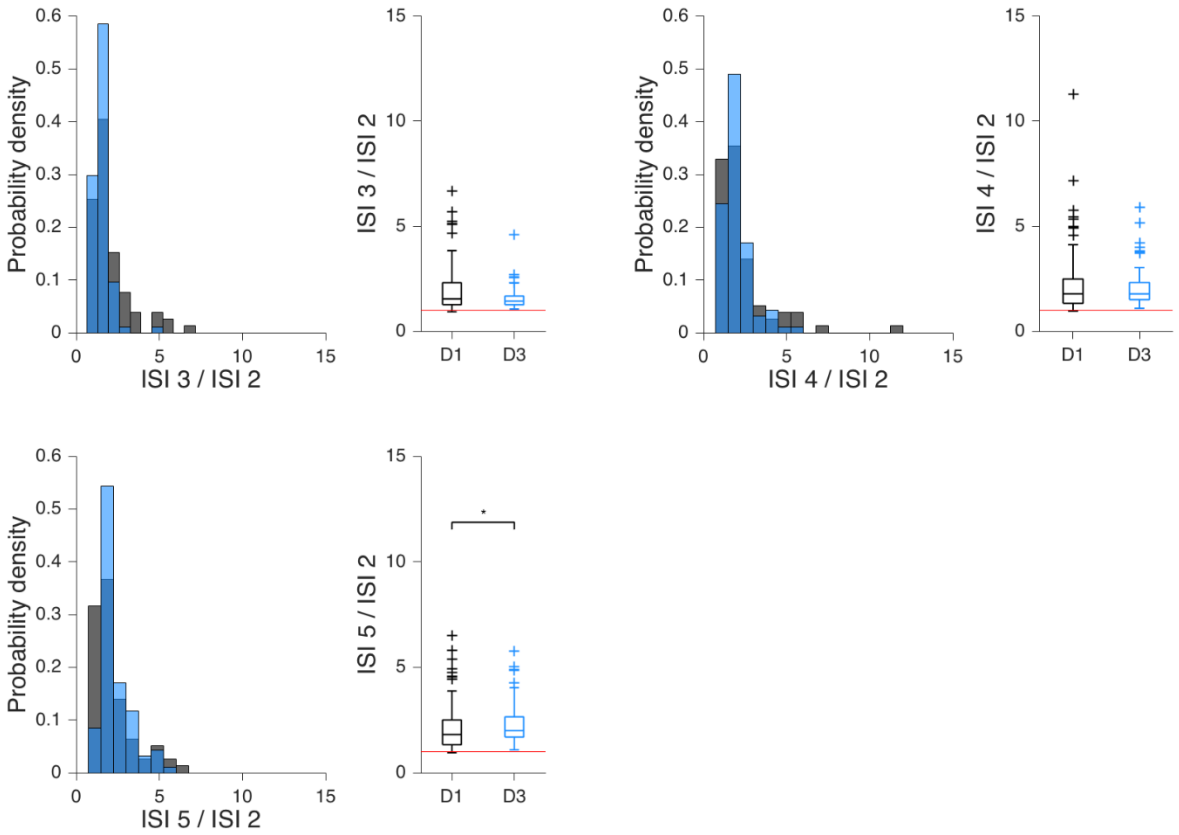

Figure 34. ISI ratios relative to ISI 2 for D1+ and D3+ pyramidal cell classes ("adaptation ratio 2")

Red horizontal line indicates a ratio of 1.

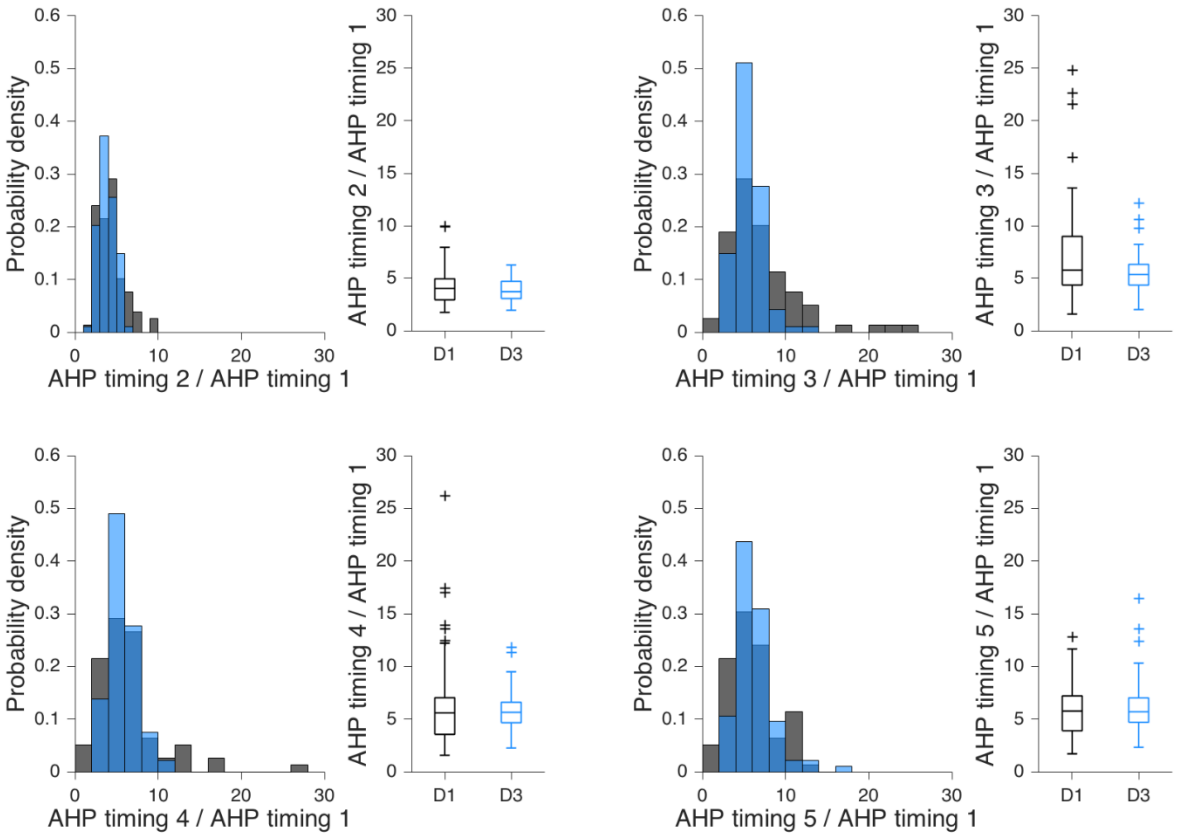

Figure 35. AHP timing ratios relative to AHP timing 1 for D1+ and D3+ pyramidal cell classes ("AHP timing ratio 1")

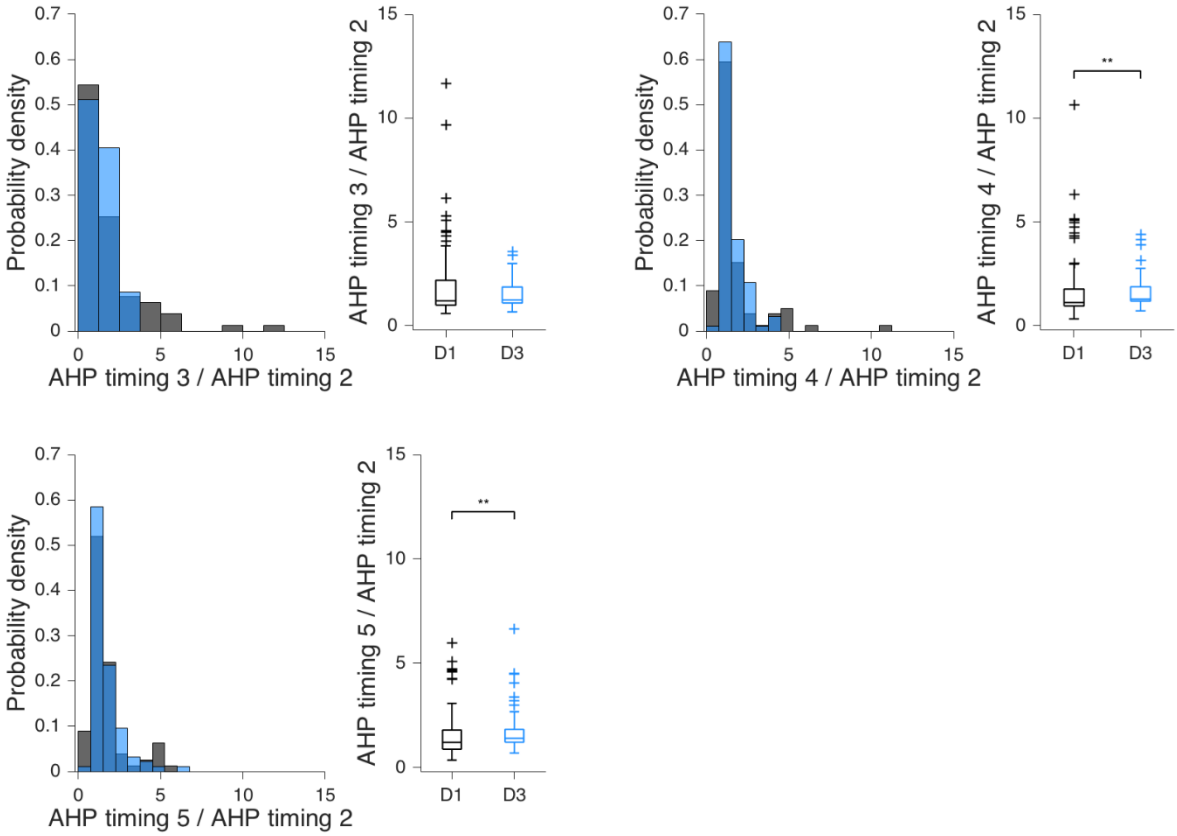

Figure 36. AHP timing ratios relative to AHP timing 2 for D1+ and D3+ pyramidal cell classes ("AHP timing ratio 2")

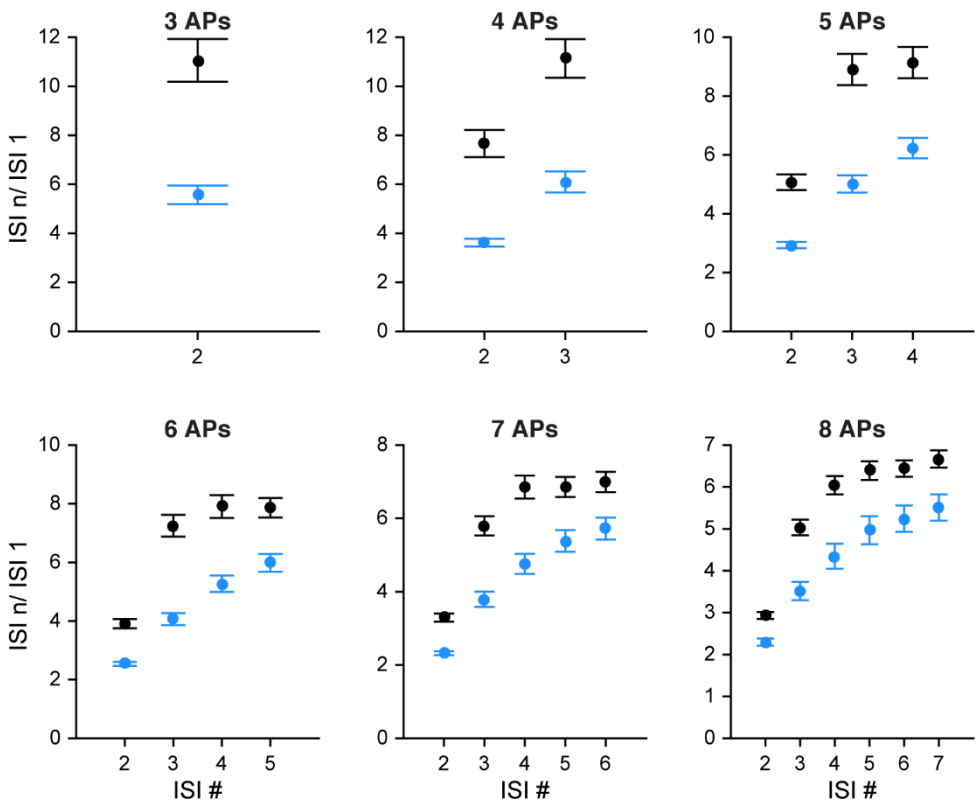

Figure 37. Spike frequency adaptation for D1+ and D3+ cell classes, across AP firing frequencies (APs/300 ms)

ISI ratios relative to ISI 1 for D1+ (black) and D3+ (blue) cell classes for all later ISIs in a spike train. Data for 6 APs same as that in Fig. 33**.** Error bars indicate mean ± SEM.

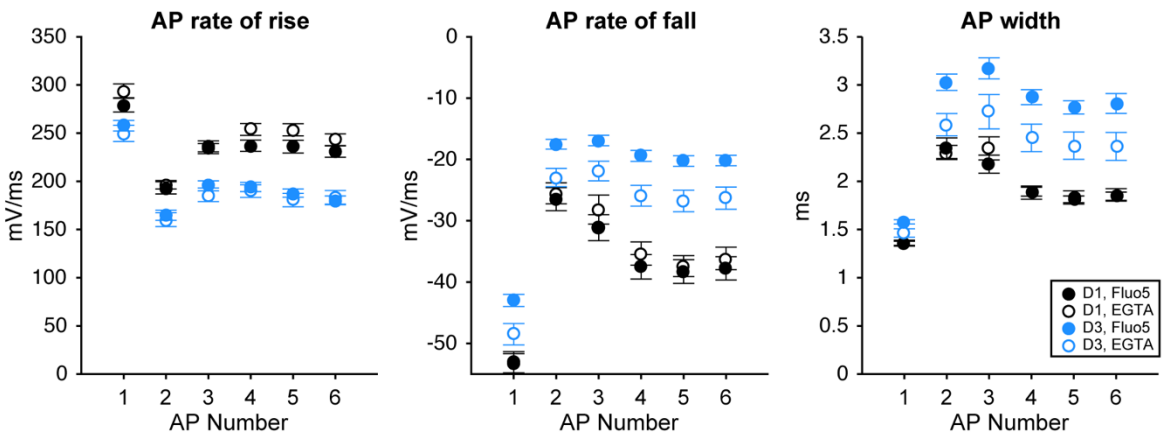

Figure 38. Ca buffer (EGTA vs. Fluo5) alters AP waveform
Error bars indicate mean ± SEM.

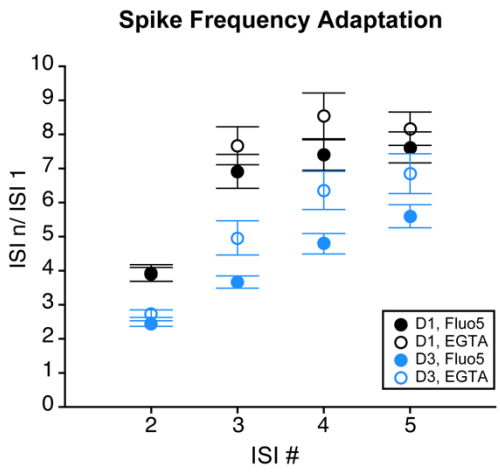

Figure 39. Ca buffer (EGTA vs. Fluo5) alters spike frequency adaptation.
Error bars indicate mean ± SEM.

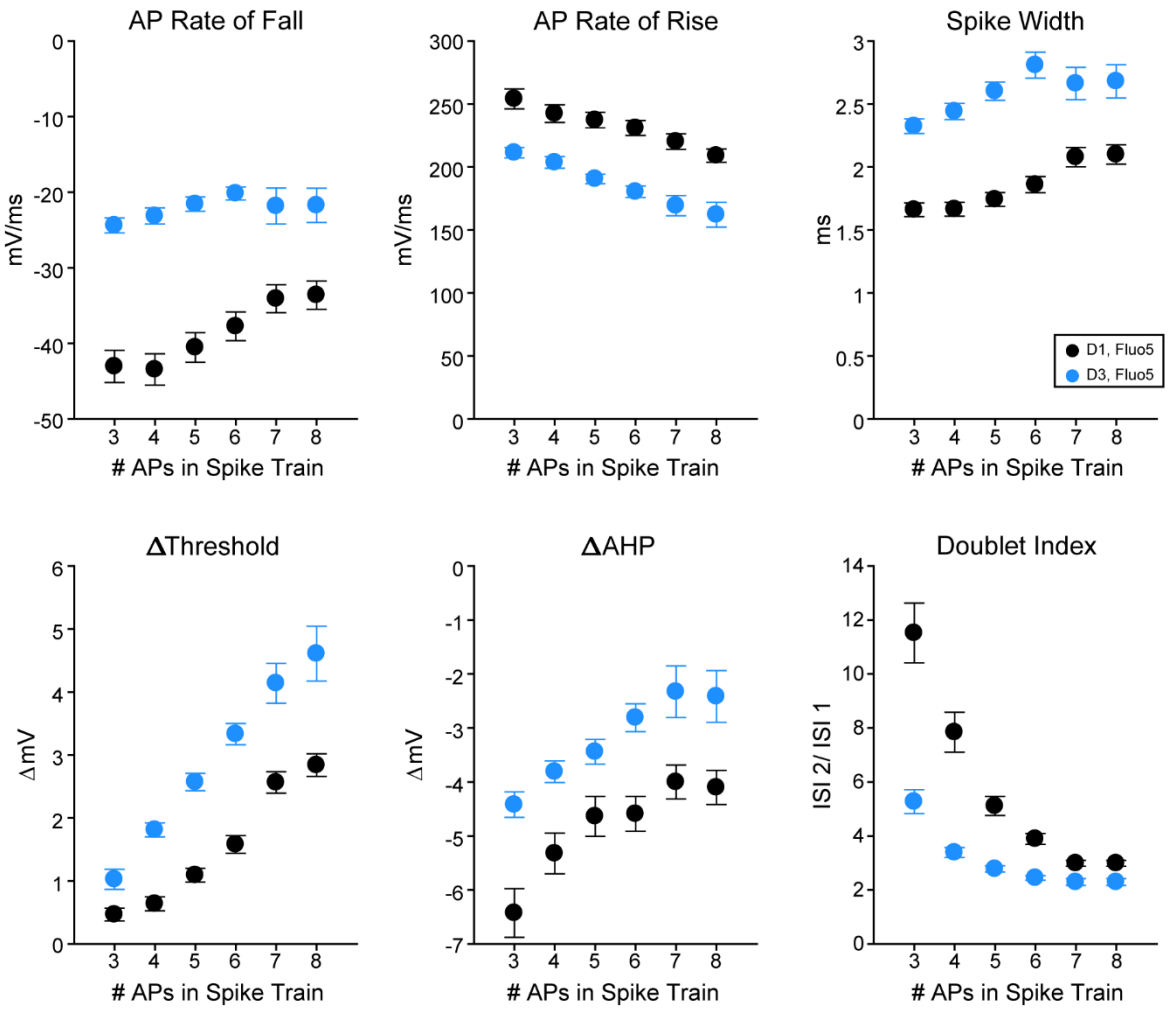

Figure 40. Number of APs in spike train affects spiking variables
All spike trains were generated by 300 ms depolarizing square current pulse; data show D1+ (black) and D3+ (blue) electrophysiological measurements with respect to number of APs in a given spike train (all data in Fluo5 recording condition). Error bars indicate mean ± SEM.

AP spike shape variables (AP rate of fall, AP rate of rise, and spike width) are measurements for the last AP in each spike train. ΔThreshold is the threshold of the last AP minus that of the first AP, while ΔAHP is the AHP of the second to last AP minus that of the first AP. Doublet index is the ratio of the second ISI to the first ISI.

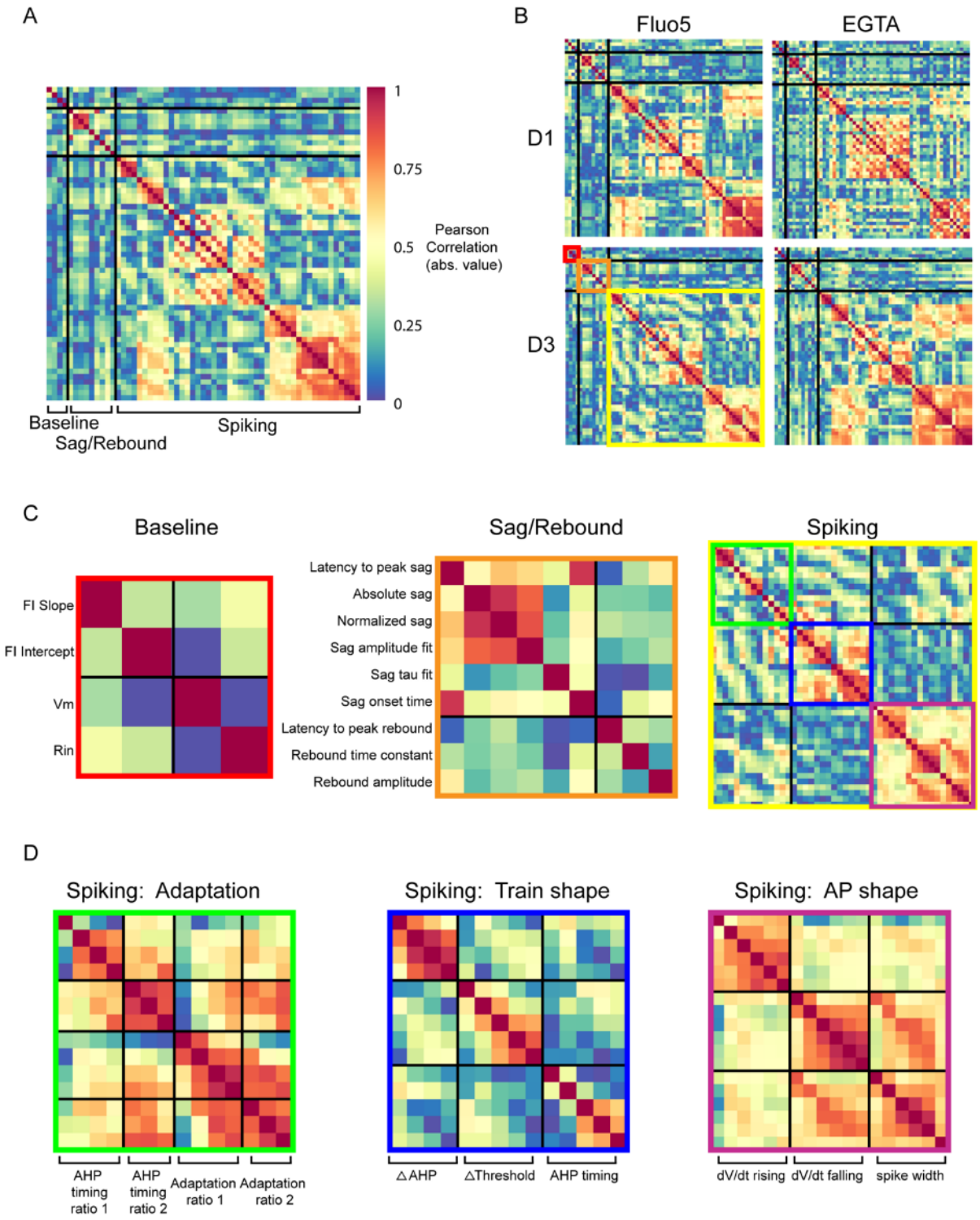

Figure 41. Strong pairwise correlations between electrophysiological variables

(A) Correlation matrix heat map of all electrophysiological variables measured for cells with 6 AP spike trains. Colors represent the absolute value of the Pearson correlation (|r|), which ranges from 0 (no correlation) to 1 (perfectly correlated). Black lines distinguish major

variable groups (baseline, sag/rebound, and spiking). Colorbar to right; color scale same for B-D.

(B) Correlation matrix heat maps for D1+ and D3+ neuron populations, separated by Ca buffer in internal solution (EGTA or Fluo5). Same variables as in A.

(C) Baseline, sag/rebound, and spiking variable correlation heat maps for D3+ neurons (Fluo5 recording condition) (from highlighted boxes in B)

(D) Enlargement of highlighted boxes in C, showing three major groupings of spiking variables: adaptation, train shape, and AP shape. For each spiking variable, data shown in order of AP number from left to right (e.g. dV/dt rising AP1, AP2, …AP6).

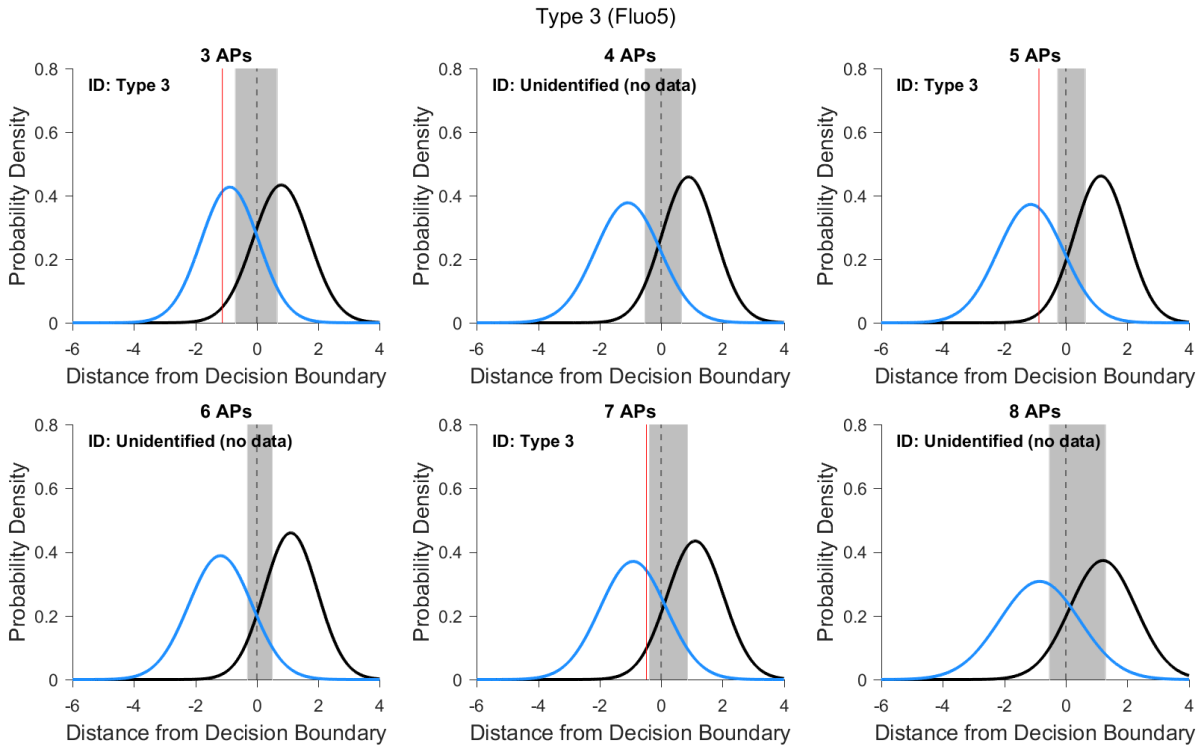

Figure 42. Linear discriminant classifier applied to non-genetically identified cell (Fluo5 in the internal solution)

Visualization of all linear discriminant classifiers (3-8 APs) for Fluo5 in the internal solution. D1+ (black) and D3+ (blue) cells' distances from the discriminant decision boundary (grey dashed line) were fit by normal distributions. These distributions defined the "exclusion zone," the area near the discriminant where cell classes were imperfectly separated and therefore "unidentified" (see Chapter 2, Materials and Methods). Red line shows distance from decision boundary for genetically un-identified cell across all relevant classifiers.

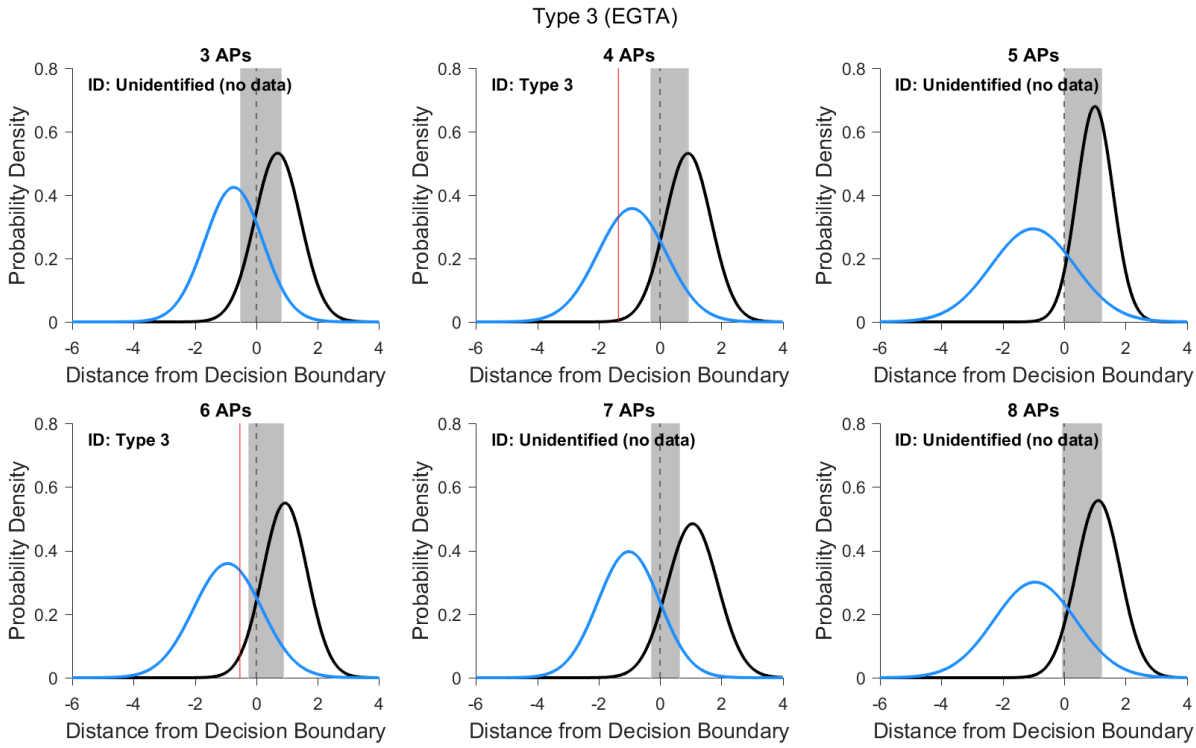

Figure 43. Linear discriminant classifier applied to non-genetically identified cell (EGTA in the internal solution)

Same as Fig. 42, except example cell with EGTA in the internal.

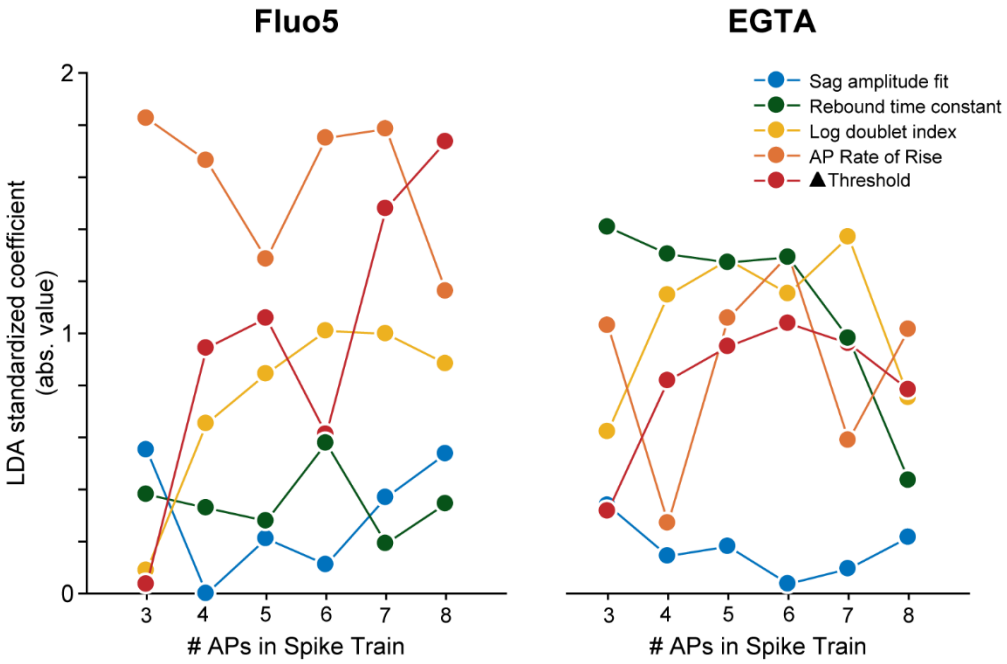

Figure 44. LDA standardized coefficients across all 12 classifiers
LDA standardized coefficients for Fluo5 (left) and EGTA (right) classifiers for 3 to 8 APs in spike train (300 ms current pulse). Values taken from Table 1.

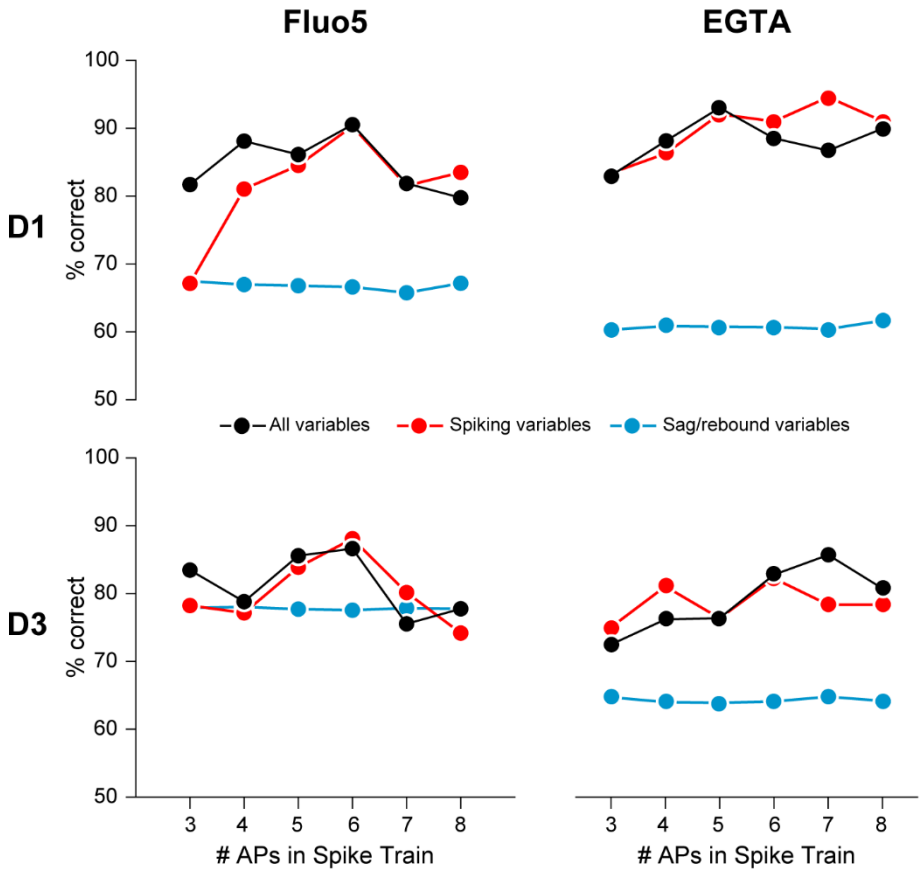

Figure 45. Cross-validation across all classifiers demonstrates the critical contribution of spiking variables to classification accuracy.
Cross-validation values for the “all variables” condition same as Fig. 2E (left); repeated holdout cross-validation additionally performed for the spiking variable subset and sag/rebound variable subset.

Tables

		D1+	D3+	Non-labelled
Ca Buffer	EGTA	40	50	39
	Fluo5	52	126	85
Total		92	176	124

Table 4. Number of neurons from each experimental condition, including both genetically-labelled and unlabeled populations.

# APs per 300 ms	D1+ (n = 92)	D3+ (n = 176)	Non-labelled (n = 124)
3	81	117	61
4	81	111	61
5	82	103	44
6	79	94	38
7	80	60	26
8	74	29	18

Table 5. Number of D1+/D3+/non-labelled neurons that have data across range of firing frequencies.

References

Armañanzas, R., and Ascoli, G.A. (2015). Towards the automatic classification of neurons. Trends Neurosci. *38*, 307–318.

Bean, B.P. (2007). The action potential in mammalian central neurons. Nat. Rev. Neurosci. *8*, 451–465.

Bischofberger, J., Geiger, J.R.P., and Jonas, P. (2002). Timing and efficacy of Ca2+ channel activation in hippocampal mossy fiber boutons. J. Neurosci. *22*, 10593–10602.

Borst, J.G.G., and Sakmann, B. (1999). Effect of changes in action potential shape on calcium currents and transmitter release in a calyx-type synapse of the rat auditory brainstem. Philos. Trans. R. Soc. B Biol. Sci. *354*, 347–355.

Cauli, B., Porter, J.T., Tsuzuki, K., Lambolez, B., Rossier, J., Quenet, B., and Audinat, E. (2000). Classification of fusiform neocortical interneurons based on unsupervised clustering. Proc. Natl. Acad. Sci. U. S. A. *97*, 6144–6149.

Connors, B.W., and Gutnick, M.J. (1990). Intrinsic firing patterns of diverse neocortical neurons. Trends Neurosci. *13*, 99–104.

DeFelipe, J. (2002). Cortical interneurons: From Cajal to 2001. Prog. Brain Res. *136*, 215–238.

DeFelipe, J. (2013). Cajal and the discovery of a new artistic world: The neuronal forest. Prog. Brain Res. *203*, 201–220.

Dembrow, N.C., Chitwood, R.A., and Johnston, D. (2010). Projection-specific neuromodulation of medial prefrontal cortex neurons. J Neurosci *30*, 16922–16937.

Fisher, R.A. (1938). The statistical utilization of mulitiple measurements. Ann. Eugen. *8*, 376–386.

Gee, S., Ellwood, I., Patel, T., Luongo, F., Deisseroth, K., and Sohal, V.S. (2012). Synaptic activity unmasks dopamine D2 receptor modulation of a specific class of layer V pyramidal neurons in prefrontal cortex. J. Neurosci. *32*, 4959–4971.

Guerra, L., McGarry, L.M., Robles, V., Bielza, C., Larrañaga, P., and Yuste, R. (2011). Comparison between supervised and unsupervised classifications of neuronal cell types: a case study. Dev. Neurobiol. *71*, 71–82.

Harris, K.D., and Shepherd, G.M.G. (2015). The neocortical circuit: themes and variations. Nat. Neurosci. *18*, 170–181.

Hattox, A.M., and Nelson, S.B. (2007). Layer V neurons in mouse cortex projecting to different targets have distinct physiological properties. J. Neurophysiol. *98*, 3330–3340.

Helmstaedter, M., Sakmann, B., and Feldmeyer, D. (2009). The relation between dendritic geometry, electrical excitability, and axonal projections of L2/3 interneurons in rat barrel cortex. Cereb. Cortex *19*, 938–950.

Henze, D.A., Borhegyi, Z., Csicsvari, J., Mamiya, A., Harris, K.D., and Buzsáki, G. (2000). Intracellular features predicted by extracellular recordings in the hippocampus in vivo. J. Neurophysiol. *84*, 390–400.

Kalmbach, B.E., Chitwood, R.A., Dembrow, N.C., and Johnston, D. (2013). Dendritic Generation of mGluR-Mediated Slow Afterdepolarization in Layer 5 Neurons of Prefrontal Cortex. J. Neurosci. *33*, 13518–13532.

Karagiannis, A., Gallopin, T., David, C., Battaglia, D., Geoffroy, H., Rossier, J., Hillman, E.M.C., Staiger, J.F., and Cauli, B. (2009). Classification of NPY-Expressing Neocortical Interneurons. J. Neurosci. *29*, 3642–3659.

Karube, F., Kubota, Y., and Kawaguchi, Y. (2004). Axon Branching and Synaptic Bouton Phenotypes in GABAergic Nonpyramidal Cell Subtypes. J. Neurosci. *24*, 2853–2865.

Klausberger, T., Magill, P.J., Cobden, P.M., and Somogyi, P. (2003). Firing of Hippocampal Interneurons in Vivo. Nature *421*, 844–848.

Kole, M.H.P., Letzkus, J.J., and Stuart, G.J. (2007). Axon Initial Segment Kv1 Channels Control Axonal Action Potential Waveform and Synaptic Efficacy. Neuron *55*, 633–647.

Lammel, S., Hetzel, A., Häckel, O., Jones, I., Liss, B., and Roeper, J. (2008). Unique Properties of Mesoprefrontal Neurons within a Dual Mesocorticolimbic Dopamine System. Neuron *57*, 760–773.

Li, T., Zhu, S., and Ogihara, M. (2006). Using discriminant analysis for multi-class classification: An experimental investigation. Knowl. Inf. Syst. *10*, 453–472.

Lisman, J.E. (1997). Bursts as a unit of neural information: making unreliable synapses reliable. Trends Neurosci. *20*, 38–43.

López-Muñoz, F., Boya, J., and Alamo, C. (2006). Neuron theory, the cornerstone of neuroscience, on the centenary of the Nobel Prize award to Santiago Ramón y Cajal. Brain Res. Bull. *70*, 391–405.

Margolis, E.B., Mitchell, J.M., Ishikawa, J., Hjelmstad, G.O., and Fields, H.L. (2008). Midbrain dopamine neurons: projection target determines action potential duration and dopamine D(2) receptor inhibition. J Neurosci *28*, 8908–8913.

McCormick, D. A., Connors, B.W., Lighthall, J.W., and Prince, D. A. (1985). Comparative electrophysiology of pyramidal and sparsely spiny stellate neurons of the neocortex. J. Neurophysiol. *54*, 782–806.

McGarry, L.M., Packer, A.M., Fino, E., Nikolenko, V., Sippy, T., and Yuste, R. (2010). Quantitative classification of somatostatin-positive neocortical interneurons identifies three interneuron subtypes. Front. Neural Circuits *4*, 12.

Miller, M.N., Okaty, B.W., and Nelson, S.B. (2008). Region-specific spike-frequency acceleration in layer 5 pyramidal neurons mediated by Kv1 subunits. J. Neurosci. *28*, 13716–13726.

Oswald, M.J., Tantirigama, M.L.S., Sonntag, I., Hughes, S.M., and Empson, R.M. (2013). Diversity of layer 5 projection neurons in the mouse motor cortex. Front. Cell. Neurosci. *7*, 174.

Otsuka, T., and Kawaguchi, Y. (2011). Cell diversity and connection specificity between callosal projection neurons in the frontal cortex. J. Neurosci. *31*, 3862–3870.

Seong, H.J., and Carter, A.G. (2012). D1 receptor modulation of action potential firing in a subpopulation of layer 5 pyramidal neurons in the prefrontal cortex. J. Neurosci. *32*, 10516–10521.

Shah, M.M. (2014). Cortical HCN channels: function, trafficking and plasticity. J. Physiol. *592*, 2711–2719.

Sheets, P.L., Suter, B.A., Kiritani, T., Chan, C.S., Surmeier, D.J., and Shepherd, G.M.G. (2011). Corticospinal-specific HCN expression in mouse motor cortex: Ih-dependent synaptic integration as a candidate microcircuit mechanism involved in motor control. J. Neurophysiol. *106*, 2216–2231.

Suter, B.A., Migliore, M., and Shepherd, G.M.G. (2013). Intrinsic electrophysiology of mouse corticospinal neurons: A class-specific triad of spike-related properties. Cereb. Cortex *23*, 1965–1977.

Vasques, X., Vanel, L., Villette, G., and Cif, L. (2016). Morphological Neuron Classification Using Machine Learning. Front. Neuroanat. *10*, 1–12.

Zaitsev, A. V., Povysheva, N. V., Gonzalez-Burgos, G., and Lewis, D.A. (2012). Electrophysiological classes of layers 2-3 pyramidal cells in monkey prefrontal cortex. J. Neurophysiol. 595–609.

Chapter 5

Concluding Remarks

The studies presented here reveal a novel role for dopamine D3 receptor (D3R)-signaling in prefrontal cells and circuits, establishing a framework for probing the mechanisms of D3R impacts on prefrontal-dependent cognitive function and dysfunction. I find that within the medial prefrontal cortex (mPFC), D3Rs selectively regulate neuronal excitability within a novel subtype of prefrontal projection neuron, modulating these neurons' propensity for high frequency action potential (AP) bursts, thought to play a unique role in prefrontal information processing. The results of each chapter have been discussed individually; therefore, in this chapter, I will consider remaining questions regarding these findings, with a focus on larger implications and future directions.

Direct control of neuronal output via site of AP initiation

Recent studies of axonal physiology have revealed that the axon has a more prominent role in neuronal integration and plasticity than previously appreciated (reviewed in Grubb et al., 2011; Bender and Trussell, 2012; Kole and Stuart, 2012; Yamada and Kuba, 2016). The axon initial segment (AIS) integrates graded synaptic inputs, transforming them into APs; direct modulation of the AIS therefore provides a powerful means of controlling neuronal output. For example, structural alterations in AIS length and location, occurring on both rapid and extended timescales, homeostatically regulate neuronal excitability (Grubb and Burrone, 2010; Kuba et al., 2010; Evans et al., 2015; Wefelmeyer et al., 2015). In addition, ionotropic modulation of AIS function can

occur at sub-second timescales, with both AP generation and waveform influenced by voltage-gated sodium (Hu et al., 2009), potassium (Kole et al., 2007; Shu et al., 2007), and calcium (Bender and Trussell, 2009; Bender et al., 2012) channels localized to the AIS. Axonal ion channels are also targets of neuromodulators such as acetylcholine (Martinello et al., 2015), serotonin (Cotel et al., 2013; Ko et al., 2016), and dopamine (Bender et al., 2010), providing a mechanistic link between neuromodulatory control of cognitive and emotional processing and neuronal function throughout the brain.

Here, we find that dopamine acts via D3Rs to downregulate AIS Ca in mPFC, extending observations previously made in brainstem interneurons (Bender et al., 2010), and demonstrating that dopaminergic modulation may be a widespread mechanism for regulating axonal excitability in D3R-expressing neurons. As seen in Chapters 2 and 3, D3R-expressing cells are distributed across the brain, particularly within limbic areas. While the functional relevance of prefrontal AP bursts has been previously discussed (see Chapter 2, Discussion), future study will be needed to elucidate the possible function of D3R-dependent AIS modulation within these regions. For example, given that single AP bursts in the hippocampus can elicit synaptic plasticity (Huerta and Lisman, 1995), can D3R signaling regulate hippocampal plasticity via affecting burst generation?

Dopamine receptor expression of prefrontal projection neurons

In Chapters 2 and 3, I examined the expression of the D1R, D2R, and D3R on prefrontal projection neurons, highlighting the separation between D2R-expressing (D2+), pyramidal tract (PT) neurons, and intratelencephalic (IT) D1R- and D3R-

expressing (D1+, D3+) neurons. This provides a useful framework for testing the role of dopamine receptor modulation on prefrontal output, with appealing parallels to the segregation of D1R and D2R onto direct and indirect pathway medium spiny neurons in the dorsal striatum (Gerfen and Surmeier, 2011). These striatal cell populations are proposed to have opposing influences on behavior, both with respect to motor output and reinforcement learning (Kravitz et al., 2010, 2012).

However, just as the canonical model of basal ganglia function is likely an oversimplification (Calabresi et al., 2014), so too is this projection-pattern separation between D2+, PT neurons and D1+/D3+, IT neurons. While this model applies well to L5 pyramidal neurons, orthograde tracing experiments in Chapters 2 and 3 indicate that, in addition to their contribution to prefrontal IT output, mPFC D3+ neurons (likely in L6) also project sub-cortically. In addition, given that L2/3 projections are exclusively IT (Molnár and Cheung, 2006; Shepherd, 2013), the localization of many D2+ neurons to L2/3 suggests that D2+ mPFC neurons may contribute IT output. If D2R and D3R are also expressed on IT and PT pyramidal neurons, respectively, do known mechanisms of dopaminergic regulation apply (as described in L5, see Clarkson et al., 2017; Gee et al., 2012), or are these cells differentially regulated? Recent work shows that serotonergic modulation occurs selectively in callosally-projecting neurons across L2/3 and L5, suggesting that at least in some cases neuromodulatory regulation is projection-type specific, as opposed to lamina-specific (Avesar and Gulledge, 2012).

Given that both D1R and D3R are expressed on corticolimbic mPFC projection neurons, both cell classes may regulate appropriate responses to emotionally-salient stimuli. D1+ neurons in the mPFC are known to be activated during feeding, a

rewarding behavior, and stimulating their axons within the basolateral amygdala increases feeding in already sated animals (Land et al., 2014). Prefrontal output to these limbic regions is further implicated in emotional resilience in challenging environments, with pharmacological and knock-out studies suggesting a role for D3R signaling in both anxious and depressive behavior (Steiner et al., 1997; Leggio et al., 2013; Vialou et al., 2014).

This improved understanding of the distribution and function of dopamine receptors on mPFC pyramidal neurons projecting to limbic regions should inform future studies probing specific role of D1+ and D3+ neurons in regulating behavior. In addition, while D1+ and D3+ prefrontal pyramidal neurons have extremely overlapping projections at the gross anatomical level, it will be critical to determine whether these cells have the same cellular or subcellular targets, or whether perhaps divergent downstream innervation patterns could support distinct behavioral roles.

Supervised machine learning for electrophysiological classification: advantages and limitations

In Chapters 2 and 4, I described a supervised machine learning approach for prediction of dopamine receptor expression based on electrophysiological properties, which allowed for the confident prediction D1R- or D3R-expression of non-genetically labelled cells. However, this high confidence required rejecting “unidentified” cells that were in a zone of electrophysiological overlap between these populations, visualized as the intersecting distributions of D1+ and D3+ distances from the discriminant decision

boundary. With repeated hold-out cross-validation, on average 13.5±1.2% of D1+ cells and 19.8±1.3% of D3+ cells were misclassified across all classifiers.

This result indicates that the five variables chosen for electrophysiological analysis could not completely separate D1+ and D3+ populations. This might arise from suboptimal feature selection; perhaps there are other electrophysiological variables that better distinguish these two classes. This could be determined through either 1) additional data collection, with more varied stimuli or 2) more advanced methods of feature selection. For example, in Chapter 2, we elicited spiking with 300 ms depolarizing current pulses, which meant that for low AP firing rates, we could only examine short spike trains. Longer current injections could reveal more information. With respect to feature selection, I used exploratory data analysis to preselect variables that comprehensively described key electrophysiological properties of these cell classes. However, there are feature selection methods that take into account possible interactions between features as well as what classification algorithm is being used (Saeys et al., 2007); future analyses could employ these methods.

Furthermore, in supervised machine learning, the number of classes is predefined, and these groups are assumed to be independent. This is not always a valid assumption. Indeed, I found that the D1+ and D3+ populations partially overlapped, with 9% of D1R-expressing cells and 29% of D3R-expressing cells also expressing the D3R or D1R, respectively (Fig. 4). Therefore, “misclassified” cells may in fact represent D1R/D3R co-expressers, a possibility not allowed for within the classification approach used.

Final thoughts

This work establishes a critical framework for understanding the cellular and subcellular substrates of prefrontal dopaminergic modulation, revealing projection-specific roles for D1R-, D2R-, and D3R-expression on prefrontal pyramidal neurons, while highlighting additional sources of complexity requiring future study. For example, does D3R-dependent modulation of IT output in L5 also apply to subcortically-projecting D3+ neurons in L6? Is there a distinct functional role for D1R/D3R co-expressing pyramidal neurons and can these cells be identified by an intermediate electrophysiological phenotype? Finding the answers to these and other questions will clarify the mechanisms by which D3Rs subserve PFC-dependent cognitive function, and determine how currently-prescribed antipsychotics, with their high D3R affinity, may impact prefrontal cells and circuits.

References

Avesar, D., and Gulledge, A.T. (2012). Selective serotonergic excitation of callosal projection neurons. Front. Neural Circuits *6*, 1–11.

Bender, K.J., and Trussell, L.O. (2009). Axon initial segment Ca2+ channels influence action potential generation and timing. Neuron *61*, 259–271.

Bender, K.J., and Trussell, L.O. (2012). The physiology of the axon initial segment. Annu. Rev. Neurosci. *35*, 249–265.

Bender, K.J., Ford, C.P., and Trussell, L.O. (2010). Dopaminergic modulation of axon initial segment calcium channels regulates action potential initiation. Neuron *68*, 500–511.

Bender, K.J., Uebele, V.N., Renger, J.J., and Trussell, L.O. (2012). Control of firing patterns through modulation of axon initial segment T-type calcium channels. J. Physiol. *590*, 109–118.

Calabresi, P., Picconi, B., Tozzi, A., Ghiglieri, V., and Di Filippo, M. (2014). Direct and indirect pathways of basal ganglia: a critical reappraisal. Nat. Neurosci. *17*, 1022–1030.

Clarkson, R.L., Liptak, A.T., Gee, S.M., Sohal, V.S., and Bender, K.J. (2017). D3 Receptors Regulate Excitability in a Unique Class of Prefrontal Pyramidal Cells. J. Neurosci. *37*, 5846–5860.

Cotel, F., Exley, R., Cragg, S.J., and Perrier, J.-F. (2013). Serotonin spillover onto the axon initial segment of motoneurons induces central fatigue by inhibiting action potential initiation. Proc. Natl. Acad. Sci. U. S. A. *110*, 4774–4779.

Evans, M.D., Dumitrescu, A.S., Kruijssen, D.L.H., Taylor, S.E., and Grubb, M.S. (2015). Rapid Modulation of Axon Initial Segment Length Influences Repetitive Spike Firing. Cell Rep. *13*, 1233–1245.

Gee, S., Ellwood, I., Patel, T., Luongo, F., Deisseroth, K., and Sohal, V.S. (2012). Synaptic activity unmasks dopamine D2 receptor modulation of a specific class of layer V pyramidal neurons in prefrontal cortex. J. Neurosci. *32*, 4959–4971.

Gerfen, C.R., and Surmeier, D.J. (2011). Modulation of striatal projection systems by dopamine. Annu. Rev. Neurosci. *34*, 441–466.

Grubb, M.S., and Burrone, J. (2010). Activity-dependent relocation of the axon initial segment fine-tunes neuronal excitability. Nature *465*, 1070–1074.

Grubb, M.S., Shu, Y., Kuba, H., Rasband, M.N., Wimmer, V.C., and Bender, K.J. (2011). Short-and long-term plasticity at the axon initial segment. J. Neurosci. *31*, 16049–16055.

Hu, W., Tian, C., Li, T., Yang, M., Hou, H., and Shu, Y. (2009). Distinct contributions of Nav1.6 and Nav1.2 in action potential initiation and backpropagation. Nat. Neurosci. *12*, 996–1002.

Huerta, P.T., and Lisman, J.E. (1995). Bidirectional synaptic plasticity induced by a single burst during cholinergic theta oscillation in CA1 in vitro. Neuron *15*, 1053–1063.

Ko, K.W., Rasband, M.N., Meseguer, V., Kramer, R.H., and Golding, N.L. (2016). Serotonin modulates spike probability in the axon initial segment through HCN channels. Nat. Neurosci. 1–7.

Kole, M.H.P., and Stuart, G.J. (2012). Signal processing in the axon initial segment. Neuron *73*, 235–247.

Kole, M.H.P., Letzkus, J.J., and Stuart, G.J. (2007). Axon Initial Segment Kv1 Channels Control Axonal Action Potential Waveform and Synaptic Efficacy. Neuron *55*, 633–647.

Kravitz, A. V, Freeze, B.S., Parker, P.R.L., Kay, K., Thwin, M.T., Deisseroth, K., and Kreitzer, A.C. (2010). Regulation of parkinsonian motor behaviours by optogenetic control of basal ganglia circuitry. Nature *466*, 622–626.

Kravitz, A. V, Tye, L.D., and Kreitzer, A.C. (2012). Distinct roles for direct and indirect pathway striatal neurons in reinforcement. Nat. Neurosci. *15*, 816–818.

Kuba, H., Oichi, Y., and Ohmori, H. (2010). Presynaptic activity regulates Na+ channel distribution at the axon initial segment. Nature *465*, 1075–1078.

Land, B.B., Narayanan, N.S., Liu, R.J., Gianessi, C.A., Brayton, C.E., Grimaldi, D.M., Sarhan, M., Guarnieri, D.J., Deisseroth, K., Aghajanian, G.K., et al. (2014). Medial prefrontal D1 dopamine neurons control food intake. Nat. Neurosci. *17*, 248–253.

Leggio, G.M., Salomone, S., Bucolo, C., Platania, C., Micale, V., Caraci, F., and Drago, F. (2013). Dopamine D3 receptor as a new pharmacological target for the treatment of depression. Eur. J. Pharmacol. *719*, 25–33.

Martinello, K., Huang, Z., Lujan, R., Tran, B., Watanabe, M., Cooper, E.C., Brown, D.A., and Shah, M.M. (2015). Cholinergic afferent stimulation induces axonal function plasticity in adult hippocampal granule cells. Neuron *85*, 346–363.

Molnár, Z., and Cheung, A.F.P. (2006). Towards the classification of subpopulations of layer V pyramidal projection neurons. Neurosci. Res. *55*, 105–115.

Saeys, Y., Inza, I., and Larrañaga, P. (2007). A review of feature selection techniques in bioinformatics. Bioinformatics *23*, 2507–2517.

Shepherd, G.M.G. (2013). Corticostriatal connectivity and its role in disease. Nat. Rev. Neurosci. *14*, 278–291.

Shu, Y., Yu, Y., Yang, J., and McCormick, D. a (2007). Selective control of cortical axonal spikes by a slowly inactivating K+ current. Proc. Natl. Acad. Sci. U. S. A. *104*, 11453–11458.

Steiner, H., Fuchs, S., and Accili, D. (1997). D3 dopamine receptor-deficient mouse: Evidence for reduced anxiety. Physiol. Behav. *63*, 137–141.

Vialou, V., Bagot, R.C., Cahill, M.E., Ferguson, D., Robison, A.J., Dietz, D.M., Fallon, B., Mazei-Robison, M., Ku, S.M., Harrigan, E., et al. (2014). Prefrontal cortical circuit for depression- and anxiety-related behaviors mediated by cholecystokinin: role of ΔFosB. J. Neurosci. *34*, 3878–3887.

Wefelmeyer, W., Cattaert, D., and Burrone, J. (2015). Activity-dependent mismatch between axo-axonic synapses and the axon initial segment controls neuronal output. Proc. Natl. Acad. Sci. *112*, 9757–9762.

Yamada, R., and Kuba, H. (2016). Structural and Functional Plasticity at the Axon Initial Segment. Front. Cell. Neurosci. *10*, 1–7.

Publishing Agreement

It is the policy of the University to encourage the distribution of all theses, dissertations, and manuscripts. Copies of all UCSF theses, dissertations, and manuscripts will be routed to the library via the Graduate Division. The library will make all theses, dissertations, and manuscripts accessible to the public and will preserve these to the best of their abilities, in perpetuity.

Please sign the following statement:

I hereby grant permission to the Graduate Division of the University of California, San Francisco to release copies of my thesis, dissertation, or manuscript to the Campus Library to provide access and preservation, in whole or in part, in perpetuity.

[signature] 9/26/17

Author Signature Date